Doctoral Thesis in Physics

Magnetothermoelectric effects in magnetic thin films and multilayers

submitted to

Faculty of Physics
Bielefeld University

by

Oliver Reimer, M. Sc.

Bielefeld, March 26, 2018

Für meine Familie

„Wir müssen unbedingt Raum für Zweifel lassen, sonst gibt es keinen Fortschritt, kein Dazulernen. Man kann nichts Neues herausfinden, wenn man nicht vorher eine Frage stellt. Und um zu fragen, bedarf es des Zweifelns.“

Richard Feynman

Declaration

I wrote this thesis by myself and used none but the indicated sources and references. Text and figures are partly taken from corresponding publications, which originate directly from this work.

Bielefeld, March 26, 2018

Oliver Reimer

Reviewers
Prof. Dr. Günter Reiss
Prof. Dr. Thomas Huser

Printed on non-aging paper ISO 9706
Bielefeld University, Faculty of Physics
Center for Spinelectronic Materials and Devices

Dissertation to attain the doctoral degree of science (doctor rerum naturalium).

Contents

1. Vorwort

Im digitalen Zeitalter der Informationstechnologie wird die weltweite Kommunikation schneller und wichtiger, als es noch vor einem Jahrhundert hätte erwartet werden können. In Zeiten in denen die digitale Bildung bereits in der Kindheit beginnt, ist der problemlose Datenaustausch zu einer Selbstverständlichkeit für die moderne Gesellschaft geworden. Riesige Rechenzentren und die kontinuierliche Weiterentwicklung der Technologie sind vonnöten, um dem steigenden Bedarf von Industrie und Gesellschaft gerecht zu werden. Diesen Herausforderungen begegnet man durch den Bau von größeren Rechenzentren sowie der stetigen Erhöhung der Speicherdichten. Der durch Rechenzentren verursachte Energiebedarf trug mit 1.5% zum globalen Energieverbrauch in 2011 bei [1]. Als ein Thema von globaler Bedeutung ist der Klimawandel eine wichtige und aktuelle Herausforderung für die moderne Energiewirtschaft mit der Folge, dass der Energieverbrauch verringert oder zumindest die Energieeffizienz von Endgeräten gesteigert werden muss. Einen Kernaspekt stellen hierbei der Energieverbrauch von Prozessoren, Servern und Speichermedien sowie deren dauerhafte Kühlung während ihrer Operation dar. Aus diesem Grund können verschiedene Ansätze aus der Grundlagenforschung zu einer effektiveren Energienutzung in der modernen Informationstechnologie beitragen.

Mit der Entdeckung des Riesenmagnetowiderstandes (GMR) 1988 [2, 3], startete das Forschungsfeld der Spintronik unter Ausnutzung einer quantenmechanischen Eigenschaft des Elektrons, dem Spin, einen ungewöhnlich schnellen Fortschritt von Grundlagenforschung zur Anwendung. Die Nutzung von spintronischen Effekten erlaubte die kontinuierliche Miniaturisierung von Speichermedien, was zur wesentlichen Erhöhung von Speicherdichten führte und damit zur Verbesserung der modernen Speichertechnologien beitrug [4]. Desweiteren könnte eine Reduktion von Dissipationsenergie erreicht werden, wenn die digitalen Informationen in elektrischen Isolatoren gespeichert werden könnten und somit die physikalische Ursache Joule'scher Wärme vermieden wird. Das Forschungsgebiet der Magnonik beschäftigt sich mit Fragen wie dem Speichern, Auslesen und Transferieren von magnetischen Informationen anhand der quantisierten Quasi-Teilchen von Spinwellen, den Magnonen [5, 6]. Weil Magnonen in ferromagnetischen Isolatoren (FMIs) transportiert werden können, haben magnonenbasierte Bauteile das Potenzial, elektrische Bauteile sowie den damit verbundenen Energieverlust durch elektrische Abwärme zu minimieren. Das eher klassiche Feld der Thermoelektrizität konzentriert sich wiederrum auf die direkte Umwandlung von Wärme zu Elektrizität. Ein Vorteil von thermoelektrischen Bauteilen ist, dass sie sich nicht aus kleineren, beweglichen Bausteinen zusammensetzen und somit eine gesteigerte Lebenszeit und Effizienz aufweisen. Das macht sie zu langlebigen und verlässlichen Energiekonvertern [7]. Allerdings wird die Umwandlungseffizienz, beschrieben durch den Gütefaktor [8], durch das

Wiedemann-Franz Gesetz limitiert, welches es schwierig macht, alle nötigen Parameter in nur einem Material bestmöglichst zu optimieren.

Während des letzten Jahrzehnts verbanden sich die Felder der Spintronik und Thermoelektrizität zu einem neuen Forschungsfeld, der Spinkaloritronik. Hier werden die Wechselwirkungen des Elektronenspins mit Wärme erforscht und im Hinblick auf potenzielle Anwendungen untersucht [9]. So erzeugt der Spin Seebeck Effekt (SSE) beispielsweise einen Spinstrom durch einen thermischen Gradienten, welcher dann durch Magnonen in FMIs transportiert werden kann [10]. Neben reiner Wärme-zu-Spinstrom Umwandlung eröffnete die Spinstromerzeugung auch neue Ansätze für Wärme-zu-Ladungsstrom Bauteilen mit konzeptionellen Vorteilen gegenüber klassichen thermoelektrischen Bauteilen [11, 12].

Bis jetzt wurden alle spinkaloritronischen Experimente mit einem räumlich fixierten Temperaturgradienten relativ zu einer Probe durchgeführt. Die resultierenden Spinströme wurden nur durch Manipulation der Magnetisierung durch ein äußeres Magnetfeld oder der Stärke des Temperaturgradienten untersucht. Dies verhinderte systematische Studien relativ zur Kristallstruktur der untersuchten Proben. Im ersten Teil dieser Arbeit wird die Entwicklung eines neuen Aufbaus präsentiert, welcher die Untersuchung von anisotropen magnetothermoelektrischer Effekte ermöglicht. Dieses Instrument erlaubt die Drehung eines Temperaturgradienten in der Probenebene, welches in Kombination mit der Drehung eines externen Magnetfeldes die Rotation von thermisch induzierten Experimenten in Relation zur Kristallstruktur ermöglicht. Dadurch eröffnet es einen neuen Freiheitsgrad in der Untersuchung von thermisch induzierten Experimenten und trägt damit zur Vertiefung des Wissens von anwendungsrelevanten Materialien bei.

Der fortschreitende Miniaturisierungsprozess während der 80er Jahre von den bis dahin longitudinalen Speichermedien führte zu physikalischen Limits aufgrund von Selbst-Demagnetisierung in kleinen Dimensionen. Deswegen erhielten dünne Schichten mit hoher senkrechter magnetischen Anisotropie (PMA) erhöhte Aufmerksamkeit für vertikale magnetische Speichertechnologien [13]. Neben anderen Verbindungen wurden CoCr-basierte Legierungen als mögliche Kandidaten für senkrechte Speichertechnologien betrachtet. Allerdings führten verschiedene Einschränkungen zu thermischen Instabilitäten [14] und verhinderten die praktische Nutzung solcher Materialien. Ein alternativer Ansatz ist die Nutzung von Co basierten Multilagen. Ein abwechselndes Aufeinanderschichten von Co mit Pt oder Pd Lagen ermöglicht eine kontrollierbare PMA, welche durch Grenzflächeneffekte zwischen den Co und Pt/Pd Lagen induziert wird. Magnetoelektrische Effekte wie der anomale Hall Effekt (AHE) werden genutzt, um die magnetischen Eigenschaften von $[Co/Pd]_n$ Multilagen systematisch zu untersuchen und anzupassen [15, 16, 17, 18]. Heutzutage sind diese Multilagen aufgrund ihrer Nutzung für die thermische Spinstromerzeugung ebenfalls von großem Interesse für die spinkalorische Gemeinschaft. So kann zum Beispiel der thermisch äquivalente Effekt zum AHE, der anomale Nernst Effekt (ANE), zur Erhöhung der Wärme-zu-Ladungsstrom Umwandlungseffizienz beitragen, wenn er konstruktiv mit dem SSE überlagert wird [19]. Aus diesem Grund trägt Grundlagenwissen von Materialien und Bauteilen in Hinsicht auf magnetische Anisotropien, Transportkoeffizienten und Umwandlungsseffizienzen zur

Verbesserung von Rechengeschwindigkeiten, Energieverbrauch und Speicherdichten im Vergleich zu konservativen Halbleiterbauteilen bei [20].

Aktuelle Studien zeigen, dass sich in einigen Probensystemen die elektrischen Transporteigenschaften durch ihre thermischen Transporteigenschaften unter Ausnutzung der Mott Relation beschreiben lassen [21, 22]. Einerseits motiviert das die Suche eines Vorzeichenwechsels vom ANE in Probensystemen, welche bereits einen Vorzeichenwechsel im AHE zeigen. Ein solcher Nulldurchgang könnte eine Messung des longitudinalen SSE in Metallen ohne eine Verunreinigung durch den ANE ermöglichen. Andererseits könnte sich ein Maximum im ANE nützlich für die Anwendung in spinkaloritronikbasierten thermoelektrischen Bauteilen erweisen. Aus diesem Grund wird eine vergleichende Studie von dem AHE und ANE in $[Co/Pd]_9$ Multilagen in dem zweiten Teil dieser Arbeit durchgeführt, welche es erlaubt, die elektrischen und thermischen Transportkoeffizienten zu quantifizieren und zueinander in Relation zu setzen.

Das Kapitel über die theoretischen Grundlagen beinhaltet eine Beschreibung aller für diese Arbeit relevanten magneto(thermo)elektrischer Effekte. Ebenso werden die nötigen Formeln zur Beschreibung der experimentellen Daten hergeleitet und ein vertiefender Einblick in das Forschungsumfeld gegeben. Weil sich die experimentelle Arbeit in zwei Studien aufteilt, werden beide Studien im Methoden- und Diskussionskapitel unabhängig voneinander abgehandelt. Nach der Beschreibung und Charakterisierung des neuen Setups wird die Rotation des Temperaturgradienten zunächst mit einer Infrarotkamera nachgewiesen, bevor eine quantitative Analyse der anisotropen Magnetothermokraft (AMTP) folgt. Diese Studie erlaubt die Bestimmung des anisotropen Seebeck Koeffizienten einer dünnen Permalloyschicht und beweist das Funktionsprinzip des neuen Aufbaus. Der zweite Teil dieser Arbeit beschäftigt sich mit der Entwicklung des Experiments für die AHE und ANE Messungen an $[Co/Pd]_9$ Multilagen. Der Vergleich verschiedener thermischer und elektrischer Transportkoeffizienten wird in Bezug auf die Mott Relation durchgeführt, was in einem neuen Ansatz zur theoretischen Beschreibung resultiert.

2. Preface

In the digital age of information technology the world wide communication becomes faster and more important as anybody would have expected one century ago. In times when digital education already starts in childhood, the exchange of data has become a matter of course of modern civilization. Giant data centers and the permanent enhancement of technology are necessary to match the increasing demands of industry and society. One can face these challenges by either building larger data centers or, additionally, by storing the digital information more densely. The energy consumption of all data centers accounted to 1.5% of the global energy consumption in 2011 [1]. In times of climate change it is a topic of global interest to decrease energy consumption or, at least, use the available energy more efficiently. One key aspect is the energy consumption of the processors, servers and storage media during their operation and for cooling purposes. Thus, different approaches of fundamental research can lead to a more effective energy use in modern information technology.

With the discovery of the giant magnetoresistance (GMR) in 1988 [2, 3], spintronics, utilizing the quantum mechanic property of an electron, the spin, started a steep progression from fundamental research to applications. The utilization of spintronic effects allowed a continuous miniaturization of storage media, leading to high information densities and, thus, greatly improved modern data storage [4]. Additionally, a reduction of dissipation energy could be achieved if the digital information could be stored within electrical insulators avoiding the physical origin of charge-resistive heat. The field of magnonics deals with questions such as how to store, read-out and transfer magnetic information via the quantized quasi-particles of spin waves, the magnons [5, 6]. Since magnons are able to be transported within ferromagnetic insulators (FMIs), magnon based devices have the potential of substituting electronic based circuits and, thus, minimize dissipation losses. The rather classical field of thermoelectricity concentrates on the direct conversion of heat into electricity. The advantage of devices without mechanical moving is to increase their lifetime and efficiency. That makes thermoelectric devices to long lasting and reliable energy converters [7]. However, the conversion efficiency, described by the figure of merit [8], is limited by the Wiedemann-Franz law which makes it challenging to optimize all necessary properties within one material.

During the last decade, the fields of spintronics and thermoelectricity combined into the new field of spin caloritronics which investigates the interaction of the spin of an electron with heat [9]. Spin currents can be generated by thermal gradients via the spin Seebeck effect (SSE) [10] and be transported e.g. via magnons in FMIs. Besides of the pure heat-to-spin current conversion,

thermal spin current generation also opened a new approach for heat-to-electricity conversion devices with conceptional advantages over established thermoelectric devices [11, 12].

So far, all spin caloritronic experiments apply a thermal gradient along a fixed spatial direction of a sample and the resulting spin currents are only investigated in terms of manipulating the magnetization with an external magnetic field or by the strength of the thermal gradient. Thus, the thermal response of a given system could not be systematically analyzed with respect to the crystal structure. This work presents the development of a novel instrument which enables the investigation of the anisotropy of magnetothermoelectric effects. This versatile tool allows the in-plane (ip) rotation of a thermal gradient in combination with the ip rotation of an external magnetic field and enables the rotation of thermally induced experiments with respect to the crystal orientation. Hence, it opens another degree of freedom into thermal experiments and can deepen the knowledge of relevant materials.

The continuing miniaturization process during the early 80's of the so far longitudinal magnetic storage media led to physical limits due to self-demagnetization. Thus, thin films with high perpendicular magnetic anisotropy (PMA) gained attraction for high-density vertical magnetic recording technologies [13]. Beside others, hexagonal CoCr-based alloys were considered as candidates for perpendicular recording media but several issues, e.g. low remanent squareness, led to thermal instabilities of thin films [14] and impeded the technical utilization of these materials. An alternative approach is the use of Co based multilayers. An alternating stacking with Pt or Pd layers ensures a controllable PMA induced by interfacial effects between Co and Pt/Pd. Magnetoelectric effects such as the anomalous Hall effect (AHE) are used to systematically investigate and tune the magnetic properties of $[Co/Pd]_n$ multilayer systems [15, 16, 17, 18]. Nowadays, these multilayers are also of great interest in the spin caloric community because of their use for thermal spin current generation. For example, the thermal equivalent effect to the AHE, the anomalous Nernst effect (ANE), could enhance the heat-to-electricity conversion efficiency when constructively superimposed with the SSE [19]. Hence, fundamental knowledge of magnetic materials and devices in terms of magnetic anisotropies, transport coefficients and conversion efficiencies can improve data processing speed, decrease electric power consumption and increase integration densities compared to conventional semiconductor devices [20].

Recent studies suggest that in some sample systems electric transport properties can be related to their thermal transport properties via the Mott relation [21, 22]. On one hand, this motivates the search for a ANE sign change in sample systems which are known for a sign change of the AHE. A zero crossing point of the ANE would enable the parasitic free measurement of the longitudinal SSE (LSSE) in metals, which has been a challenging task for fundamental research. On the other hand, a maximum of the ANE could contribute to its application in spin caloric based thermoelectric devices. For this purpose, a comparative study between the AHE and the ANE is conducted on $[Co/Pd]_9$ multilayers to quantify and theoretically describe the electric and thermal transport coefficients.

Within the next chapter, an introduction to the relevant magnetothermoelectric effects of this work is given. The necessary equations to describe the experimental results are derived and a

deeper insight into the context of fundamental research is given. Since the experimental work of this thesis consists of two studies, the experimental methods as well as the results are presented for both studies individually. After the description and characterization of the novel setup, the rotation of a thermal gradient is first observed by using an infrared camera and then by a quantitative analysis of the anisotropic magnetothermopower (AMTP). This study allows to determine the anisotropic Seebeck coefficient of a permalloy thin film and proves the working principle of the new setup. The second part of this work describes the development of the experiment for the AHE and ANE measurements on $[Co/Pd]_9$ multilayers. The comparison of various thermal and electric transport coefficients is discussed in terms of the Mott relation, supposing a new theoretical approach to match the experimental results.

3. Theoretical Background

3.1. Electric transport

In this chapter, the basic description of thermoelectricity is followed by its combination with magnetic interactions. An overview of the magnetothermoelectric effects related to this work is given.

3.1.1. Electric potentials as driving forces

Within the semiclassical picture of statistical physics, electric current consists of flowing electrons. Because fermions can not occupy the same quantum state, the electron distribution is described by the Fermi-Dirac distribution

$$f(\epsilon) = \frac{1}{1 + \exp(\frac{\epsilon - \mu}{k_B T})} \quad . \tag{3.1}$$

The Fermi function is shown in Fig. 3.1 and specifies the propability of an electron to be found at the energy ϵ, at a given absolute temperature T and electrochemical potential μ [23]. At zero temperature, $f(\epsilon < \mu) = 1$ and $f(\epsilon > \mu) = 0$, indicating that the electrons occupy all available states up to the electrochemical potential while leaving higher energy states empty. Hence, at zero temperature, μ equals the Fermi energy ϵ_f which describes the highest occupied energy state in a given system. However, for higher temperatures, the transition of occupied to unoccupied states broadens, reflecting the fact that by introducing thermal energy into the system electrons of initially occupied states below ϵ_f gain enough energy to occupy states above ϵ_f. Note that μ is not a constant but temperature dependent and the probability of finding an electron with the energy $\epsilon = \mu$ is always 0.5 (see Fig. 3.1).

The Landau formalism describes the conduction in terms of transmission probabilities. Assuming a one-dimensional conductor which allows electrons to flow from one electron reservoir through a channel into another, one can define the energy dependent transmission probability $\Gamma(\epsilon)$. Note that $\Gamma(\epsilon)$ strongly depends on the density of states (DOS(ϵ)), which, in turn, is material dependent. The total charge current through the channel equals the net flow of electrons from one reservoir into the other. Thus, the transmission probability of an electron times the Fermi

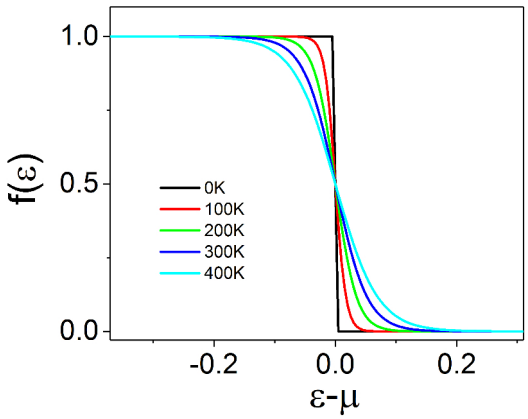

Figure 3.1.: The Fermi-Dirac distribution for different temperatures.

function at the same energy integrated over all energies,

$$I = \frac{2\,e}{h} \int f(T, \epsilon)\Gamma(\epsilon)\, d\epsilon \quad , \tag{3.2}$$

leads to the net charge current I, regarding the spin degeneracy (factor 2) and a unit correction by the Planck constant h [23].

In case of a pure electric transport, the equilibrium is disturbed by applying an external voltage V across both electronic reservoirs (Fig. 3.2) while keeping both at a finite temperature T_1. This results in a change of both Fermi functions since their electrochemical potentials will be split by the energy difference eV. But due to the same temperature T_1, the thermal broadening is the same for both. Then, Eq. (3.2) reads

$$I = \frac{2\,e}{h} \int \Big[f(T_1, \epsilon, \mu_1) - f(T_1, \epsilon, \mu_2) \Big] \Gamma(\epsilon)\, d\epsilon \quad , \tag{3.3}$$

hence, the difference of both Fermi functions determines the electron flow. This situation is depicted in Fig. 3.2. Here, $f_1(\epsilon)$ (left reservoir, red), $f_2(\epsilon)$ (right reservoir, green) with the corresponding μ_1, μ_2, respectively, and their difference $\Delta f(\epsilon) = f_1(\epsilon) - f_2(\epsilon)$ (blue) are shown. The electrons of all occupied states from the left reservoir fill the states of the channel. But since the occupation distribution around μ_1 is zero for the right reservoir, the electrons from the channel will further flow into the lower energy states of the right reservoir around μ_2. Hence, a stable voltage source will result in a stable charge flow. The direction of charge flow can also be understood in terms of $\Delta f(\epsilon)$. Independent of the energy, $\Delta f(\epsilon) \geq 0$, thus, the product of Eq. (3.3), $\Delta f\, \Gamma(\epsilon) \geq 0$, hence, all energy states from the channel contribute to an electron flow from left to right. This results in the fact, that the application of an external voltage always leads to a longitudinal charge current from the negative to the positive pole of the voltage source, independent of the material, i.e., its DOS(ϵ) [24, 25].

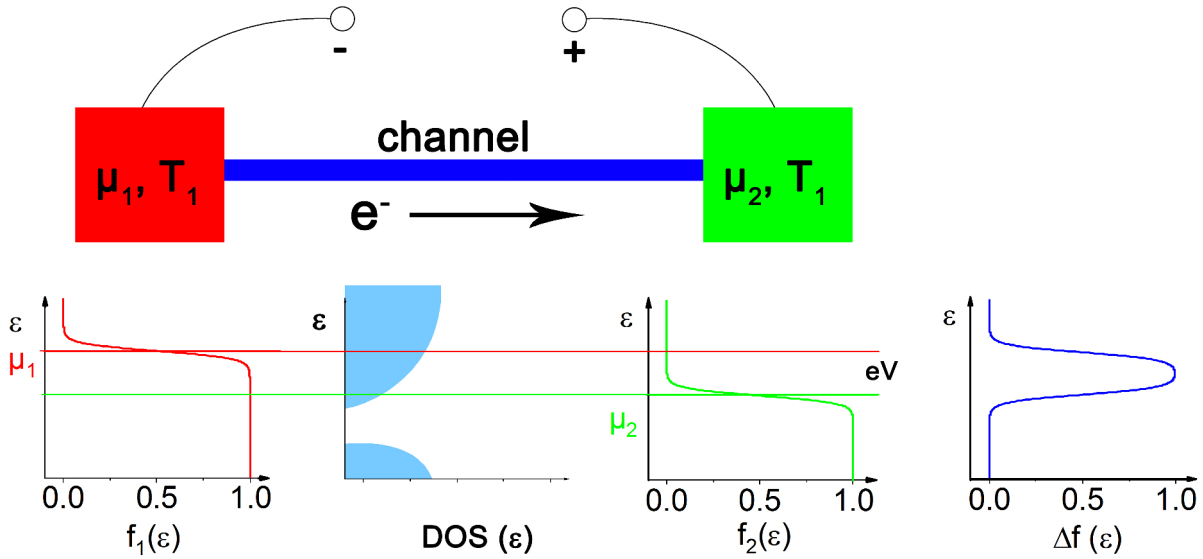

Figure 3.2.: Two electron reservoirs are connected by a conducting channel and are held at the same temperature T_1. Due to a voltage source the electrochemical potentials of the Fermi distributions of both reservoirs (red, green) are shifted and split by the energy eV, leading to a positive Δf (blue) and, thus, a charge current from left to right. Here, the electron flow direction is independent of the DOS of the channel.

3.1.2. Thermal gradients as driving forces

A temperature difference can induce charge transport in electrical conductors as discovered in 1821 by T. J. Seebeck [26, 27]. Followed by the discovery of the inverse effect in 1834, namely the generation of a temperature gradient by electric current (Peltier effect), the field of thermoelectrics was born. The development of semiconductor materials sped up the invention of applications based on thermoelectric effects. Today, thermoelectric devices are used as coolers, thermal energy sensors, power generators or waste heat recyclers [7, 8]. Especially in terms of the need for alternative, long-lasting energy technologies thermoelectric devices play an important role. This includes the search for high-efficiency thermoelectric materials which are characterized by the figure of merit ZT, determined by the Seebeck coefficient S, electrical conductivity σ and thermal conductivity κ

$$ZT = \frac{\sigma\, S^2}{\kappa}\, T \quad . \tag{3.4}$$

Thermoelectric transport can be described by continuing the description of electrically driven charge currents. Here, no external voltage but a temperature difference is applied to the two electron reservoirs. Thus, Eq. (3.2) reads

$$I = \frac{2\,e}{h} \int \Big[f(T_1, \epsilon, \mu) - f(T_2, \epsilon, \mu) \Big] \Gamma(\epsilon)\, d\epsilon \quad , \tag{3.5}$$

with $T_1 > T_2$ and the Fermi functions visualized in Fig. 3.3. In that case, due to the different

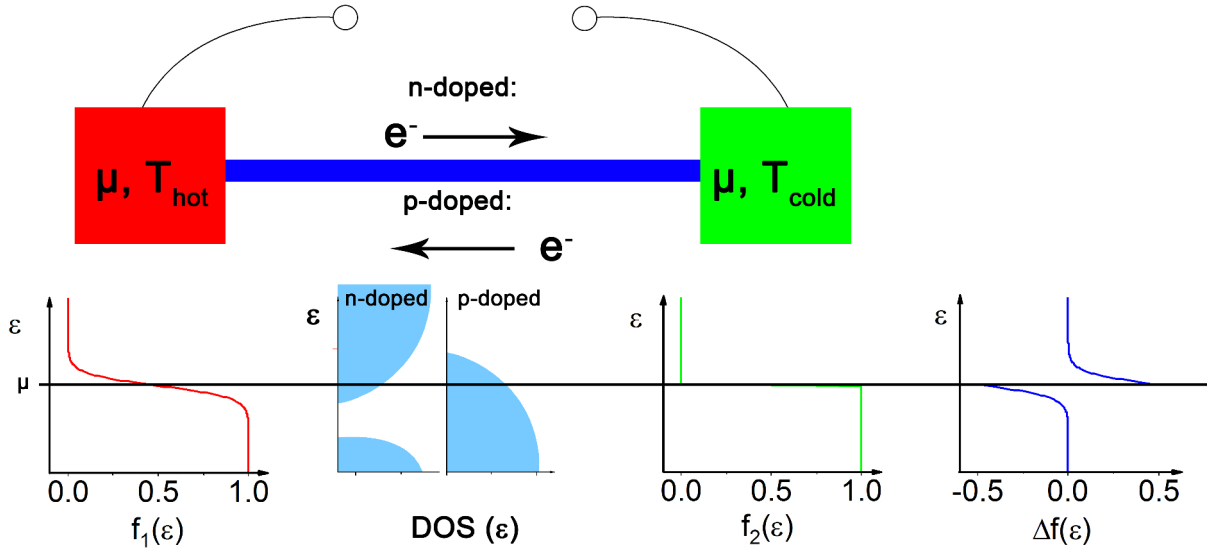

Figure 3.3.: In contrast to Fig. 3.2, both reservoirs are only subject to a temperature difference ΔT without an applied voltage. Now, due to different thermal broadening of f_1 and f_2, Δf changes sign for electrons higher or lower in energy than μ. This leads to a DOS(ϵ) dependent net electron flow direction, e.g., from hot to cold for n-doped but from cold to hot for p-doped materials.

thermal broadening of $f_1(\epsilon)$ and $f_2(\epsilon)$, the sign of $\Delta f(\epsilon)$ changes for energies lower or higher than μ (Fig. 3.3 (blue curve)). This difference leads to an opposite charge flow direction for electrons with energies higher or lower than μ. Similar to the first case, the electrons with $\epsilon > \mu$ from the hot reservoir flow into the free states of the channel and are dragged into the cold reservoir, since $f_2(\epsilon) < f_1(\epsilon)$. But in contrast, the electrons with $\epsilon < \mu$ flow from the cold into the hot reservoir, since here $f_2(\epsilon) > f_1(\epsilon)$. Therefore, one ends up with two opposite charge currents and the net charge flow depends on the DOS of the channel [24, 25].

The contrary influence of n-type or p-type DOS is illustrated in Fig. 3.3 by a scheme of the DOS for both types. Note that the DOS increases with increasing ϵ for n-type materials but decreases with increasing ϵ for p-type materials. Because of the integration over all energy states, the absolute number of states flowing in one or the other direction will determine the net flow direction. In an n-doped material, more states exist at $\epsilon > \mu$ than for $\epsilon < \mu$, thus, leading to a net current from hot to cold. Whereas for a p-doped material, the higher number of states at $\epsilon < \mu$ compared to $\epsilon > \mu$ determine the net flow direction from cold to hot. This important difference leads to applications like power generators or Peltier elements, where n- and p-type semiconductors are connected in series to enhance the power or heat output of the device.

In a next step, a general expression dealing with both voltage and temperature differences is derived. Again, the net current I is dependent on the difference of the Fermi functions, but this time with small perturbations in temperature and electrochemical potential, $\Delta T = T_1 - T_2$ and

$\Delta\mu = \mu_1 - \mu_2$, respectively,

$$I = \frac{2\,e}{h} \int \Big[f(T_1, \mu_1, \epsilon) - f(T_2, \mu_2, \epsilon) \Big]\, \Gamma(\epsilon)\, d\epsilon \quad . \tag{3.6}$$

Using a Taylor expansion, this difference can be expressed in terms of the energy derivative of the Fermi function

$$\begin{aligned} f(T_1, \mu_1, \epsilon) - f(T_2, \mu_2, \epsilon) &\approx \frac{\partial f}{\partial \mu}\, \Delta\mu + \frac{\partial f}{\partial T}\, \Delta T \\ &= \left(-\frac{\partial f}{\partial \epsilon} \right) \Delta\mu + \left(-\frac{\partial f}{\partial \epsilon} \right) \frac{\epsilon - \mu}{T}\, \Delta T \quad , \end{aligned} \tag{3.7}$$

leading to

$$\begin{aligned} I &= \frac{2\,e^2}{h} \int \left[\left(-\frac{\partial f}{\partial \epsilon} \right) \Delta V\, \Gamma(\epsilon) \right] d\epsilon + \frac{2\,e^2}{h} \int \left[\left(-\frac{\partial f}{\partial \epsilon} \right) \frac{\epsilon - \mu_0}{e\,T} \Delta T\, \Gamma(\epsilon) \right] d\epsilon \\ &= G\, \Delta V + L\, \Delta T \end{aligned} \tag{3.8}$$

with G as the charge conductance and L the thermoelectric conductance [23]. Equation (3.8) describes a charge current driven by a voltage and temperature difference, whereas the transport coefficients G and L include the transmission probability of the charge carriers being transmitted from one reservoir to the other. Equivalently, the heatflow Q can be described by the thermoelectric conductance L and the thermal conductance K

$$Q = L\, T\, \Delta V - K\, \Delta T \quad . \tag{3.9}$$

Note up to this point the description of the transport coefficients is based on the Landauer formalism, which only regards one-dimensional ballistic transport between two reservoirs. To generalize this formulation to bulk materials these expressions can be translated into the Boltzmann formalism simply by exchanging the transmission function $\Gamma(\epsilon)$ with the so-called transport distribution function $\Xi(\epsilon)$ [28]. Here, we are not interested in its exact formulation, but it should be stressed, that this function connects the number of states per energy with the number of states per wave-vector and also regards the dimension of the system under investigation [23, 29, 30]. However, it only changes the interpretation of the charge, thermoelectric and thermal conductances G, L and K into σ, α and κ, the electric, thermoelectric and thermal conductivities, respectively. Now, Eq. (3.8) and Eq. (3.9) read

$$I = \sigma \Delta V + \alpha \Delta T \tag{3.10}$$

$$Q = \alpha T \Delta V - \kappa \Delta T \quad . \tag{3.11}$$

Under open circuit conditions ($I = 0$), Eq. (3.10) can be expressed as

$$\Delta V = -\frac{\alpha}{\sigma}\, \Delta T = -S\, \Delta T \tag{3.12}$$

which is the ordinary Seebeck voltage, induced by a temperature difference ΔT and scaling with

the Seebeck coefficient S [31]. Note that due to the aforementioned reasons (e.g. DOS) α can be positive or negative, whereas σ is always positive. This indicates, that the Seebeck coefficient itself can be negative or positive for different materials depending on their electronic structure.

However, the transport coefficients still include an energy integral over $\Xi(\epsilon)$ and $\frac{\partial f}{\partial \epsilon_\mathrm{k}}$. The Sommerfeld expansion allows us to develop those integrals and after a first order expansion the transport coefficients become

$$\sigma = 2\frac{e^2}{h}[\Xi(\epsilon_\mathrm{F}) + ...] \quad , \tag{3.13}$$

$$\alpha = 2\frac{\pi^2\, k_\mathrm{B}^2\, e}{h}\, T \left[\frac{\Xi(\epsilon_\mathrm{F})}{\partial \epsilon}|_{\epsilon=\epsilon_\mathrm{F}} + ...\right] \quad \text{and} \tag{3.14}$$

$$\kappa = 2\frac{\pi^2\, k_\mathrm{B}^2}{3\, h}\, T[\Xi(\epsilon_\mathrm{F}) + ...] \quad . \tag{3.15}$$

By comparison of the Eqs. (3.13 - 3.15), the *Wiedemann-Franz law*, which relates the electric to the thermal conductivity,

$$\kappa = \frac{\pi^2\, k_\mathrm{B}^2}{3\, e^2}\, T\, \sigma \tag{3.16}$$

as well as a link between the thermoelectric and charge conductivity

$$\alpha = \frac{\pi^2 k_\mathrm{B}^2}{3\, e}\, T\, \frac{\partial \sigma}{\partial \epsilon} \tag{3.17}$$

can be found. With the definition of the Seebeck coefficient $S = \frac{\alpha}{\sigma}$ and Eq. (3.17), the *Mott relation*, connecting the Seebeck coefficient with the energy derivative of the conductivity at the Fermi energy,

$$S = \frac{\pi^2\, k_\mathrm{B}^2}{3e}\, T \frac{\partial(\ln \sigma)}{\partial \epsilon}|_{\epsilon_\mathrm{F}} \tag{3.18}$$

is derived [23].

3.1.3. Magnetoelectric transport

The field of *magnetoelectricity* describes electric transport phenomena influenced by magnetic phenomena. The most popular representatives of this field are magnetoresistive (MR) effects which describe the change of resistivity of a material or device depending on its magnetic state. Here, an external magnetic field H can influence electric properties of non-magnetic (e.g. paramagnetic) and magnetic (e.g. ferri- or ferromagnetic) devices or materials. Among others, the ordinary, anisotropic, giant, colossal and tunnel magnetoresistance are known [32, 33]. Depending on whether the resistivity changes continuously or discretely with the change of magnetic field, applications like magnetic field sensors, storage of binary data or read heads arose from these magnetoelectric properties [33, 34].

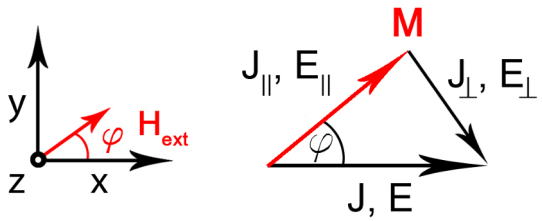

Figure 3.4.: When an electric current is driven through a ferromagnetic conductor along x, the electric resistance parallel and perpendicular to M is different due to the AMR. The different electric fields parallel and perpendicular to M result in different electric fields along the x- and y-axis, strongly depending on the angle φ.

The anisotropic magnetoresistance

In this work, the anisotropic magnetoresistance (AMR), already discovered in 1856 by W. Thomson [35], plays an important role and, therefore, is explained in more detail. The AMR describes the difference of the electric resistivity measured parallel and perpendicular to the magnetization direction of a ferromagnetic conductor. The AMR ratio is given by

$$\frac{\Delta\rho}{\rho_{\mathrm{avg}}} = \frac{\rho_{||} - \rho_{\perp}}{\frac{1}{3}\rho_{||} + \frac{2}{3}\rho_{\perp}} \quad , \tag{3.19}$$

with $\rho_{||}$, $\rho_{\perp}$ being the longitudinal resistivities for parallel and perpendicular magnetization with respect to the charge current, respectively, and ρ_{avg} as the average resistivity for a completely demagnetized state [36]. The external magnetic field couples to the spins of the electrons of the crystal lattice whose spatial distribution is determined by the atomic orbitals. Due to spin-orbit coupling (SOC), the rotation of spins results in a reorientation of the atomic orbitals, allowing the external magnetic field to rotate the atomic orbitals of the crystal lattice. In the case of asymmetric orbitals, this reorientation results in different scattering cross sections for mobile charge carriers depending on their direction relative to the magnetization direction. In general, the electric resistivity is typically reduced for a magnetization direction perpendicular to the electric current. Thus, the measured voltage across a ferromagnet depends on the directions of current and magnetization.

Following Thompson *et al.* [34], this direction dependence of the resistivity can be described by using the general transport equation

$$E = \rho\, J_{\mathrm{c}} \quad , \tag{3.20}$$

where an electric field E is induced by a charge current density J_{c} scaled by the resistivity ρ. Rotating an external saturation magnetic field in the x-y plane by the angle φ (Fig. 3.4), the magnetization will be orientated along the same angle φ. Applying a current density $|\vec{J}| = J_{\mathrm{x}}$, the longitudinal electric field E_{x} depends on the electric field components parallel and perpendicular to the magnetization and, thus, on φ. These components $E_{||}$ and $E_{\perp}$ can be described by J_{x},

the resistivities $\rho_{||}$ and $\rho_{\perp}$ and the angle φ as follows

$$E_{||} = \rho_{||}\, J_{\mathrm{x}}\, \cos\varphi \tag{3.21}$$

$$E_{\perp} = \rho_{\perp}\, J_{\mathrm{x}}\, \sin\varphi \quad . \tag{3.22}$$

Both components, in turn, contribute to the longitudinal measured electric field, E_{x}, by their projections onto the x-axis

$$E_{\mathrm{x},||} = E_{||}\, \cos\varphi = \rho_{||}\, J_{\mathrm{x}}\, \cos^2\varphi \tag{3.23}$$

$$E_{\mathrm{x},\perp} = E_{\perp}\, \sin\varphi = \rho_{\perp}\, J_{\mathrm{x}}\, \sin^2\varphi \quad . \tag{3.24}$$

The measured field along the x-axis then reads

$$E_{\mathrm{x}} = E_{\mathrm{x},||} + E_{\mathrm{x},\perp} \tag{3.25}$$

$$= \rho_{||}\, J_{\mathrm{x}}\, \cos^2\varphi + \rho_{\perp}\, J_{\mathrm{x}}\, \sin^2\varphi \quad . \tag{3.26}$$

Using $\sin^2\varphi = 1 - \cos^2\varphi$ and $\cos^2\varphi = \frac{1+\cos 2\varphi}{2}$ the longitudinal electric field describing the longitudinal AMR results in

$$E_{\mathrm{x}} = \left(\frac{\rho_{||} + \rho_{\perp}}{2} + \frac{\rho_{||} - \rho_{\perp}}{2}\cos 2\varphi\right)\, J_{\mathrm{x}} \quad . \tag{3.27}$$

Beside the longitudinal, the transverse electric field E_{y} can be measured as well while applying J_{x} and varying the magnetization direction. For this purpose, the projections of $E_{||}$ and $E_{\perp}$ (Eqs. (3.21) and (3.22)) onto the y-axes have to be considered, leading to

$$E_{\mathrm{y}} = E_{\mathrm{y},||} + E_{\mathrm{y},\perp} \tag{3.28}$$

$$= (\rho_{||}\, J_{\mathrm{x}} - \rho_{\perp}\, J_{\mathrm{x}})\, \cos\varphi\, \sin\varphi \quad . \tag{3.29}$$

With $\cos\varphi\, \sin\varphi = \frac{1}{2}\sin 2\varphi$,

$$E_{\mathrm{y}} = \frac{\rho_{||} - \rho_{\perp}}{2}\, \sin 2\varphi\, J_{\mathrm{x}} \tag{3.30}$$

describes the transverse electric field, also called transverse AMR or planar Hall effect (PHE), since this voltage is measured in the same plane as M and J, but perpendicular to J.

The Hall effect

Additional to the change of resistivity, a change of the electron flow direction can be the result of magnetism. In the late 19^{th} century E. H. Hall discovered the influence of H on a current-carrying conductor. He found, by applying H orthogonal to the current direction, that a potential difference perpendicular to both parameters occurs [37, 38, 39]. Later, this observation was explained by the Lorentz force, acting on moving charge carriers exposed to a magnetic field.

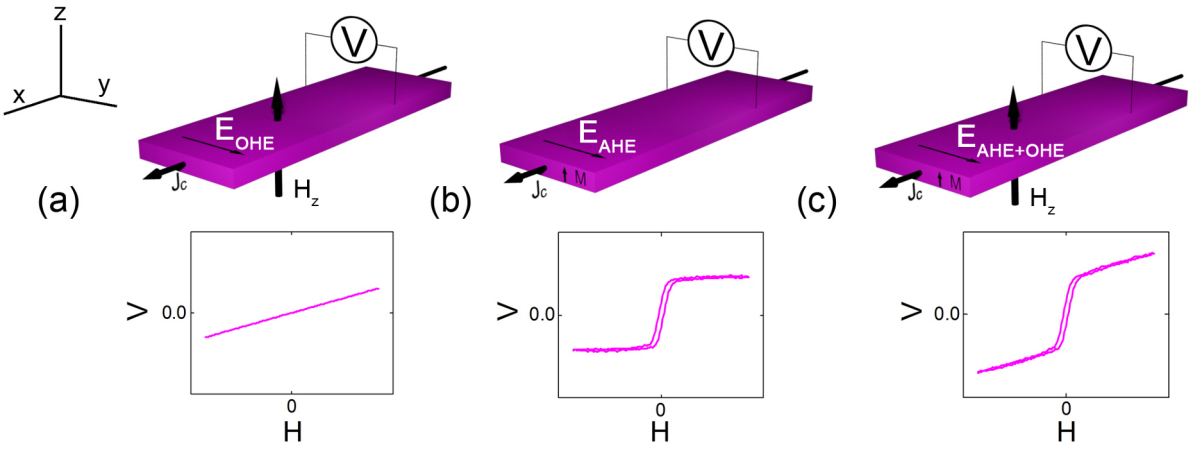

Figure 3.5.: While applying a charge current along the x-axis the voltage drop along the y-axis is measured for different magnetic situations. (a) A non-magnetic conductor only shows the linear OHE for increasing H_z while a magnetic conductor (b), ideally shows a non-linear AHE voltage with saturation values for high H due to saturated M_z. (c) A real experiment reveals a superposition of the OHE and AHE.

For open circuit conditions, this leads to a transverse voltage, characterized by the transverse resistivity ρ_{xy}. Nowadays, both parameters are named after their discoverer, the *Hall voltage* and *Hall resistivity*, respectively. Shortly after describing the Hall effect in non-magnetic conductors, E. H. Hall found the Hall resistivity to be much larger in magnetic conductors [40]. In the following, it was found that not only the magnitude of the Hall resistivity, but also its dependence on H of ferromagnetic conductors is qualitatively different compared to those of non-magnetic conductors. For non-magnetic conductors, the Hall resistivity depends linearly on H, whereas for magnetic conductors it steeply increases for low magnetic fields but nearly saturates for high magnetic fields. These observations led to the description of the Hall resistivity [41]

$$\rho_{xy} = \rho_{OHE} + \rho_{AHE} \tag{3.31}$$

$$= R_{OHE}\,\mu_0\,H_z + R_{AHE}\,M_z \quad , \tag{3.32}$$

indicating one contribution induced by H_z and another by the spontaneous magnetization M_z. ρ_{OHE} is the resistivity originating in the ordinary Hall effect (OHE) and ρ_{AHE} the resistivity due to the anomalous Hall effect (AHE). Additional to the magnetic permeability μ_0, both contributions can be described by the corresponding coefficients, the OHE coefficient R_{OHE} and the AHE coefficient R_{AHE}, respectively.

Figure 3.5 depicts the measurement geometries and resulting Hall voltages for different experimental situations. A non-magnetic conductor (Fig. 3.5 (a)) shows a linear Hall voltage along the y-axis with increasing H_z while applying a charge current J_c along the x-axis. In a magnetic conductor an additional voltage contribution proportional to the net magnetization occurs. Since in most cases M is manipulated by applying H_{ext} (Fig. 3.5 (b)), a non-linear shaped AHE voltage with a saturation value proportional to M will be recorded. Due to the simultanious

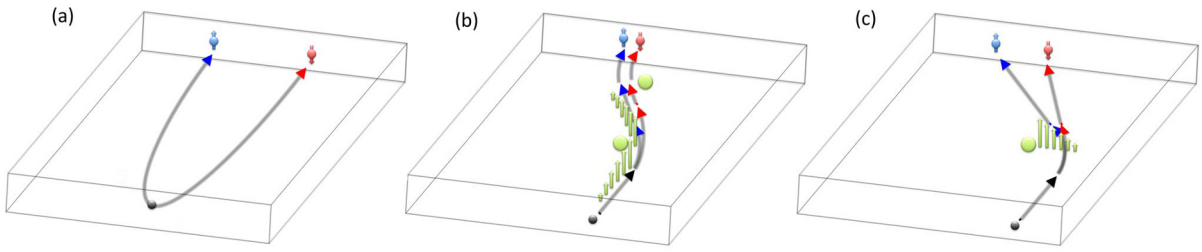

Figure 3.6.: Scheme of three different scattering mechanisms responsible for the AHE. (a) The Berry phase of the intrinsic crystal structure results in a motion transverse to the electric field, (b) the side jump mechanism deflects electrons spin-dependent at the atomic orbitals of impurities and (c) spin-dependent scattering due to SOC to impurities induces asymmetric skew scattering [43].

manipulation of the charge carriers by H and M, a superimposed voltage of the OHE and AHE will always be measured in a real experiment (Fig. 3.5 (c)). These contributions can be separated easily by determining the linear slope of the OHE voltage for high H and subtract it from the superimposed signal. This enables the quantification of the pure AHE voltage signal. Note if $R_{\mathrm{AHE}} \gg R_{\mathrm{OHE}}$, the OHE contribution can become very small.

General formulations of the induced electric fields with respect to the vectorial origin of the involved parameters are given by

$$\vec{E}_{\mathrm{OHE}} = -\mu_0 \, R_{\mathrm{OHE}} \, \vec{J}_{\mathrm{c}} \times \vec{H} \tag{3.33}$$

and

$$\vec{E}_{\mathrm{AHE}} = R_{\mathrm{AHE}} \, \vec{J}_{\mathrm{c}} \times \vec{M} \quad . \tag{3.34}$$

However, although the OHE coefficient R_{OHE} was quickly understood to depend mainly on the density of charge carriers, the origin of the AHE coefficient R_{AHE} and, thus, the AHE, was not fully understood for a long time [42]. It was found that R_{AHE}, besides of other material specific parameters, seemed to depend on the longitudinal resistivity $\rho_{xx} = \rho$. But only in the second half of the 20^{th} century, with the help of quantum mechanics and spin-orbit interactions, three different origins of the AHE could be identified and mathematically described.

First, the electrons gain a spin-dependent velocity component transverse to their driving external electric field (also called anomalous velocity, see Fig. 3.6 (a)) [44]. If the sum over the contributions of all occupied band states is nonzero, as it is the case for ferromagnetic conductors, a net contribution to the transverse Hall resistivity is obtained [42]. Since this contribution is only dependent on the perfect crystal Hamiltonian, it is named the *intrinsic* contribution. It shows, that a pure intrinsic scattering leads to a $\rho_{\mathrm{xy}} \propto \rho^2$ dependence and motivated the modern discussion of the Berry phase and Berry curvature [45].

Second, as a consequence of the intrinsic scattering, moving charge carriers get additionally

scattered at the electric fields of extrinsic perturbations of the perfect crystal, namely the atomic orbitals of impurities (Fig. 3.6 (b)). This *side-jump* scatter event also leads to a $\rho_{xy} \propto \rho^2$ dependence and, thus, can not be experimentally distinguished from the intrinsic scattering [46].

Third, the asymmetric and spin-dependent *skew* scattering, which results in different final momentum after scattering at lattice impurities, was discussed (3.6 (c)) [47, 48]. This theory results in a $\rho_{xy} \propto \rho$ dependence and seemed to be contradictory to the aforementioned theories.

For some decades a controversial debate proceeded whether the exponent n of the power law

$$\rho_{xy} = \lambda \rho^n \tag{3.35}$$

has to be assumed as 1 or 2 and, thus, favoring one or the other scattering process. Hence, many experimental studies concentrated on identifying the exponent n for different materials. For this purpose, their resistivities were varied either by increasing the temperature of the experiment or by changing the impurity concentration at low temperatures [49]. It turned out that n rather seemed to be continuous than discrete, reflecting that in real materials the underlying processes superimpose each other. Hence, the power law expresses the contribution of the intrinsic and side jump scattering ($n \approx 2$) in comparison to the skew scattering ($n \approx 1$). For more detailed information, the work of N. Nagaosa shall be recommended [42].

3.1.4. Magnetothermoelectric transport

In the chapter of thermoelectricity the influence of the electronic structure on the Seebeck coefficient, and the thermoelectric response was explained. It concluded that any change of the electronic structure, e.g. by a magnetic field or magnetization, influences the thermoelectric response of the material. As a consequence, the field of magnetothermoelectricity arises. The next two sections are attributed to the magnetothermoelectric effects related to this work.

The anisotropic magnetothermopower

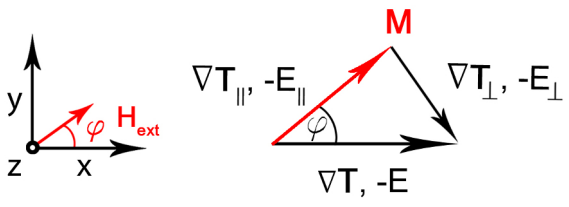

Figure 3.7.: Thermal analogon of Fig. 3.4: A temperature gradient is the driving force of an electric current along x. Due to the anisotropic orbitals of the atoms, the parallel and perpendicular Seebeck coefficients differ from each other. Thus, the measured thermovoltage depends on the direction of the magnetization.

As described Sec. 3.1.2, a thermal gradient along the x-direction (∇T_x) drives a charge current through the sample along the x-direction due to the Seebeck effect. Under open circuit conditions this results in a charge accumulation and in a measurable electric field along x. In a magnetic material, as described in Sec. 3.1.3, the magnetization influences the orientation of the anisotropic atomic orbitals. Thus, the scattering cross sections of the charge current differ for orientations parallel or perpendicular to M, leading to varying Seebeck coefficients $S_{||}$ and $S_\perp$. Similar to the AMR, the electric field along x depends on the electric field contributions parallel and perpendicular to M, which, in turn, depend on the angle φ between M and the x-axis (see Fig. 3.7). In analogy to Eq. (3.27), the longitudinal anisotropic magnetothermopower (AMTP) describes the electric field measured parallel to the applied thermal gradient with an in-plane magnetic field along φ

$$E_\mathrm{x} = -\left(\frac{S_{||}+S_\perp}{2} + \frac{S_{||}-S_\perp}{2}\cos 2\varphi\right)\nabla T_\mathrm{x} \quad . \tag{3.36}$$

Note in case of a non-magnetic material the Seebeck coefficient is isotropic ($S_{||} = S_\perp$) and Eq. (3.36) simplifies to

$$E_\mathrm{x} = -\left(\frac{S_{||}+S_\perp}{2}\right)\nabla T_\mathrm{x} = -S\,\nabla T_\mathrm{x} \quad , \tag{3.37}$$

describing the ordinary Seebeck effect. Hence, the AMTP (Eq. (3.36)) combines a magnetic field independent contribution (ordinary Seebeck effect) with a magnetic field dependent contribution due to the magnetization of a sample. Applying ∇T_x, rotating a magnetic field in the plane of a magnetic sample and measuring the voltage along x, results in a $\cos(2\varphi)$-oscillation of the voltage around an offset value based on the ordinary Seebeck effect.

Not only the longitudinal but also the transverse electric field induced by ∇T_x can be measured. As the thermal counterpart of the PHE (Eq. (3.30)), the transverse AMTP or planar Nernst effect (PNE) [50] follows

$$E_\mathrm{y} = -\frac{S_{||}-S_\perp}{2}\sin 2\varphi\,\nabla T_\mathrm{x} \quad . \tag{3.38}$$

It can be seen that a voltage measurement in a magnetic material perpendicular to the applied thermal gradient varies with $\sin(2\varphi)$, but cancels out for materials with isotropic Seebeck coefficients.

The Nernst effect

The charge carriers driven by the Seebeck effect underlie the same forces and scatter mechanisms as described for the Hall effects in Sec. 3.1.3. Assuming the same experimental geometries, a non-magnetic conductor exposed to a thermal gradient ∇T_x and a perpendicular magnetic field H_z induces an electric field E_y (Fig. 3.8 (a)). This effect is known as the first Ettingshausen-Nernst or simply the ordinary Nernst effect (ONE) [51]. It scales linearly with H and can be

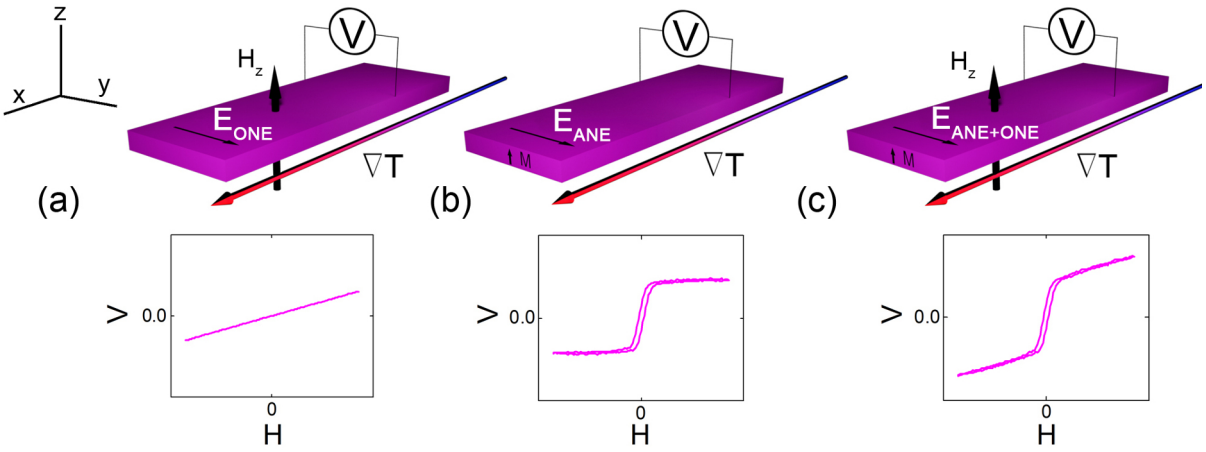

Figure 3.8.: Thermal equivalent to the Hall effects: While applying a thermal gradient along the x-axis the voltage drop along the y-axis is measured for different magnetic situations. (a) A non-magnetic conductor only shows the linear ONE for increasing H_z while a magnetic conductor (b), shows a non-linear ANE voltage with saturation values for high H. (c) A real experiment shows a superposition of the ONE and ANE, comparable to the electric charge driven equivalent.

described by the cross product

$$\vec{E}_{\mathrm{ONE}} = \mu_0 \, N_{\mathrm{ONE}} \, \nabla T \times \vec{H} \quad , \tag{3.39}$$

with the material dependent Nernst coefficient N_{ONE}. In a magnetic conductor, similar to the AHE, the application of a thermal gradient gives rise to the anomalous Nernst effect (ANE, Fig. 3.8 (b)), inducing an electric field transverse to ∇T and its magnetization M

$$\vec{E}_{\mathrm{ANE}} = N_{\mathrm{ANE}} \, \nabla T \times \vec{M} \quad . \tag{3.40}$$

Since the experimental measurement of the ANE includes the manipulation of M by the application of H, again a superposition of the ONE and ANE is measured (Fig. 3.8 (c)). Similar to the Hall effects, the different contributions can be separated by subtracting the linear ONE contribution from the superimposed signal.

3.2. Spin transport

The field of conventional electronics is based on pure charge currents, i.e., only takes into account the electronic charge of the electrons. With the development of relativistic quantum mechanics and in accordance to experiments it was found, that electrons additionally carry an intrinsic angular momentum. This angular momentum, called spin, is quantized and has the magnitude $\pm\frac{\hbar}{2}$. Additional, it is responsible for differing electron energies in an external magnetic field depending on their spin orientation, i.e., spin-up ($\uparrow$) or spin-down ($\downarrow$) [52]. In ordinary electronics

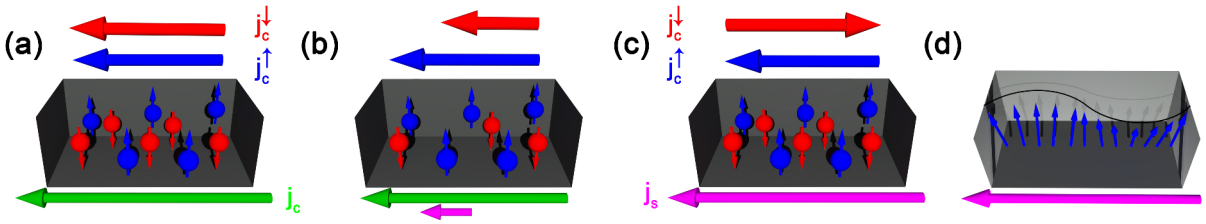

Figure 3.9.: (a) The equal amount of ↑ (blue) and ↓ (red) electrons flow in the same direction ($j_c^{\uparrow} = j_c^{\downarrow}$), resulting in a pure charge current j_c (green arrow). (b) An imbalance of electron species ($|j_c^{\uparrow}| \neq |j_c^{\downarrow}|$) causes a net charge current accompanied by a spin current (magenta arrow), also called spin-dependent or spin-polarized current. (c) When $j_c^{\uparrow} = -j_c^{\downarrow}$, no charge current but a pure spin current occurs. (d) In magnetic insulators, spin currents are transmitted via collective spin dynamics, i.e., magnonic excitations without the flow of charge carriers. The flow of spin information can generally be distinguished between electronic spin currents (based on spin of conduction electrons (b)+(c)) and magnonic spin currents (d).

the electron spins are randomly orientated and exhibit no influence on the functionality of the device. The field of *spintronics* integrates the spin degree of freedom into the functionality of electronics. Furthermore, it deals with questions like spin injection, spin manipulation and spin detection.

3.2.1. Spin currents

The integration of spin induced effects into electronic devices requires a clear definition and separation of the different origins, i.e., if these effects are based on charge or spin (or even both) information. In the beginning of spintronics, no consistent designation was assigned by literature, but after the increased interest in spintronics, a standardized formulation has been established. This formulation enables a better understanding of the underlying physics and shall be introduced now.

In the two channel model, ↑ and ↓ electrons can be treated as independent species of charge carriers with differing electric conductivities or even diffusion directions [53]. The resulting charge current can be described as the sum of the charge currents driven by both species

$$j_c = j_c^{\uparrow} + j_c^{\downarrow} \tag{3.41}$$

and the resulting transfer of spin angular momentum driven by the diffusion of charge carriers as the difference of the charge currents of both species

$$j_s = j_c^{\uparrow} - j_c^{\downarrow} \quad . \tag{3.42}$$

A pure charge current j_c, e.g. in non-magnetic metals, consists of a charge flow with an equal amount of ↑ and ↓ electrons (Fig. 3.9 (a)). Hence, no spin information is transmitted and j_c

is the origin of purely charge induced effects. If an imbalance between ↑ and ↓ electrons of a charge current occur, e.g. in ferromagnetic metals, the charge current is spin-polarized, i.e., is accompanied by a spin current (Fig. 3.9 (b)). Here, spin-dependent charge currents and resulting spin-dependent effects occur. For example, a spin-dependent charge current can be realized by spin injection. Since in a ferromagnet the electrical resistivity for the majority spins ↑ is substantially less than for minority spins ↓, a charge current becomes spin-polarized and the ferromagnet acts as a spin polarizer. In contrast to the aforementioned situations, two kinds of pure spin currents can occur. Firstly, the charge flow direction of ↑ and ↓ electrons is opposite but same in magnitude. Here, the moving charge carriers result in zero net flow of electric charge but in a pure spin current j_s (Fig. 3.9 (c)). Secondly, in magnetic insulators, localized electrons transmit the spin information via magnons, the quantized quasi-particles of spin waves [54]. In that case, $j_c = 0$, but $j_s \neq 0$ (Fig. 3.9 (d)). However, both mechanisms lead to pure spin currents and are the driving forces for spin effects. Therefore, the choice of materials influences potentially arising effects or, in turn, can exclude the appearance of parasitic contributions by unintended side-effects.

3.2.2. The spin Hall effect

As one of the most important consequences of SOC and its relevance for the next section the *spin Hall effect* (SHE) shall be explained in more detail. The generation of spin currents by charge currents can be explained as a result of the incorporation of special relativity into quantum mechanics. In a simple picture, in the rest frame of a moving electron the electric field of a crystal lattice can be Lorentz transformed into an effective magnetic field. This effective magnetic field interacts with the spin of the electron and influences its moving direction [55]. Due to the same scattering mechanisms as for the AHE (Fig. 3.6), the electrons scatter spin-dependently, transverse to their moving direction but in opposite directions. Whereas the electric field of the AHE can only be measured due to the intrinsic spin-imbalance of a ferromagnetic metal (FM), the SHE does not induce an electric field because of the lack of majority charge carriers [4]. Instead, a spin current is induced, accumulating ↑ electrons at one side and ↓ electrons on the opposite side [56] (Fig. 3.10 (a)).

Since a spin accumulation does not evolve an electric voltage, spin currents can not be detected by conventional electronic devices. The first observations of the SHE were based on optical methods, e.g., Kerr microscopy or p-n diodes [57, 58]. But for a convenient detection of a spin accumulation in electronic devices the electronic detection of the SHE became standard. For this purpose a reversed experiment to the above mentioned situation is utilized. A spin current is injected into a material with high SOC, i.e., electrons with opposite spin flow in opposite directions (no net charge flow). Due to the aforementioned reasons they get scattered perpendicular to their moving direction. As a result of their opposite spin and their opposite moving direction, all electrons get scattered into the same transverse direction (Fig. 3.10 (b)). Under open circuit conditions, the resulting charge current j_c generates an electric voltage which can be measured by ordinary voltmeters [59]. The described effect is the *inverse Spin Hall effect* (ISHE) and became the most

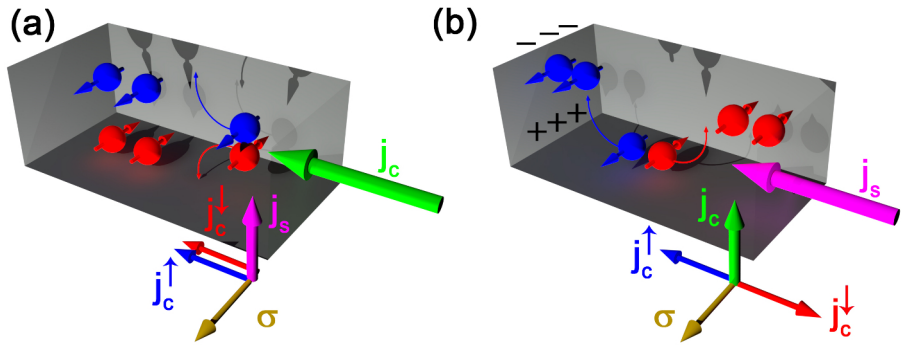

Figure 3.10.: (a) When an unpolarized charge current j_c (green) is applied to a material with high SOC, the electrons get scattered transverse to j_c and the spin polarization σ (yellow). The SHE generates a spin current j_s (magenta), leading to a spin accumulation under open circuit conditions. (b) Injecting j_s into the same material leads to scattering of all electrons into the same perpendicular direction, due to opposite spin orientations for opposite flow directions. Thus, under open circuit conditions, the ISHE converts a spin current into an electric voltage.

important effect to detect spin currents in spintronic devices. Hence, the SHE for spin injection and the ISHE for spin detection have a large impact in the spintronic community [60, 61].

Since materials exhibiting high SOC act as charge-to-spin current converter or vice versa, the material dependent *spin Hall angle*

$$\Theta_{\mathrm{SH}} = \frac{\sigma^{\mathrm{s}}_{\mathrm{xy}}}{\sigma^{\mathrm{c}}_{\mathrm{xx}}} \frac{e}{\hbar} \tag{3.43}$$

characterizes the conversion efficiency determined by the charge conductivity $\sigma^{\mathrm{c}}_{\mathrm{xx}}$ and the spin Hall conductivity σ^{s}_{xy}. The search for the best spin detector material revealed positive (Au, Pd, Pt) as well as negative Θ_{SH} (Ta, W, Mo) and Pt ($1\% < \Theta^{\mathrm{Pt}}_{\mathrm{SH}} < 10\%$) evolved as a broadly used spin detector material [43, 62]. The electric voltage induced by the ISHE is described by

$$\vec{E}_{\mathrm{ISHE}} = (\Theta_{\mathrm{SH}}\, \rho)\, \vec{j}_{\mathrm{s}} \times \vec{\sigma} \tag{3.44}$$

with the spin Hall angle Θ_{SH}, resisitvity ρ, spin current $\vec{j}_{\mathrm{s}}$ and spin polarization vector $\vec{\sigma}$ [59]. Thus, electrons flowing in opposite directions of $\vec{j}_{\mathrm{s}}$ have opposite spins which are aligned parallel or antiparallel to $\vec{\sigma}$. In a material with high SOC, transverse to $\vec{j}_{\mathrm{s}}$ and $\vec{\sigma}$ the ISHE voltage arises. Therefore, it can be used as an indicator for a spin current. The preferred direction of $\vec{\sigma}$, as mentioned before, can be a consequence of crystalline anisotropy or of the magnetization in FM layers adjacent to a normal metal (NM).

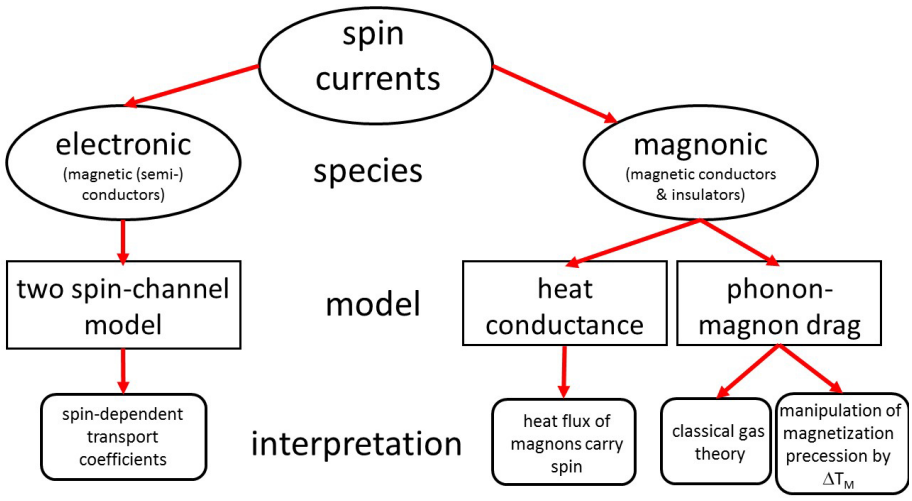

Figure 3.11.: Overview of different origins of thermally induced spin currents.

3.2.3. Spin caloritronics

The field of *spin caloritronics* combines the research fields of thermoelectricity and spintronics and investigates the interplay of heat driven spin- and charge currents [61, 63]. Although already theoretically discussed during the beginning of spintronics in the late 1980's [64], experiments stayed rare until the first decade of the new millennium [65]. The announced observation of the transverse spin Seebeck effect (TSSE) [66], i.e., the generation of a spin current by a transverse temperature gradient, initiated new interest for spin caloritronics. Although the existence of the TSSE was falsified and attributed to parasitic side-effects [67, 68, 69, 70], the controversial discussion led to a deeper insight of spin caloritronics and revealed its full potential for practical applications.

Thermal generation of spin currents

As described earlier, spin transport can either be based on the spins of conduction electrons or on collective perturbations of the magnetization, i.e., magnons. Thus, both spin current species need different explanations of their thermal generation. Figure 3.11 depicts an overview of the different models which are described in the following.

Electronic spin currents can be explained by the two spin-channel model of Mott [71]. Here, the electron transport is split into two independent spin transport channels. Spin flip mechanisms are excluded so that each electron stays in its specific channel. As the DOS determines the scattering rates of electrons as well as the Seebeck coefficient (as described in Sec. 3.1.2), both channels contribute differently to the electric and thermal transport. This results in spin-dependent transport coefficients so that the conventional charge conductivity consists of the two

spin-channel conductivities [9]

$$\sigma = \sigma^{\uparrow} + \sigma^{\downarrow} \tag{3.45}$$

as well as the Seebeck coefficient consists of the two spin-channel Seebeck coefficients

$$S = \frac{\sigma^{\uparrow} S^{\uparrow} + \sigma^{\downarrow} S^{\downarrow}}{\sigma^{\uparrow} + \sigma^{\downarrow}} \quad . \tag{3.46}$$

Applying a voltage to a ferromagnetic metal leads to a spin-dependent current due to the spin-polarization P of the conductivity for $\sigma^{\uparrow} \neq \sigma^{\downarrow}$ [72]

$$P = \frac{\sigma^{\uparrow} - \sigma^{\downarrow}}{\sigma} \quad , \tag{3.47}$$

and the application of a thermal gradient generates a spin-polarized current due to spin-dependent Seebeck coefficients. However, this simple picture can only explain spin-dependent transport phenomena but not magnonic spin transport phenomena.

For this reason, additional interactions besides of electron-heat interactions have to be taken into account. In the case of electronic spin currents, the conduction electrons as carriers of charge, spin and heat are considered. Now, magnons (the bosonic quasi-particles of spin waves) become important. As perturbations of the magnetization originating from the magnetic moments of localized d-electrons, magnons carry spin as well as heat. Although phonons only transport heat but no spin, they can indirectly influence the transport of spin due to scattering or dragging conduction electrons or magnons [11]. Accordingly, two mechanisms can explain the thermal generation of magnons. First, their thermal conductivity and second, magnon-phonon drag (see Fig. 3.11).

The first model deals with the heat conductivity of a magnetic insulator which consists of two contributions, i.e., of the magnon and phonon heat conductivity κ_{M} and κ_{P}, respectively. The applied heat is therefore absorbed not only by magnons but also by phonons. However, a thermal gradient induces a heat flux of magnons due to κ_{M},

$$j_{\mathrm{Q,M}} = \kappa_{\mathrm{M}} \nabla T \quad , \tag{3.48}$$

which directly corresponds to a thermally induced spin flux

$$j_{\mathrm{s}} = \frac{\hbar}{k_{\mathrm{B}} T} j_{\mathrm{Q,M}} \quad , \tag{3.49}$$

with Planck constant $\hbar$, Boltzmann constant k_{B} and temperature T. This expression is equivalent to a magnetization gradient, because each magnon also carries spin [11]. This rather simplistic picture was later expanded by the magnon-phonon coupling. In contrast to phonons, magnons do not directly couple to the heat reservoirs. Therefore, the system has to be regarded as consisting of magnons at the magnon temperature T_{M} and of phonons at the phonon temperature $T_{\mathrm{P}} \neq T_{\mathrm{M}}$. Only magnon-phonon coupling brings the magnons into thermal equilibrium with the phonons

(and simultaneously to the heat reservoirs) within a finite relaxation time τ_{MP}. Theoretical predictions show, that for large τ_{MP} (weak magnon-phonon coupling) it is impossible to deposit any heat into the magnonic system ($\kappa_{\mathrm{M}} = 0$), whereas for small τ_{MP} (large magnon-phonon coupling) $T_{\mathrm{M}} \rightarrow T_{\mathrm{P}}$ ($\kappa_{\mathrm{M}} > 0$). Thus, the interactions between phonons and magnons play a significant role for thermally induced magnons.

The second model is based on phonon-magnon drag. This interaction becomes important if more phonon-magnon than phonon-phonon collisions occur, i.e., the interaction time τ_{PP} is larger than τ_{MP}. Again, it is assumed that the applied heat only couples to the phonon system. In the picture of the ideal gas theory, both quasi particles are treated as classical particles which have momentum and diffuse along pressure gradients. Applying a thermal gradient to the magnon-phonon system corresponds to a pressure gradient in the phonon system, since heat only couples to the phonons. But due to magnon-phonon coupling, the phonon pressure gradient acts as a driving force for a magnon flux, transferring momentum from the phonons to the magnons [11].

Another interpretation uses the different magnon and phonon temperatures calculated by Sanders and Walton [73] and regards the microscopic origin of spin-waves. Here, the difference of both temperatures (ΔT_{M}) act as the driving force of magnon-phonon drag. In thermal equilibrium, T_{M} equals T_{P} and no force is present. Only with an applied thermal gradient, ΔT_{M} arises. At the hot side, the phonons heat up the magnons whereas at the cold side they cool the magnons. Since magnons are equivalent to the precession of magnetization, this results in a thermally induced magnetization gradient. However, the magnitude of phonon-magnon drag depends on the density of dragging phonons, as well as on the ratio of phonon-magnon to phonon-phonon or phonon-impurity scattering cross sections [74]. In summary, magnon-phonon drag has to be regarded as an additional contribution to spin currents, besides to the previously described heat conductivity mechanism.

The longitudinal spin Seebeck effect

As the most popular representative of spin caloritronics, the longitudinal spin Seebeck effect (LSSE) has a major impact on spin caloritronic research. The LSSE generates a spin current j_{s} parallel or antiparallel to a thermal gradient. Applied out-of-plane (oop) to a FM/NM bilayer j_{s} is transferred via spin injection into the adjacent paramagnet with high SOC. Due to the magnetization of the FMI (which lies ip the FM), j_{s} is polarized along M ($\vec{\sigma}||\vec{M}$) resulting in a measurable electric voltage because of the conversion by the ISHE (Eq. (3.44), Fig. 3.12). The LSSE was firstly observed in a ferrimagnetic insulator/normal metal bilayer (FMI/NM, YIG/Pt) [10] and was attributed to a magnonic spin current from either phonon-drag or magnon conductivity. The spin transfer from magnons in the FMI to the conduction electrons in the NM involves *s-d scattering*, describing the spin transfer from localized d-electrons (FMI) to conduction s-electrons (NM). Therefore, the magnitude of the LSSE strongly depends on the interface quality and the spin mixing conductance $g^{\uparrow\downarrow}$.

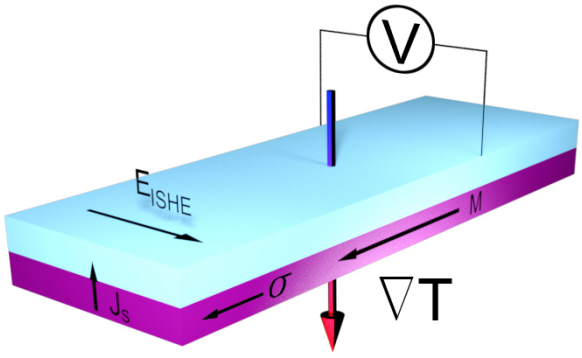

Figure 3.12.: When a thermal gradient is applied oop to a FMI/NM bilayer, an antiparallel spin current j_s to ∇T is generated. j_s is transmitted into the adjacent NM with high SOC and via the ISHE converted into a transverse electric field. The thermal generation of a spin current is called the LSSE.

The use of LSSE based devices for thermoelectric power generation is one of the most promising approaches for highly efficient green technologies. Increasing the figure of merit (Eq. (3.4)) in ordinary thermoelectric devices is limited, since σ and κ are coupled in isotropic materials via the *Wiedemann-Franz law*. In contrast, the thermoelectric conversion based on the LSSE involves a heterostructure allowing to tune the output signal at three independent levels. First, the heat-to-spin current conversion in the FM, second, the spin-angular transmission across the interface characterized by $g^{\uparrow\downarrow}$ and third, the spin-to-charge current conversion in the NM characterized by Θ_{SH} [12]. Due to these three factors, the heat and charge currents flow in different parts of the device. Hence, the figure of merit is determined by κ of the FM and σ of the NM. As a consequence, the Wiedemann-Franz law does not apply to this heterostructure system, allowing the enhancement of the total efficiency by a low heat conducting FM and a high charge conducting NM.

Additionally to the mentioned material flexibility, two other advantages arise from the utilization of the LSSE compared to ordinary thermoelectric devices. First, the ISHE voltage can easily be scaled by increasing the device area. A larger area of the FM induces a larger spin current into the NM which in turn is converted into a larger electric field. Since the output V_{LSSE} depends on the distance over which E_{ISHE} is measured ($V_{\mathrm{LSSE}} = E_{\mathrm{ISHE}}\, l$) larger contact distances also increase the output voltage [75]. And second, the effect geometry of the LSSE is advantageous in comparison to the conventional Seebeck effect. Because the conventional Seebeck voltage is generated parallel to a thermal gradient, an increase of the output voltage is achieved by a serial connection of single devices (Fig. 3.13 (a), (b)), leading to complex and costly mass production processes. LSSE devices, in contrast, generate the thermovoltage perpendicular to the thermal gradient, enabling a convenient enhancement of the output power only by increasing the area of the device (Fig. 3.13 (c), (d)), simplifying any future mass productions.

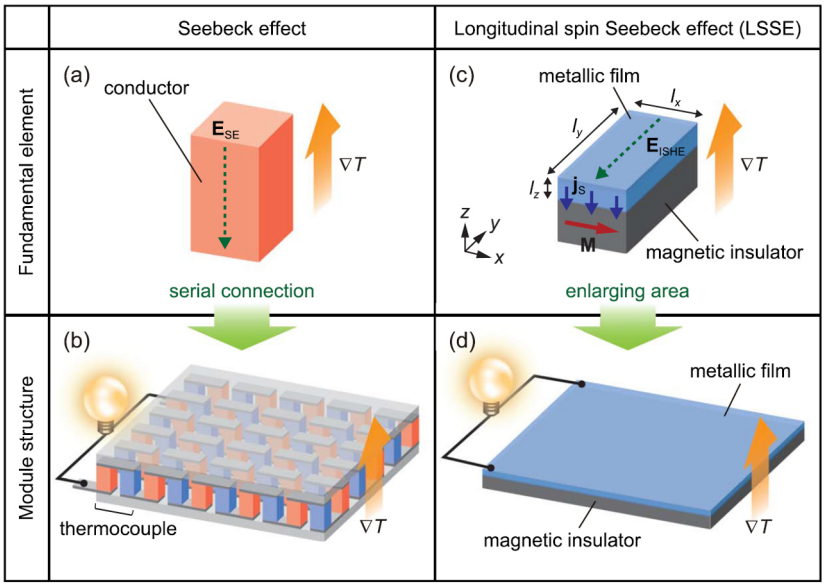

Figure 3.13.: Conventional thermoelectric device (a) compared to its spin counterpart (c). The different physical processes of the LSSE enables a simplified signal enhancement for large scale thermoelectric power generation (d) compared to ordinary TE devices (b). Figure taken from Ref. [12].

Enhancement of the LSSE efficiency

A lot of effort has been made in spin caloritronics to adress each point of the aforementioned three-level enhancement of the LSSE. A broad range of magnetic insulators has been investigated in terms of the heat-to-spin current conversion [12]. An improvement of $g^{\uparrow\downarrow}$ has been achieved by high crystal and interface quality [76, 77], post-annealing [78] or the use of an ultra-thin ferromagnetic interlayer between the FM and NM to enhance the magnetic moment density at the interface [79]. And finally, Θ_{SH} was examined not only for metals [80, 81], but also for alloys [82, 83], semiconductors [84, 85, 86] and organic materials [87, 88].

At this point, the optimization of the first parameter in the three-level improvement process shall be deepened, namely the heat-to-spin current conversion. The possible enhancement of the current conversion can again be divided into three approaches. As a final goal, all of these three approaches can be combined to reach an enhanced conversion efficiency. Firstly, the choice of material in which the conversion process takes place influences the conversion efficiency. Secondly, the design of the device for the spin current generation could offer a potential enhancement. And thirdly, a combination of different effects could enhance the final voltage output. Here, each approach is briefly addressed, directly leading to the motivation of the second part of this work.

1. Although the first experiments of the LSSE were conducted with FMI, the search for more appropriate materials quickly included ferromagnetic semiconductors and metals. Due to free charge carriers [69] and the same geometry of the LSSE and ANE, measurements of these

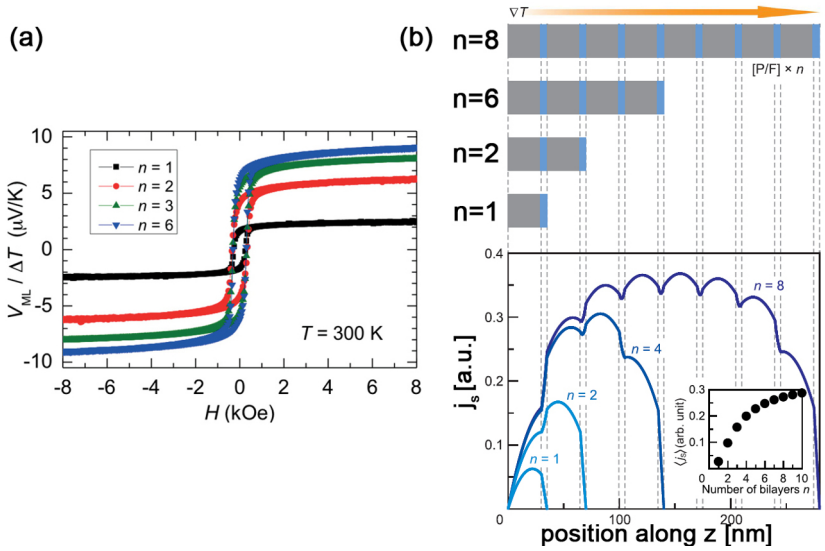

Figure 3.14.: (a) V_{LSSE} can be improved by using multilayer of FM/NM bilayers [92]. (b) The increase of V_{LSSE} can be attributed to an enhanced j_{s}. Due to continuous boundary conditions at the FM/NM interfaces, j_{s} will steadily increase with the number of repetitions, resulting in larger V_{LSSE} [12].

systems could now contain contributions from both magnetothermal effects. Therefore, ANE contributions have to be identified and excluded, before quantifying the LSSE magnitude in such a given system. This can be done by evaluating the ANE contribution of the ferromagnetic metal (FMM) without the spin detector material [89] or by utilizing the temperature dependence of the ANE coefficient [90].

2. For some years, heterostructures were established in LSSE measurements and one concentrated on the manipulation of both materials. In addition to this approach the use of alternately-stacked FM/NM bilayers can significantly enhance the LSSE [91]. It has been shown, that a repetition of 6 bilayers can enhance the LSSE up to a factor of 6 [92, 93] (Fig. 3.14 (a)). Instead of describing the multilayers as parallel contacted bilayers separated by the non-conductive FM, it seems more convenient to assume a serial connection between all bilayers. Because of continuous boundary conditions, j_{s} can not vanish in the NM between two adjacent FM, thus, j_{s} accumulates and monotonically increases with increasing repetition of the bilayer (Fig. 3.14 (b)). Hence, a larger j_{s} results in larger V_{LSSE}.

3. When the non-magnetic spin detector is exchanged by a ferromagnetic spin detector, the FM spin detector induces an additional ANE voltage to the LSSE voltage of the FMI (Fig. 3.15 (a) [12]). Similarly, the use of FMM instead of FMI generate a LSSE and an ANE voltage. This improvement has already been shown in combination with multilayers, which combines the improvement of multilayer and hybrid structures (Fig. 3.15 (b) [19]). For a constructive superposition of the ANE and the LSSE, the sign of Θ_{SH} has to match the direction of the ANE, otherwise a destructive superposition would occur.

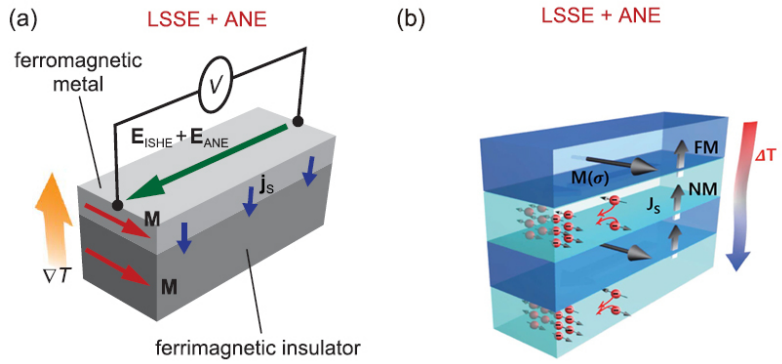

Figure 3.15.: A constructive superposition of the LSSE and ANE is achieved, when (a) a FMM spin detector [12] or (b) a FMM spin injector in multilayers is used [19].

The latter point suggests the use of FMM spin injector materials in multilayer systems to increase the total output voltage (Fig. 3.16 (a)). However, due to the first point, one needs to examine the pure LSSE contribution of the multilayer system to enhance this contribution. Hence, the ANE contribution has to be excluded at the first stage of analyzing the multilayer's potential for applications. In another configuration, the contribution of the LSSE can be excluded resulting in a pure ANE measurement. When the multilayer has an oop magnetization, the application of an ip thermal gradient only induces the ANE, since the induced spin current is not transmitted into the spin detector material but flows ip the FMM (Fig. 3.16 (b)). Although the spin polarization $\vec{\sigma}$ is still perpendicular to j_s, no ISHE can convert the spin current into a charge current because it is not injected into the NM. Reference [94] has shown that for $(Co/Pd)_9$ multilayers dependent on the Co thickness and base temperature the AHE vanishes due to a sign change of the anomalous Hall coefficient. The Mott relation, in turn, couples the electric transport coefficient to the thermoelectric coefficient. Thus, a sign change of the AHE coefficient points to a sign change of the ANE coefficient, indicating that a specific working point can be found where the ANE vanishes. Measuring in the LSSE configuration at this working point results in a pure LSSE signal. Therefore, in this work a study is conducted which compares the AHE and ANE of Co/Pd multilayers and tries to validate the Mott relation for these multilayers in a high temperature regime.

3.3. Generalized transport equation

For a better understanding of the used mathematical tools, this chapter summarizes all described transport phenomena and combines their transport coefficients into one general valid mathematical description. This overview simplifies the connection between driving forces, transport coefficients and resulting fields and additionally illustrates the broad field of yet undiscovered spin caloritronic effects.

In the linear response regime, any fluxes are proportional to the gradient of their corresponding

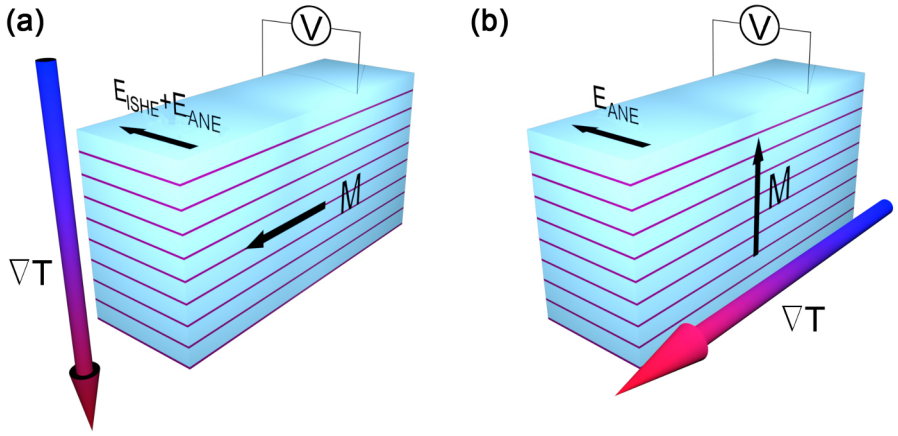

Figure 3.16.: (a) Measuring the transverse thermovoltage in FMM/NM multilayers in the LSSE geometry leads to a superposition of a LSSE and ANE voltage. (b) When the direction of M and ∇T are exchanged, no thermally induced spin current is transferred into the NM layer. Thus, no ISHE occurs and the pure ANE contribution can be investigated for future exclusions within LSSE experiments.

driving forces. For example, a heat flux j_q is proportional to a thermal gradient or the diffusion of particles j_d is proportional to a concentration gradient. In three dimensions, the fluxes $\vec{j}_k$ are connected via the anisotropic direct transport matrix $\widetilde{L}_k$ to their corresponding driving forces $\vec{X}_k$

$$\vec{j}_k = \widetilde{L}_k \, \vec{X}_k \quad . \tag{3.50}$$

As described in the last chapters, not only direct transport can occur, e.g., charge currents can not only be generated by an electric field. Also the superposition of differing driving forces can lead to the same current, e.g. the thermal generation of charge currents. Thus, each $\vec{j}_\mathrm{k}$ can be described as generated by different superpositioned driving forces $\vec{X}_i$, each connected via its specific three dimensional transport coefficient $\widetilde{L}_{ki}$ to the current

$$\vec{j}_k = \sum_{i=1}^{\mathrm{n}} \widetilde{L}_{ki} \, \vec{X}_i \quad . \tag{3.51}$$

For all existing forces a corresponding current is generated (k=[1...n]). In this work, three kinds of currents and driving forces are treated. The charge, spin and heat currents (indicated by the indice c, s, q, respectively) generated by a gradient of the electrochemical potential, spin accumulation and temperature gradient can be described through the transport tensor $\widehat{L}$ including all transport matrices $\widetilde{L}_{ki}$

$$\begin{pmatrix} \vec{j}_c \\ \vec{j}_s \\ \vec{j}_q \end{pmatrix} = \begin{pmatrix} \widetilde{L}_{\mathrm{cc}} & \widetilde{L}_{\mathrm{cs}} & \widetilde{L}_{\mathrm{cq}} \\ \widetilde{L}_{\mathrm{sc}} & \widetilde{L}_{\mathrm{ss}} & \widetilde{L}_{\mathrm{sq}} \\ \widetilde{L}_{\mathrm{qc}} & \widetilde{L}_{\mathrm{qs}} & \widetilde{L}_{\mathrm{qq}} \end{pmatrix} \begin{pmatrix} \nabla \mu_\mathrm{c}/e \\ \nabla \mu_\mathrm{s}/2e \\ -\nabla T/T \end{pmatrix} \quad . \tag{3.52}$$

Since all tensor elements $\widetilde{L}_{ki}$ are three dimensional matrices, all transport phenomena explained above are described within $\widehat{L}$. The diagonal components of $\widetilde{L}_{ki}$ describe longitudinal and the off-diagonal components of $\widetilde{L}_{ki}$ transverse transport phenomena. The direct transport coefficient $\widetilde{L}_{\mathrm{cc}}$ connects an electric field with a charge current and, thus, is the conductivity tensor. Here, the longitudinal transport coefficients imply Ohm's law and the AMR, whereas the transverse transport coefficients describe the AHE and PHE. The indirect transport coefficient $\widetilde{L}_{\mathrm{cq}}$ combines the thermal gradient with a charge current and, thus, includes the longitudinal AMTP and the transverse phenomena such as ANE and PNE. $\widetilde{L}_{\mathrm{sq}}$ describes a spin current induced by a thermal gradient, including the spin Seebeck effect and the recently discovered spin Nernst effect [95]. Consequently, the thermal and magnon Hall effects are described by the direct transport tensors $\widetilde{L}_{\mathrm{qq}}$ and $\widetilde{L}_{\mathrm{ss}}$ and the (inverse) SHE or (spin) Peltier effect [96] (among others) are attributed to the corresponding indirect transport coefficients of $\widehat{L}$.

Due to Onsager's reciprocity $L_{ki} = L_{ik}$ [97], the transport tensor is symmetric and Eq. (3.52) can be rewritten [9] to

$$\begin{pmatrix} \vec{j}_c \\ \vec{j}_s \\ \vec{j}_q \end{pmatrix} = \sigma(\epsilon_{\mathrm{F}}) \begin{pmatrix} 1 & P & ST \\ P & 1 & P'ST \\ ST & P'ST & \kappa T/\sigma \end{pmatrix} \begin{pmatrix} \nabla\mu_{\mathrm{c}}/e \\ \nabla\mu_{\mathrm{s}}/2e \\ -\nabla T/T \end{pmatrix} \quad , \tag{3.53}$$

with the Seebeck coefficient S, absolute temperature T, thermal conductivity κ, electric conductivity σ and spin polarization P. Here, S and P are defined as in Eq. (3.46) and Eq. (3.47), respectively, and $P' = \frac{\partial(P\sigma)}{\partial\epsilon}|_{\epsilon_{\mathrm{F}}}$ is the energy derivative of the spin polarization.

Cross linking of transport coefficients

In Sec. 3.1.2 it is shown, that the transport coefficients σ, κ and S are interconnected via the Wiedemann-Franz law and Mott relation. Recently, the Mott relation was tested and verified for different systems such as $Ga_{1-x}Mn_xAs$ semiconductors [21], Fe_3O_4 single crystals [22] or $[Pt/Co]_n$ multilayers [98]. In those works, AHE and ANE measurements are conducted at the same spots of the sample to ensure that both signals originate from the same sample properties such as crystal orientation, magnitude of magnetization or intrinsic impurities. Since in those experiments only the transverse transport coefficients are measured, based on Eq. (3.17), one obtains

$$\alpha_{\mathrm{xy}} = \left(\frac{\pi^2\, k_{\mathrm{B}}^2}{3\, e}\right) T\, \frac{d}{d\epsilon}[\sigma_{\mathrm{xy}}(\epsilon)]_{\mu} \quad . \tag{3.54}$$

A detailed derivation of the following expressions is given in the attachment, based on Ref. [22]. Basically, α_{xy} can be expressed in terms of three measurement parameters ρ_{xx}, T and S_{xx}

$$\alpha_{\mathrm{xy}} = \rho_{\mathrm{xx}}^{(n-2)} \left(\frac{\pi^2\, k_{\mathrm{B}}^2}{3e}\, T\, \lambda' - \lambda(n-2)\, S_{\mathrm{xx}}\right) \quad . \tag{3.55}$$

Here, k_B is the Boltzmann constant and e the electron charge. Thus, the electric measurement requires not only to measure ρ_{xy} but also ρ_{xx} since these resistivity tensor elements are correlated via the power law (Eq. (3.35)) and lead to the parameters λ and n. Note that λ' is the energy derivative of λ and is kept as a free fit parameter. During the thermal measurement, besides of the ANE coefficient, also the temperature dependent S_{xx} has to be measured. Following the work by Ramos *et al.* [22], S_{xy} is assumed to consist of two contributions. First, the off-diagonal thermoelectric tensor element induces an electric field along y. Second, a charge current driven by the ordinary Seebeck effect parallel to $\nabla_x T$ gets deflected by the Hall angle $\Theta_\mathrm{H} = \frac{\sigma_{xy}}{\sigma_{xx}}$ into the y direction. With Eq. (3.55) the anomalous Nernst coefficient becomes

$$\begin{aligned}\frac{E_y}{\nabla_x T} = S_{xy} &= \rho_{xx}\,\alpha_{xy} - S\frac{\sigma_{xy}}{\sigma_{xx}} \\ &= \rho_{xx}^{(n-1)}\left[\frac{\pi^2 k_\mathrm{B}^2}{3e}\,T\,\lambda' - \lambda\,(n-1)S_{xx}\right] \quad . \end{aligned} \tag{3.56}$$

By measuring S_{xx}, S_{xy}, ρ_{xx} and ρ_{xy} one can verify the validity of the Mott relation by fitting S_{xy} with Eq. (3.56). This allows to relate the thermal response of a given system to the electric response and, furthermore, an insight into the underlying scatter mechanisms.

4. Experimental Methods

4.1. Rotating in-plane thermal gradient setup

During this work, a new experimental setup has been designed and tested. It allows the application of a rotatable thermal gradient and magnetic field in different in-plane directions of a sample. This flexibility allows the investigation of magnetothermoelectric effects with respect to the crystal structure of a sample and is a new versatile tool for future research.

Figure 4.1 shows a schematic diagram of the setup which consists of three mandatory (thermal, magnetic, electric) and one additional (infrared) component if needed. Besides the physical periphery (symbolized by the rectangles), a software tool (symbolized by the ellipses) has been developed which controls the three mandatory categories and leads to one output file with the experimental parameters. The rotation of the thermal gradient has been verified before the actual measurements. For this purpose, an infrared camera was added to investigate the thermal distributions of different surfaces. Because the analysis of the infrared data is based on direct pictures of the sample's surface any optical obstacles as wires or Hallbar structures will influence and falsify the result. Hence, the infrared component can only be applied if no simultaneous electrical measurements are conducted and is only used for basic optical investigations of pure substrates.

In this chapter, each component is described in detail to give an overview of its operating function, limits, resolution, assumptions and potential for further improvements.

4.1.1. Thermal component

The thermal component of the setup is based on the work by M. Bovender who realized the first design during his Bachelor thesis [99]. Further improvements of his first design included changes of the Peltier element arrangement and the electric detection of the temperatures in order to improve the resolution and the spatial integration of the magnetic component. In the following, only the final version of the setup is described.

To achieve a rotatable thermal gradient (∇T) in the plane of a sample one uses the vectorial superposition of ΔT_x and ΔT_y. For this purpose a sample stage was designed which clamps a quadratic sample at four sides, see Fig. 4.2 (a). The temperatures of these four copper sample holders are individually controlled and allow the application of ΔT_x and ΔT_y. The developed

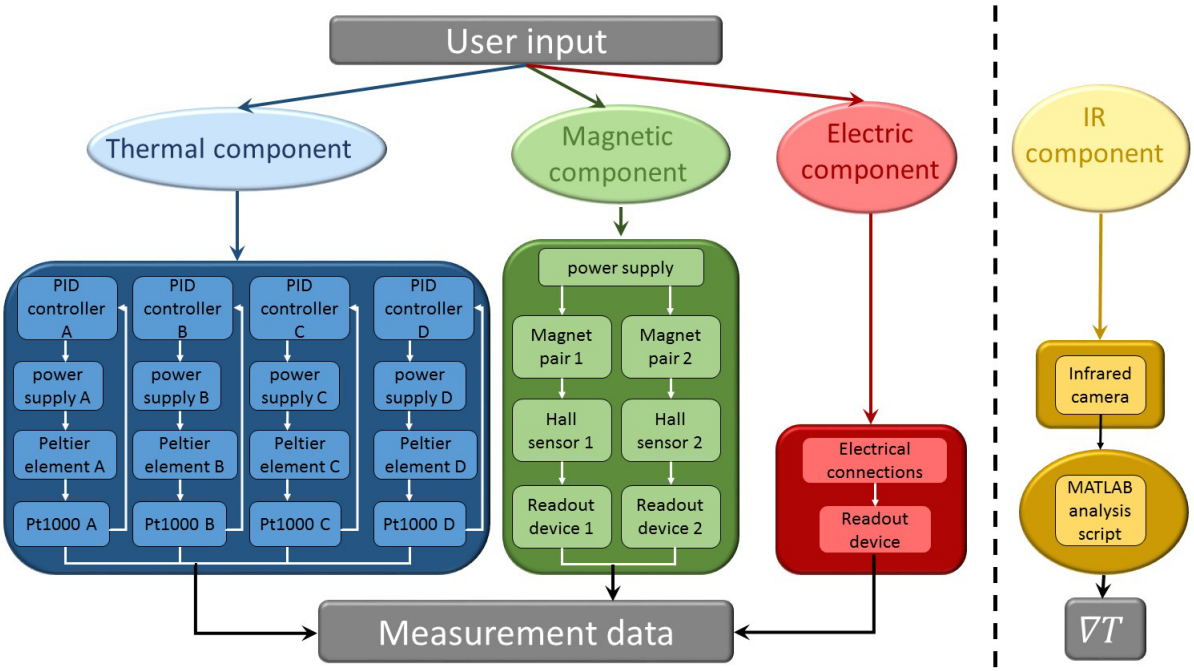

Figure 4.1.: A block diagram of the setup consisting of three obligatory components (thermal, magnetic, electric) and one optional component (infrared detection of the surface heat distribution). The ellipses represent software tools whereas the rectangles symbolize peripheral devices. Each component is described in detail in the chapters 4.1.1, 4.1.2, 4.1.3 and 4.1.4.

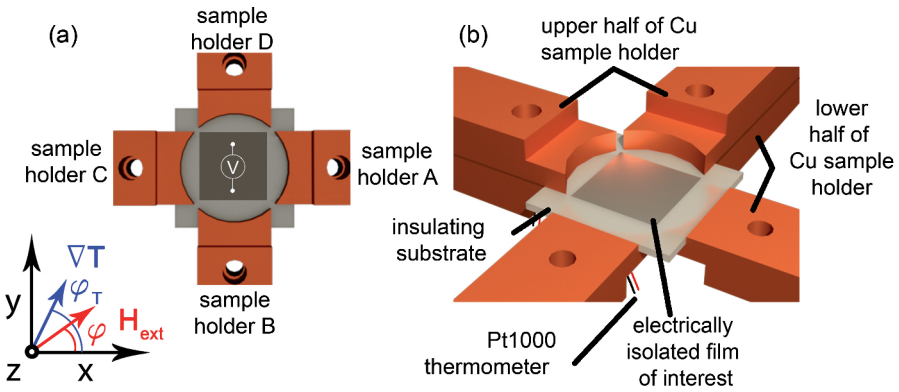

Figure 4.2.: The coordinate system defines the angles φ_T and φ of the thermal gradient and external magnetic field, respectively. (a) The sample is mounted between four sample holders which allow the separate application of an x-component ($\nabla_x T$) and a y-component ($\nabla_y T$) of ∇T. (b) For a pure in-plane ∇T the heat is transferred from an upper and a lower sample holder part into the insulating substrate. The sample edges of the studied film have been electrically isolated from the sample holder to exclude any parasitic Seebeck voltage contributions from the sample holders in the measurements.

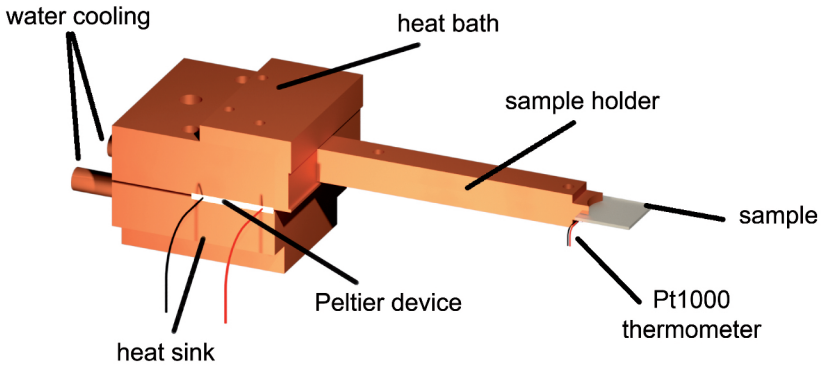

Figure 4.3.: All heaters consist of a Peltier element which is sandwiched between the water cooled heat sink and the heat bath. The heat bath transfers the heat via the sample holder to the sample.

control software *heater.py* needs the input parameters of the net temperature difference ΔT, the angle of the temperature difference, φ_T (as defined in Fig. 4.2), and the base temperature T_{base} of the experiment. These parameters are used to calculate

$$\Delta T_{\mathrm{x}} = \cos\varphi_{\mathrm{T}}\,\Delta T \tag{4.1}$$

$$\Delta T_{\mathrm{y}} = \sin\varphi_{\mathrm{T}}\,\Delta T \quad , \tag{4.2}$$

which allow the calculation of the temperature for each sample holder T_{A}, T_{B}, T_{C} and T_{D}

$$T_{\mathrm{A,C}} = T_{\mathrm{base}} \pm \frac{\Delta T_{\mathrm{x}}}{2} \tag{4.3}$$

$$T_{\mathrm{B,D}} = T_{\mathrm{base}} \mp \frac{\Delta T_{\mathrm{y}}}{2} \quad . \tag{4.4}$$

These settings are transmitted to the PID controllers (Newport Electronics, i3252-C24) which remotely control the heating power output of four power supplies (Manson HCS3202) (see Fig. 4.1 blue rectangular). Note that the maximum current is limited to 4 A to avoid inflicting critical damage on the Peltier elements.

As can be seen in Fig. 4.2 (b), the heat is not only transferred from the bottom to the sample substrate but also from an upper part of the copper sample holder. This sample holder arrangement allows the application of a pure in-plane ∇T without any parasitic out-of plane ∇T components as shown in different works [68, 69]. At the lower part of the sample holder, 2 mm next to the sample, Pt1000 thermometers are fixed with temperature stable two-component glue to electrically measure the temperature of each sample holder and give a feedback to the PID controller.

More technical details can be found in Fig. 4.3. Peltier elements with (30.0 x 15.0 x 3.8) mm^3 are chosen as heating devices which can also be used as coolers by changing the current direction. Therefore, a higher and more stable temperature regime is accessible in comparison to resistive

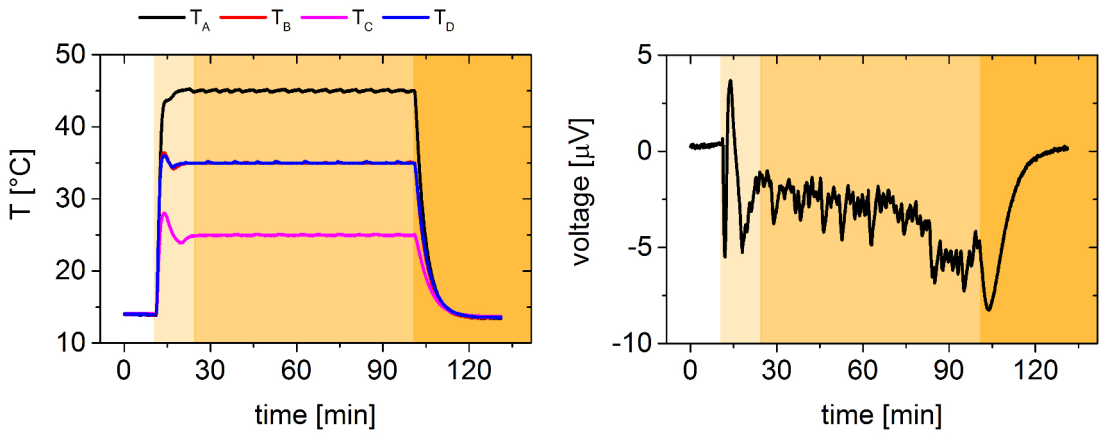

Figure 4.4.: Measuring the temperatures of all sample holders and the corresponding background voltage along the y-axis as depicted in Fig. 4.2 with applied ΔT=20 K, T_{base} = 35° C and φ_T. The different background colors indicate the different thermal phases: thermal equilibrium at room temperature (0-10 min), heat up (10-25 min), nearly reaching thermal stability (25-100 min) and cool down (100-130 min).

heaters. Using thermal conductive paste, the Peltier elements are sandwiched between two copper blocks. Due to the working principal of a Peltier element, it will be heated on one side and cooled down on the other side. The main purpose is to heat the upper block which transfers the heat via the sample holder to the sample and simultaneously cools the lower block. It is important to provide a stable heat sink because, otherwise, heat convection could lead to a heat transfer from the heat bath to the heat sink. This heat transfer could warm up the heat sink and affect the heating efficiency of the Peltier element. For this purpose, the lower block has a U-shaped drilling with connections to a water cooling system, which stabilizes the lower block at about 8°C and allows the dissipation of convectional heat. The complete heating stage is flexibly attached to a ground plate that enables its positional adjustment for different sample sizes.

After implementing the electric component as described later in chapter 4.1.3, a first measurement is conducted to characterize the thermal stability of the system. Hence, a permalloy sample is contacted along the y-axis, (see Fig. 4.2 (a)) and the (thermal) offset voltage is measured after an initial autotune of the PID controllers and applying $\Delta T = 20\,\mathrm{K}$, $T_{base} = 35°\,\mathrm{C}$ and $\varphi_T = 0°$ for over 2 hours.

Figure 4.4 shows the temperature distribution of each sample holder and the corresponding voltage vs. time. During the first 10 min. (white background) all heaters are in thermal equilibrium at room temperature. The small temperature variation of 0.1 K lies within the temperature sensitivity of the PID controllers and the resulting voltage during this period stays constant at $(0.3 \pm 0.1)\,\mu$V. At least this measurement accuracy is necessary to resolve spin caloric effects in the nanovolt regime. Now, the thermal gradient is applied and 15 min. (light yellow background) after turning on the heating process each heater reaches its final temperature. During the thermal non-equilibrium the voltage varies in a range of 8 μV which shows the need of conducting the experiments at thermal equilibrium. However, during the following 75 min.

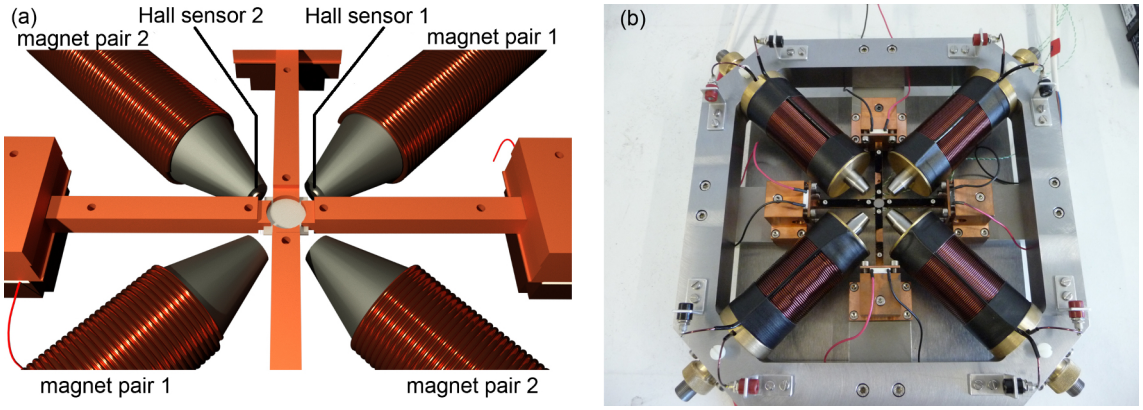

Figure 4.5.: (a) Technical design of the magnetic component. Four electromagnets with iron cores, connected via a magnetic yoke, are integrated into the setup. The opposing magnets define two magnetic axes which, due to vectorial superposition, result in a rotatable magnetic field in the plane of the sample. Two Hall sensors allow the detection of the magnetic field. (b) Photograph of the realized magnetic component added to the thermal component.

(mid yellowish background) regular temperature oscillations of $\Delta T = 0.2$ to 0.4 K for all sample holders can be observed. These oscillations have a strong impact on the measured voltage, as can be seen in Fig. 4.4. With an applied ΔT the voltage drops to an average value of about $-2.5\,\mu$V but with large variations over $2\,\mu$V. These variations can be explained by the oscillating ΔT. Even small variations in ΔT can cause voltage changes of a few μV, since typical Seebeck coefficients are in the range of μV/K (e.g. $S_{Py} = -4.5\,\frac{\mu V}{K}$, $S_{Au} = 1.8\,\frac{\mu V}{K}$ [100, 101]). Hence, for detecting effects in the nanovolt regime even temperature variations of 0.2 K have to be excluded. 100 min. after starting the measurement (dark yellow background) the heaters are turned off, all temperatures decrease to room temperature and the voltage saturates at the initial $0.3\,\mu$V with low background noise.

A systematic variation of the PID parameters showed that the use of four independent PID controllers cannot stabilize the temperature within 0.3 K variation (see attachment). As a consequence, the PID controllers are only used for a rough adjustment of the power supplies until the temperatures oscillate within 0.3 K around their final temperature. Then, the PID control circuit is deactivated and the power supplies are tuned to the before applied powers. Although the automatic temperature regulation is turned off, the water cooling system and the Al shielding box (as described below) keep the temperature distribution stable for a sufficiently long duration. This proceeding enables the needed low-level background noise to resolve thermoelectric voltages in the nanovolt regime (see chapter 5.1). A future improvement might be a remotely controlled switching between a variable and a constant PID output voltage. Thus, after reaching minimal thermal deviation, the PID output voltage and, in turn, the power output of the power supplies is fixed. Another approach could be the use of a multi-channel PID controller which regards the thermal coupling of all heater channels.

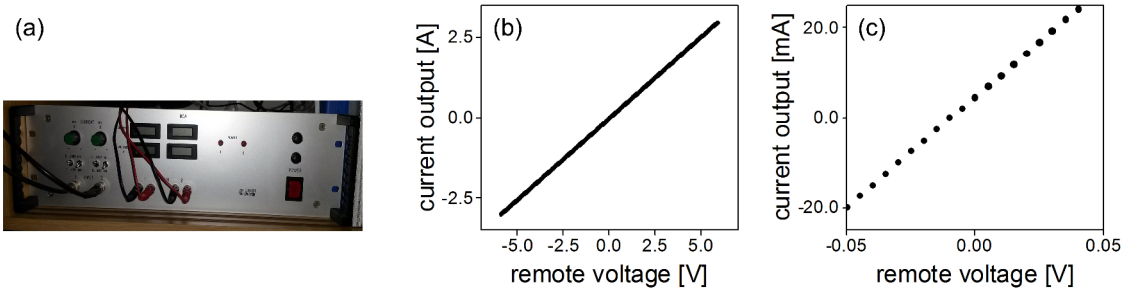

Figure 4.6.: (a) The in-house built power supply provides each magnet pair with up to ±5 A using an input control voltage of ±10 V. (b) The graph shows the current output vs. the remote voltage of the digital/analog converter. (c) Close-up of (b), indicating the high resolution of the power supply. The lowest increase of the remote voltage by 5 mV results in an output increase of 2.5 mA.

4.1.2. Magnetic component

Similar to the rotation of ∇T, a vectorial superposition of two magnetic axes is used to gain a rotated net magnetic field at the center of the sample. Four electromagnets with iron cores of 14 mm diameter and windings made of Cu wire with a diameter of 1.25 mm connected by an iron yoke are integrated into the setup (see Fig. 4.5). The opposing electromagnets are electrically connected in series in a way that one pole cap is the north- and the other pole cap the south pole. This defines two separate magnetic axes which can be controlled individually. Additionally, a Hall sensor (AS-NTP Flex, Projekt Elektronik, temperature stable up to 100°C) is pressure-reliefly attached to one pole cap of each magnetic axis, allowing the direct measurement of the magnetic field of both magnetic axes. Due to the measured magnetic field range, the voltage output of each Hall sensor is amplified (40x), measured by Keithley2000 multimeters and sent to the computer for recording. Hence, after further calibrations (for further information see attachment), one can conclude the net magnetic field at the sample position by measuring the magnetic field at the pole caps.

In order to apply a well controlled magnetic field, an in-house built, remote controlled, 2-channel bipolar power supply is used (see Fig. 4.6 (a)). A digital/analog converter with 12 Bit resolution produces an output voltage of ±10 V and can, therefore, increase the remote voltage for the power supply in steps of 5 mV. The power supply has a maximum current output of 5 A and shows a high resolution response to the applied remote control. Figure 4.6 (c) shows that each increase of the remote voltage by 5 mV results in an increase of the current output by 2.5 mA which makes this power supply the best available model tested for this purpose at the moment. The iron cores are flexibly mounted in the center of the magnetic coils to take different sample sizes into account. Thus, their positions at the time of the measurement has to be known because larger distances between the pole caps result in different magnetic field strengths (B) at the samples position. Hence, the parameter d_{core} which for practical reasons is measured at the outer side of the coils, is defined (see. Fig. 4.7 (a)) and has to be the same for all iron cores.

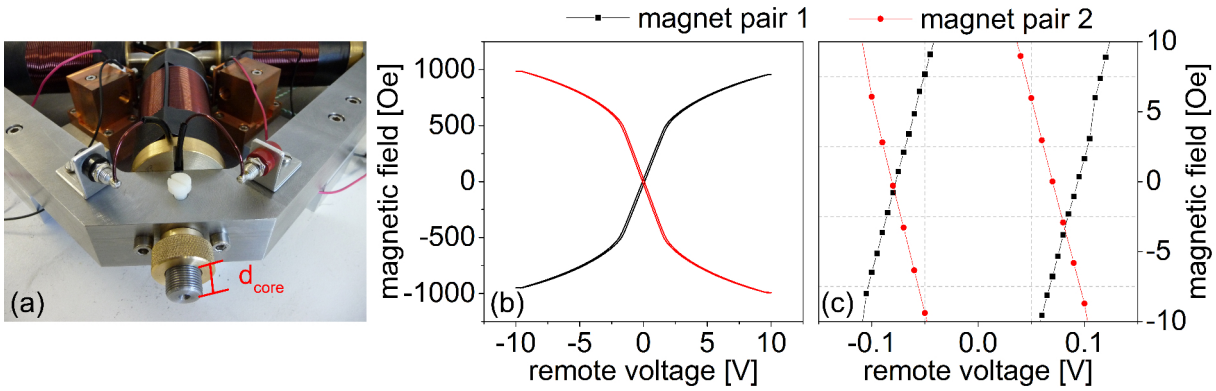

Figure 4.7.: (a) Definition of the parameter d_{core} which has to be the same for all iron cores. (b) Induced magnetic field of both magnetic pairs at the sample's center vs. the applied remote voltage. These calibration data, taken for $d_{core} = 8$ mm, are the fundamental base of the software tool which controls the magnetic field. (c) The hysteretical behavior due to the remanence of the iron cores can clearly be seen in the low voltage regime. A resolution of $\Delta B = 1.3$ Oe for low remote voltages and $\Delta B = 0.2$ Oe for high control voltages can be achieved.

Now, a third Hall sensor was positioned at the exact sample position and was subsequently orientated parallel to the direction of both magnetic axes. While sweeping the maximum range of the remote voltage for the power supply, the resulting magnetic field at the position of the sample reached $\approx 1000\,\mathrm{Oe}$ (for $d_{\mathrm{core}} = 8\,\mathrm{mm}$), see Fig. 4.7 (b). It can be seen that in the range of $\approx \pm 1.3\,\mathrm{V}$ a steep linear increase of B was achieved since in this regime the magnetization of the iron cores continuously increased. Above this regime the magnetization of the iron cores start to saturate and a further increase of B is only driven by the enhancement of the current through the coils. Also, a small hysteretic behavior due to the remanence of the iron cores can be resolved, highlighted in Fig. 4.7 (c). Here, one recognizes that the incremental increase of the remote voltage by 5 mV results in a resolution of ΔB $\approx$ 1.3 Oe in the low voltage regime ($\pm$1.3 V) down to $\approx$ 0.2 Oe in the high voltage regime (>9 V, not shown).

The developed control software for the magnetic component takes the hysteretical response into account and is based on the calibration measurements for a specified d_{core}. Note that the actual status of the setup is optimized for $d_{\mathrm{core}} = 8\,\mathrm{mm}$ and that additional calibration measurements are necessary for different d_{core}. As soon as a magnetic field has to be applied, the software tool starts with the input parameters of the net magnitude for the magnetic field $|B|$ and its in-plane angle φ, as defined in Fig. 4.2. Depending on φ the software chooses the right field direction for each magnetic axes and splits $|B|$ into the components $|B|_{MP1}$ and $|B|_{MP2}$ which have to be provided by the magnetic axes. Now, the software looks for the corresponding remote voltage in the calibration data (Fig. 4.7 (b)) and sends the command to the digital/analog converter.

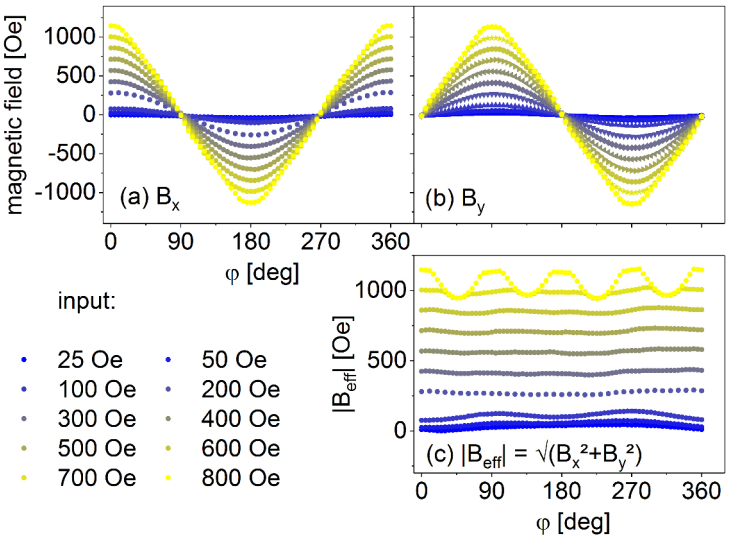

Figure 4.8.: Superimposing both magnetic axes result in the cos shaped projection of the rotated magnetic field on the x-axis (a) and the sin shaped projection on the y axis (b). Larger input fields than 600 Oe lead to more linear shaped distributions that have a large influence on the magnitude of the net field as can be seen in (c): Only for fields $\leq$600 Oe the magnitude stays constant within a maximum standard deviation of 13 Oe.

Superimposing both magnetic axes leads to the rotation of the net magnetic field. Rotating the magnetic field by the angle φ as defined in Fig. 4.2 results in the oscillating x- and y-components

$$B_\mathrm{x} = |B| \cos\varphi \tag{4.5}$$

$$B_\mathrm{y} = |B| \sin\varphi \quad . \tag{4.6}$$

Rotating magnetic fields of increasing magnitudes (25 Oe to 800 Oe input values) lead to the expected cosine (B_x) and sine (B_y) oscillations, as can be seen in Fig. 4.8 (a) and (b). Each curve is fitted by a cosine (sine) function to determine the magnitude and cosine- (sine-) like origin of the curve. Two facts can be concluded from these fits. Firstly, independent of the user input, the measured field amplitudes at the sample position exceed the input magnitude on average by 35%. This has to be taken into account as soon as the absolute maximum fields are critical. Secondly, for magnitudes $\geq$ 700 Oe the curves develop a linear shape which increasingly deviate from the trigonometric oscillations. Thus, non-homogeneous rotated net magnetic fields are obtained. The magnitude of the rotated net magnetic field is shown in Figure 4.8 (c). A constant magnitude within a standard deviation of max. 13 Oe for 200 Oe $\geq$ H $\geq$ 600 Oe input fields and the artefacts of larger fields due to the linear contributions in the x- and y- axes can be noted. Additionally, for H<200 Oe the net field also becomes inhomogenous which can be attributed to stray fields of the other magnetic core. Therefore, a working range for $d_\mathrm{core} = 8$ mm between 200 Oe and 600 Oe input is recommended.

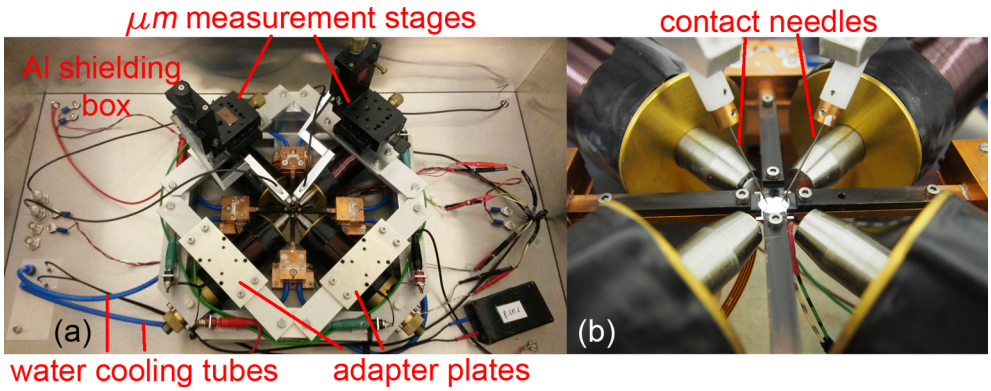

Figure 4.9.: (a) The combined thermal, magnetic and electric components were transferred into an Al shielding box to minimize electromagnetic background noise. Measurement stages were mounted on adapter plates to sensitively position Al carriers for the contact needles and data transmission cables at the center of the setup. All cables and water cooling tubes were led through an Al ground plate. (b) A closeup view of the electric connection in contact mode.

Including the 35% increase of the input magnetic field strength, the setup allows a maximum net magnetic field of 850 Oe with $\Delta B = 13$ Oe during a 360° rotation (see Fig. 4.8 (c)). The fits of the x- and y- component underlie a phase shift of up to 1.8° and make it reasonable to denote the error of φ to $\Delta\varphi = 2°$.

4.1.3. Electric component

After combining the thermal and magnetic component, the next step is to integrate the detection of the electric signal. The future use of e.g. Hallbars makes a fine positioning of the electric contacts necessary. Hence, the use of 3D μm measurement stages is obligatory. A mechanical mount system with four adapter plates configured for different types of measurement stages (OWIS, Staufen, Germany) is designed and mounted on top of the magnetic component (see Fig. 4.9 (a)). The complete setup is transferred into an aluminum shielding box to minimize electromagnetic background noise in the measurements. All electric wires and tubes for the water cooling system (blue tubes in Fig. 4.9 (a)) are led through an Al ground plate to enable a shielding in all spatial directions and suppress the electromagnetic noise to a minimum. From the measurement stages Al holders lead to the center of the setup and are used as carriers for the contact needles and the wires for data transmission (temperature stable, flexible capton wires with 1 mm diameter, Allectra, Germany). Figure 4.9 (b) shows a closeup view with the contact needles in experimental contact mode.

The influence of the Al shielding box is shown in Fig. 4.10. Here, the background voltage measured by two contact needles (without heating) on a platinum stripe is shown. A suppression of the RMS noise from ≈ 50 nV (without shielding) down to ≈ 10 nV (with shielding) can be observed. Therefore, it is highly recommended to use the Al box for all electric measurements.

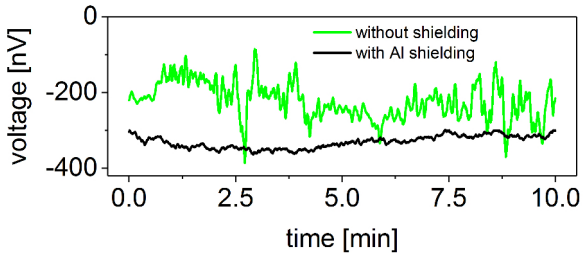

Figure 4.10.: Comparison of the RMS noise level in the background voltage without and with the Al shielding box (without heating). A suppression from 50 nV to 10 nV could be achieved.

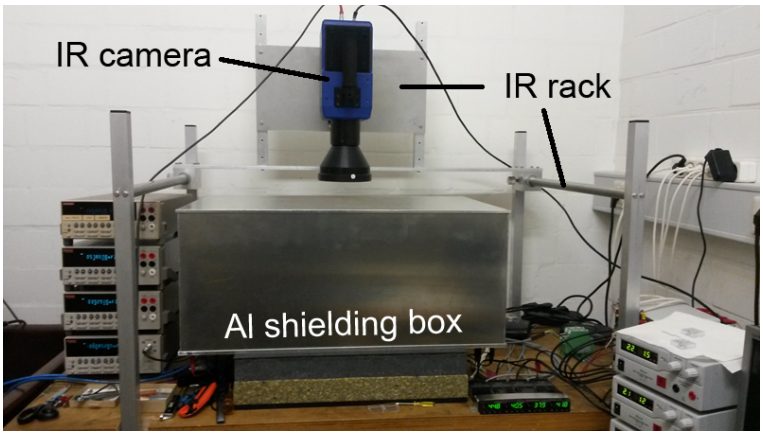

Figure 4.11.: The infrared camera is mounted on a flexible rack above the experimental setup. The setup itself is put into an aluminum shielding box.

Additionally, another contact method has been established to further enhance the signal-to-noise ratio and temperature stability. 25 μm thin Au wires are bonded on the sample and its ends were glued to Au probes with silver paste. The electric signal is detected by a Keithley 2182A nanovoltmeter. The lastly described method is used in the studies shown in this work.

4.1.4. Infrared component

In order to verify the successful rotation of ∇T optically, a FLIR SC7000 infrared camera is used. It is mounted 50 cm vertically above the setup on an external rack which allows its alignment in the x-, y- and z-direction. Figure 4.11 shows an overview of the spatial arrangement of the infrared camera above the shielding box. For the optical detection, the top of the shielding box was taken off.

All materials emit electromagnetic waves ranging from ultraviolet or even X-ray regions for hot temperatures down to the infrared spectrum near room temperature. For our setup, temperatures between room temperature and 100° C play a role and, thus, heat radiation in the infrared regime of the electromagnetic spectrum is most important ($\lambda_{photon} = 700\,\text{nm} - 1\,\text{mm}$) [102].

The SC7000 camera uses an Indium antimonide (InSb) sensor which is sensitive to the mid-wave infrared radiation between 3 to 5 μm.

The camera's sensor absorbs the emitted infrared energy and converts it to an electric signal. The signal is transmitted to a computer which calculates the temperature and displays it with a color code. This is done by following Wien's displacement law for black body radiation [103],

$$\lambda_{max} = \frac{b}{T} \quad , \tag{4.7}$$

with Wiens constant $b = 2.898 \cdot 10^{-3}$ m K. Note that this is only possible if the emissivity coefficient of a material is known because the emitted energy is a material dependent parameter [102]. For this reason, it is necessary to equalize the emissivities of all recorded materials in the optical experiments. This is done by evaporating a highly absorbing, thin layer of clustered Au particles under nitrogen atmosphere on the investigated substrates and the sample holder (see Fig. 4.9 (b)), following Ref. [104]. This procedure thermally equalizes all involved materials to an equal emissivity and enables a quantitative comparison of different materials.

Extracting the experimentally obtained parameters T_{base}, ∇T and φ_{T} is done by using two software tools. Firstly, the firmware *FLIR ResearchIR* is used to control the IR camera, set calibration parameters, e.g., the emissivity and directly picture the thermal distribution. Due to the resolution of 320x256 pixels the software allows to export the raw temperature data into a 320x256 matrix data file,

$$T = \begin{bmatrix} T_{1,1} & \dots & T_{1,320} \\ \vdots & \ddots & \vdots \\ T_{256,1} & \dots & T_{256,320} \end{bmatrix} \quad . \tag{4.8}$$

Secondly, the exported data file is analyzed by a custom written MATLAB script, which was developed with the help of Dr. M. Simonis. This MATLAB script allows to define a region of interest (ROI) which determines a circular area in the center of the sample for analysis. Then, ∇_{x} and ∇_{y} are calculated for each element $T_{\mathrm{i,j}}$ leading to two separate matrices $\nabla_{\mathrm{x}}T$ and $\nabla_{\mathrm{y}}T$. The mean average of each matrix is then given by

$$\overline{\nabla_{\mathrm{x,y}}\mathrm{T}} = \sum_{i,j} \frac{\nabla_{\mathrm{x,y}} T_{\mathrm{i,j}}}{dim(\nabla_{\mathrm{x,y}}T)} \quad , \tag{4.9}$$

regarding the possibility of surface defects, e.g., scratches or particles, influencing the optical detected thermal distribution. $\overline{\nabla_{\mathrm{x,y}}T}$ represent the x- and y-component of the total thermal gradient within the aforementioned ROI. Depending on the sign of $\overline{\nabla_{\mathrm{x,y}}\mathrm{T}}$, φ_{T} can be calculated using trigonometric calculations.

One exemplary result of this calculation is visualized in Fig. 4.12 on top of the raw temperature data. Figure 4.12 (a) shows the ROI (area of gray circle), ∇T (the white arrow which scales with $|\nabla T|$) and φ_T (angle embedded between the x-axis and ∇T along the white arc and number in

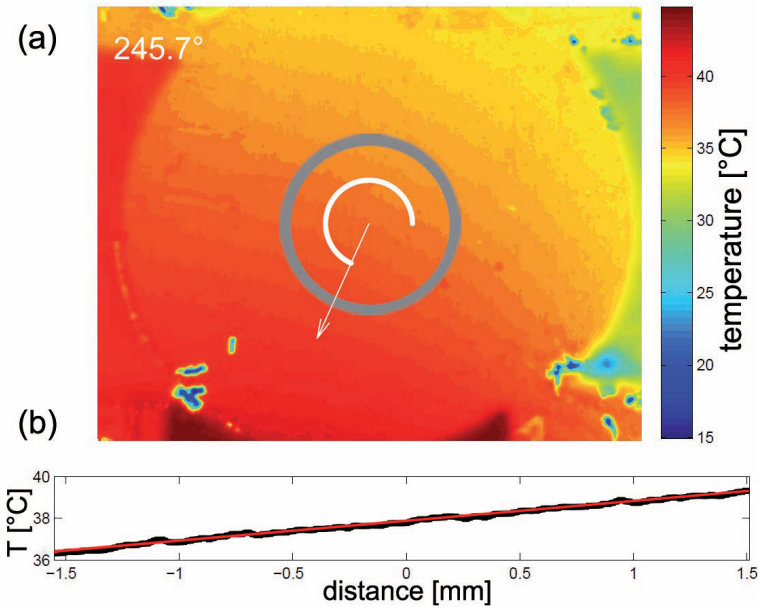

Figure 4.12.: (a) A thermographic picture after applying a thermal gradient with $\varphi_{\mathrm{T,in}} = 240°$ on a pure Cu substrate. The ROI (gray circle) indicates all data points which are used to calculate the resulting angle $\varphi_{\mathrm{T,out}} = 245.7°$. The white arrow points in the direction of the average ∇T and scales with $|\nabla T|$. (b) The thermal profile (black) along $\varphi_{\mathrm{T,\,out}}$ can be fitted linearly (red) to additionally obtain T_{base} (origin of fit) and ∇T (slope of fit).

upper left corner). Here, the four sample holders as well as thermal artifacts (e.g. lower right corner) can be resolved. For reasons of homogeneity the diameter of the ROI (and later the measured electric structures, e.g. Hallbars) should not exceed 40 % of the picture's y-dimension ($\approx$ 3 mm).

Knowing the average angle of ∇T allows the extraction of all data points along that direction and plotting them versus the position within the ROI (see Fig. 4.12 (b)). Since the center of the ROI also represents the center of the sample, the intersection of a linear fit of the thermal profile with the y-axis is equal to T_{base} and its slope to ∇T. In this manner, the rotation of ∇T can be visualized, making a detailed investigation of ∇T depending on different input parameters possible.

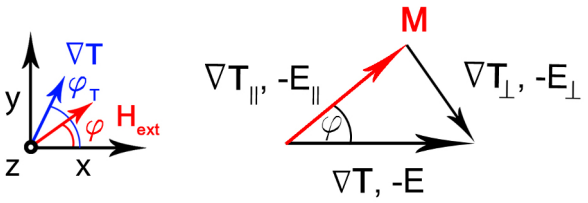

Figure 4.13.: Definition of the angle of the thermal gradient.

4.1.5. Theoretical modification of the anisotropic magnetothermopower

Since in this study the rotation of ∇T in the xy-plane is utilized whereas the electric contacts stay fixed along the y-axis, a superposition of the AMTP and PNE is expected for orientations of ∇T between the x- and y-axis directions. Because of the additional angle φ_T in the measurement geometry (Fig. 4.13), the equations of the longitudinal and transverse AMTP have to be modulated. Assuming a measurement of the AMTP along the x-direction for rotated ∇T, Eq. (3.36) changes to

$$E_{\mathrm{x}} = -\left(\frac{S_{||}+S_{\perp}}{2} + \frac{S_{||}-S_{\perp}}{2}\cos 2\varphi\right)|\nabla T|\,\cos\varphi_T \quad , \tag{4.10}$$

because of the projection of ∇T onto the x-axis. Similarly, Eq. (3.38) for the PNE (transverse AMTP) changes to

$$E_{\mathrm{y}} = -\frac{S_{||}-S_{\perp}}{2}\sin 2\varphi\,|\nabla T|\,\cos\varphi_T \quad . \tag{4.11}$$

Now, it has to be taken into account that the AMTP is measured along the y-axis and the angles in Eq. (4.10) are defined with respect to the x-axis. Therefore, an angle phase shift has to be introduced which considers that the (longitudinal) AMTP is measured along the y-axis. Keeping the angles defined regarding the x-direction shifts E_{y} by 90°, leading to

$$\begin{aligned} E_{\mathrm{y}} &= -\left(\frac{S_{||}+S_{\perp}}{2} + \frac{S_{||}-S_{\perp}}{2}\cos\left(2(\varphi-90°)\right)\right)|\nabla T|\,\cos(\varphi_T-90°) \\ &= -\left(\frac{S_{||}+S_{\perp}}{2} - \frac{S_{||}-S_{\perp}}{2}\cos 2\varphi\right)|\nabla T|\,\sin\varphi_T \quad . \end{aligned} \tag{4.12}$$

Hence, Eq. (4.12) describes the longitudinal AMTP and

$$E_{\mathrm{y}} = -\frac{S_{||}-S_{\perp}}{2}\sin 2\varphi\,|\nabla T|\,\cos\varphi_{\mathrm{T}} \tag{4.13}$$

the transverse magnetothermopower (PNE) measured along the y-direction. Since the experiment will measure the AMTP and PNE simultaneously, the superpositioned electric field along the

y-direction is described by

$$E_{\mathrm{y}} = -(S_{+} \sin\varphi_{\mathrm{T}} + S_{-} \sin(2\,\varphi - \varphi_{\mathrm{T}}))|\nabla T| \tag{4.14}$$

with $S_{+} = \frac{S_{||}+S_{\perp}}{2}$ and $S_{-} = \frac{S_{||}-S_{\perp}}{2}$, showing that a variation of φ_{T} leads to a phase shift of E_{y}.

4.2. Magneto(thermo)electric investigation of Co/Pd multilayers

Based on previous experiments, this section gives an overview of the experimental and theoretical improvements of the magneto(thermo)electric investigation of Co/Pd multilayers.

4.2.1. Sample preparation

The magnetic multilayers are grown on thermally oxidized Si (500 μm)/SiO_2 (500 nm) substrates using magnetron sputter deposition (CLAB 600, Leybold Vakuum GmBH). The base pressure is kept below 3 x10^{-7} mbar to minimize impurities and the deposition process takes place at room temperature. First, a Ta(5 nm) buffer layer is deposited on the substrate to enhance the stacking coefficient, followed by the deposition of a 9x repetition of a Co(x nm)/Pd (1.5 nm) bilayer (x = 0.075, 0.1, 0.125, 0.15, 0.175, 0.2, 0.225, 0.25, 0.3, 0.35, 0.4, 0.45, 0.6). It was shown that Co/Pd multilayers posses a PMA [105, 106, 107] which can be further stressed by either increasing the number of repeats [108] or by post annealing under an oop magnetic field [109]. Because this work continues studies conducted on 9x repetition of ($Co/Pd_{1.5nm}$) multilayers, the post annealing procedure is chosen. A systematic alternating-gradient magnetometer study investigated the influence of the post annealing temperature and Co thickness on the saturation and remanence magnetization, M_s and M_r, respectively [109]. It was found that for temperatures between 200° and 350° the highest values of M_s and M_r could be obtained for Co thicknesses between 0.3 nm to 0.55 nm. In addition, the planned experiment is conducted to up to 250°. Since any structural changes within the samples due to high temperatures during the experiment have to be excluded, all samples are post annealed at higher temperatures. Therefore, they are heated at 350° C for 60 min with an applied oop magnetic field of 6500 Oe.

Figure 4.14 shows x-ray reflectivity measurements (XRR) of (a) the 0.15 nm and (b) 0.2 nm Co multilayer in the as prepared and post annealed state. Here, the intensity of x-rays which are reflected at the interfaces of the crystal lattice is measured for increasing incidence angle Θ. Depending on the distance of the involved interfaces, constructive interference is observed for specific angles, resulting in oscillation patterns. These patterns allow to reconstruct the interface quality, roughness, density of involved materials and film thicknesses. As can be seen in Fig. 4.14 (a) and (b), for both samples the heating process enhances the interlayer quality and roughness, displayed by the improved oscillations for 2Θ angles above 5°. By fitting the post annealed spectra, estimations of the total thickness t_{tot} can be made. The fits are shown in Fig. 4.14 (c) and (d) and agree with the experimental data reasonably well. They result in t_{tot}=19.19 nm and 19.47 nm, which are close to the expected values of t_{tot}=19.85 nm and 20.3 nm, respectively. However, not only the reflection from the top and bottom of the complete multilayer causes interference, also the regularly repeated top and bottom interfaces of each Co/Pd bilayer result in intensity oscillations. These Bragg peaks are expected at higher angles due to the thinner thickness of the bilayer and superimpose the signal of the interference of x-rays from top and bottom of the whole multilayer stack. Hence, they are often detected as oscillations with higher intensity compared to the normal peaks. The first order Bragg peak can clearly be identified for

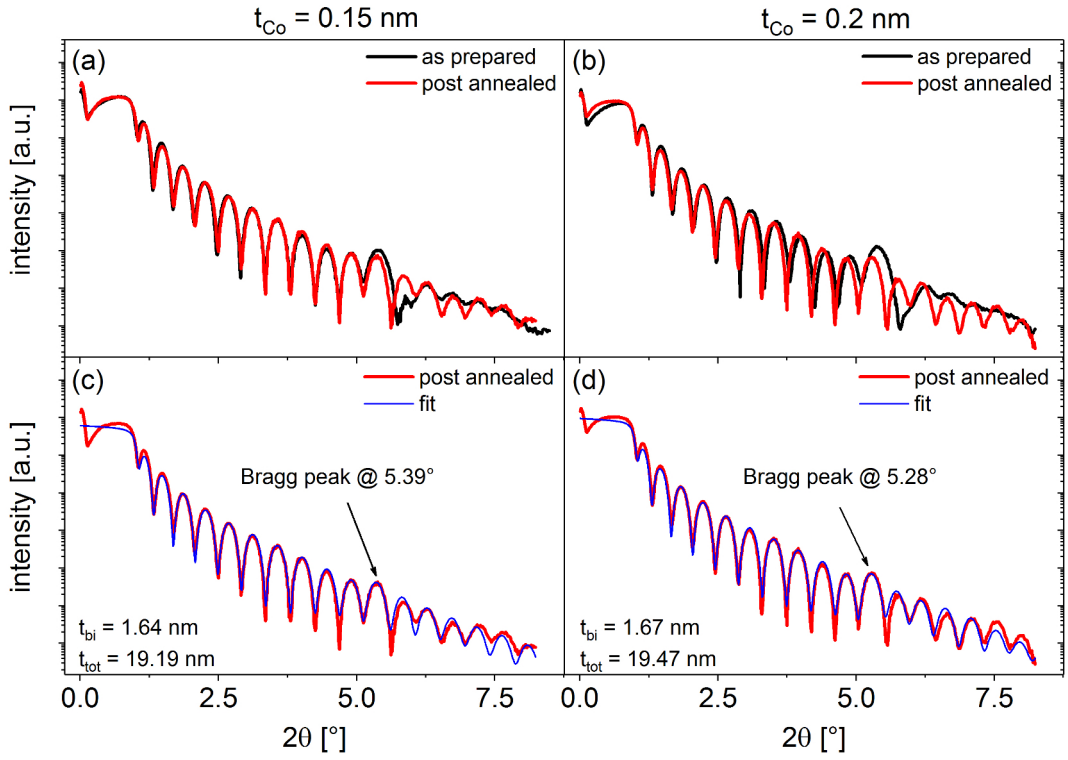

Figure 4.14.: XRR spectra of the (a) $(Co_{0.15nm}/Pd_{1.5nm})_{9x}$ and (b) $(Co_{0.2nm}/Pd_{1.5nm})_{9x}$ multilayer for the as prepared and post annealed state. The enhanced oscillations suggest a higher interface quality in both samples due to post annealing. The post annealed spectra are fitted (c), (d) and in addition with the Bragg peaks confirm the sputtered film thicknesses and bilayer periodicity.

both samples in the as prepared state but are also visible after post annealing at $2\Theta = 5.39°$ and 5.28°, respectively. With Bragg's law the bilayer thickness can be calculated to be $t_{bi} = 1.64\,nm$ and 1.67 nm which again agree with the expected bilayer thicknesses of 1.65 nm and 1.7 nm. Hence, the expected layout of the sputtered multilayer systems are verified and their structural quality is not altered by the post annealing process.

The PMA of each multilayer is proven by the polar magneto optical Kerr effect (PMOKE) in the oop configuration. Here, a laser beam is reflected at a samples surface and recorded by a photo diode. Depending on the oop component of the magnetization of the sample, the PMOKE rotates the polarization angle of the reflected laser beam in comparison to the incident beam. This Kerr rotation is recorded as a function of an oop magnetic field sweep which switches the magnetization from the magnetic easy axis (oop) to the hard axis (ip) and back to the easy axis (oop) again. Again, these measurements are done for each multilayer in the as prepared and post annealed state and are shown in Fig. 4.15. Here, it can be seen that for the lowest Co content no signal could be obtained, showing that these Co films are too thin to introduce an oop magnetic component. For $t_{Co} = 0.125\,nm$ the Kerr rotation starts to increase but only shows a magnetic hard axis behavior. Only for $t_{Co} = 0.15\,nm$ the signal exhibits a fast switching for low magnetic

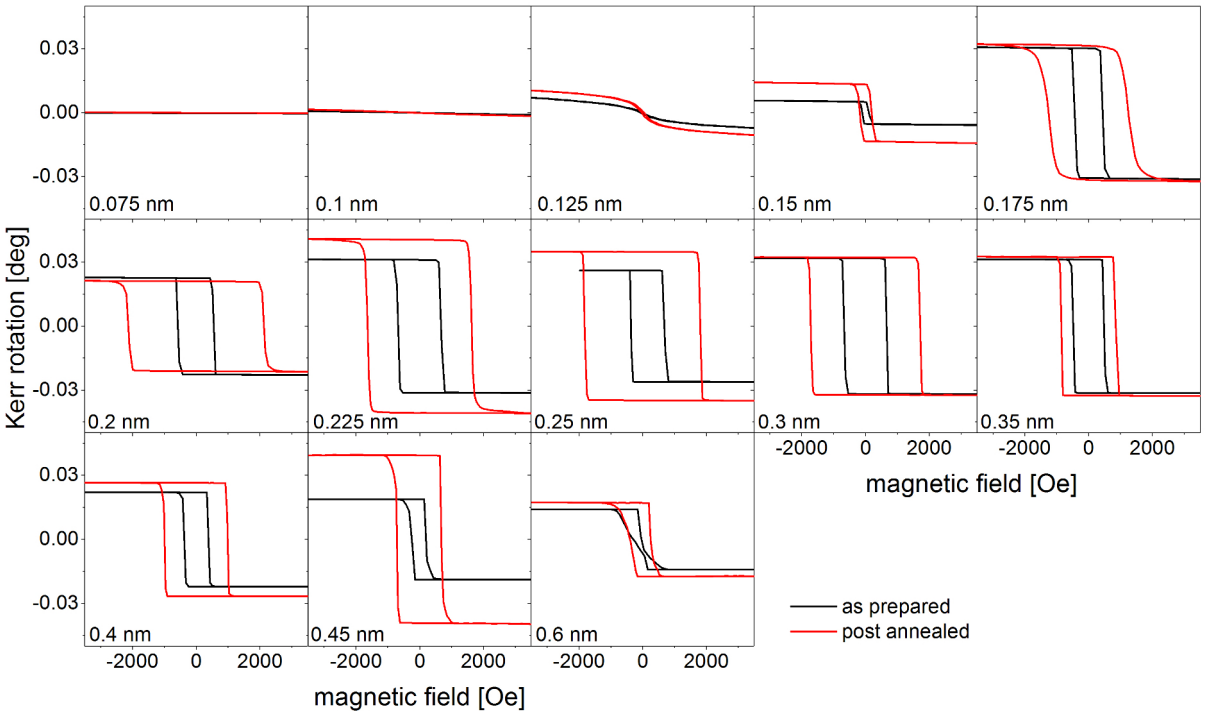

Figure 4.15.: PMOKE measurements in the oop configuration show an oop magnetic easy axis for increasing Co thicknesses. For the highest t_{Co}, the easy axis starts to tilt from oop to ip due to the increasing influence of the ip shape anisotropy compared to the oop interface anisotropy.

fields, indicating the development of an oop magnetic easy axis. For $0.175\,\text{nm} \geq t_{Co} \geq 0.45\,\text{nm}$ the coercive fields and magnitude of the Kerr rotation stay relatively constant, until for the thickest sample both parameters decrease. This can be explained by a change of the interface and bulk contributions to the magnetic anisotropy energies which determine the orientation of the magnetization. Whereas for thin Co films the interface contribution leads to an preferred oop orientation, the bulk contribution results in ip magnetizations for thick Co samples. It has been shown that the critical thickness of Co, where the ip magnetization switches to oop orientation, is 0.76 nm in $(Co/Pd)_{9x}$ multilayers [109]. This agrees well with the shown data. The most striking difference of the post annealed multilayers are the generally increased coercive fields of all multilayers.

Figure 4.16 highlights the influence of the post annealing process on the magnitudes of the Kerr rotation (a), the coercive fields (b) and the squareness $\left(\frac{\text{remanence Kerr rotation}}{\text{saturation Kerr rotation}}\right)$ (c). While a systematic increase of the Kerr rotation can not be observed for the post annealed samples, the coercivity is highly improved for all samples. Especially in the regime of $0.175\,\text{nm} \geq t_{Co} \geq 0.3\,\text{nm}$ an increase by a factor of up to 3 can be seen. Thus, the post annealing process enhances the collective coupling between the magnetic domains, resulting in higher fields necessary to switch the magnetization. Nevertheless, the constant squareness of 1 for $t_{Co} > 0.175\,\text{nm}$ indicates that a magnetic easy axis is obtained in the oop orientation for all samples which is not negatively

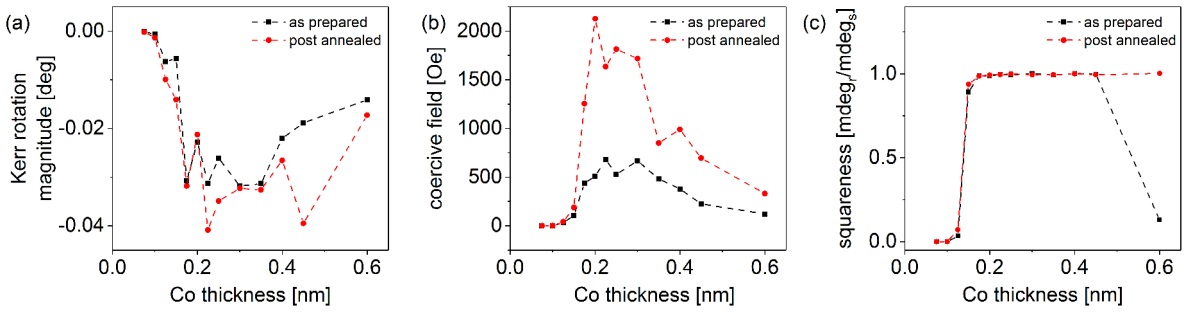

Figure 4.16.: (a) Kerr rotation magnitude, (b) coercive fields and (c) squareness of PMOKE measurements comparing the as prepared and post annealed state of the multilayers. A clear enhancement of the coercive fields due to the post annealing hints to a stronger collective coupling between the magnetic domains. The constant squareness of 1 for $t_{\mathrm{Co}} > 0.175\,\mathrm{nm}$ verifies a perpendicular magnetic easy axis.

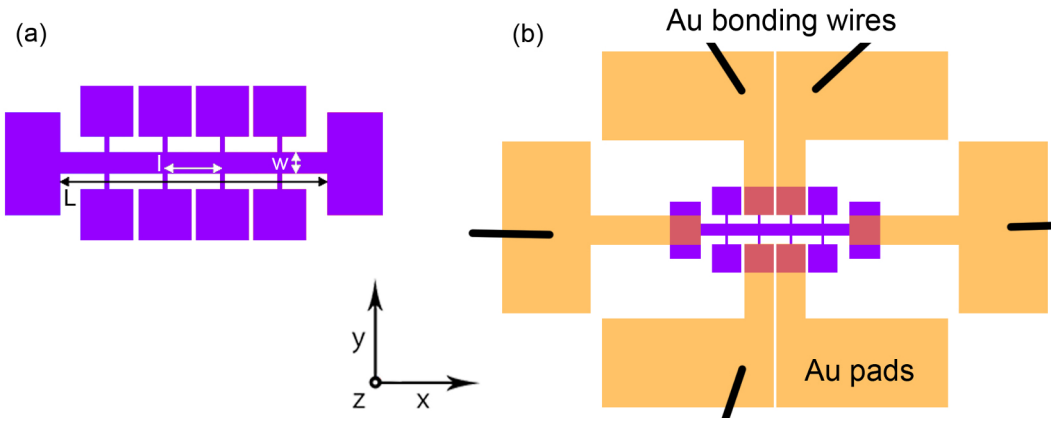

Figure 4.17.: (a) A Hallbar with the dimensions L = 1100 μm, l = 220 μm and w = 80 μm was etched into the multilayers. (b) A second lithography step provided Au contact pads.

influenced by the post annealing process.

Since the XRR and PMOKE measurements are conducted on planar samples, a structuring process for the electric measurements is necessary. Hence, the samples are patterned via UV-lithography and Ar etching into Hallbar structures with the dimensions L = 1100 μm, w = 80 μm, l = 220 μm and the varying total thickness $\mathrm{t_{tot}} = (t_{\mathrm{buffer}} + 9t_{\mathrm{Co}} + 9t_{\mathrm{Pd}}) = (19.6 + 9t_{\mathrm{Co}})\,\mathrm{nm}$ (see Fig. 4.17 (a)). A second lithography step provides large Au contact pads for low contact resistances after bonding with 25 μm thin Au wires, as depicted by Fig. 4.17 (b).

4.2.2. Experimental setup

Performing comparable ANE and AHE measurements under similar experimental conditions to reliably extract quantitative temperature dependent parameters is a challenging task. Since ∇T

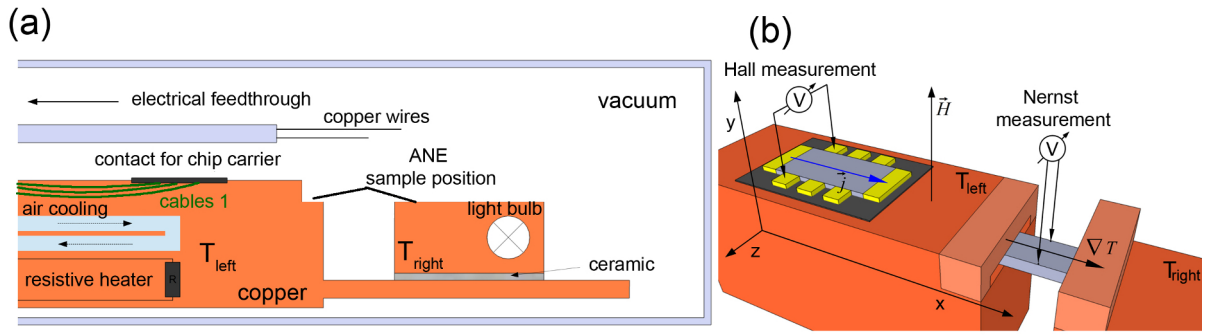

Figure 4.18.: (a) Scheme of vacuum furnace. (b) Mount of the AHE and ANE samples in the study by T. Matalla-Wagner [111].

has to be constant but applied in a temperature range above room termperature, the use of a vacuum furnace is necessary. Additionally, the need of an oop magnetic field rules out the use of the newly developed setup described in the last section. Hence, a vacuum furnace is used which is described in detail elsewhere [110, 111, 112] but an overview is depicted in Fig. 4.18 (a). Basically, a resistive heater (heater_A) provides the heat for the left copper block and a light bulb (heater_D) which is mounted into another, thermally decoupled, copper block provides the heat at the right copper block.

The first experiments comparing the AHE and ANE on Co/Pd multilayers have been conducted by T. Matalla-Wagner [111]. In this study, on one hand, a temperature range of $320\,\text{K} \leq T_\text{left} \leq 420\,\text{K}$ was investigated in terms of the AHE and ANE for $t_\text{Co} = 0.2\,\text{nm}$, $\Delta T = 8\,\text{K}$ and $I_\text{DC} = 500\,\mu\text{A}$. On the other hand, different t_Co were investigated at $T_\text{left} = 320\,\text{K}$ with $\Delta T = (9.7 \pm 1.1)\,\text{K}$. Note that two individual samples, but prepared under same conditions were used to compare AHE and ANE signals. Figure 4.18 (b) shows one Hallbar structured sample mounted on the left Cu block for AHE measurements and another planar, non-structured sample for ANE measurements mounted between the left and right Cu block, hence, being exposed to ∇T. Two issues arise from this experimental design. Firstly, a structured sample is compared with a planar sample. This only unambiguously defines the Hall resistivities whereas the Nernst signals may originate from different sample sizes, contact distances and non-homogeneous electrical contact alignments. Secondly, due to the different sample positioning of the AHE and ANE samples the base temperature of both measurements were not equal, since $T_\text{base,AHE} = T_\text{left}$, whereas $T_\text{base,ANE} = T_\text{left} + \frac{\Delta T}{2}$.

To eliminate the uncertainties due to different sample positions and structured vs. planar films the continuing study of M. van Straaten [112] combined the measurement of the AHE and ANE into one sample design. Here, both measurements were conducted on the same Hallbar. Additionally, the samples were glued and bonded with Al wires onto small cryogenic chip carriers (Fig. 4.19 (a)), leaving araound 3 mm of free-standing substrate at each side to clamp the sample with thermal conductive paste into the same sample holder as before. The free-hanging chip carrier allowed to connect all six contact pads of the Hallbar, the application of a longitudinal current and the measurement of the transverse voltages (Fig. 4.19 (b)).

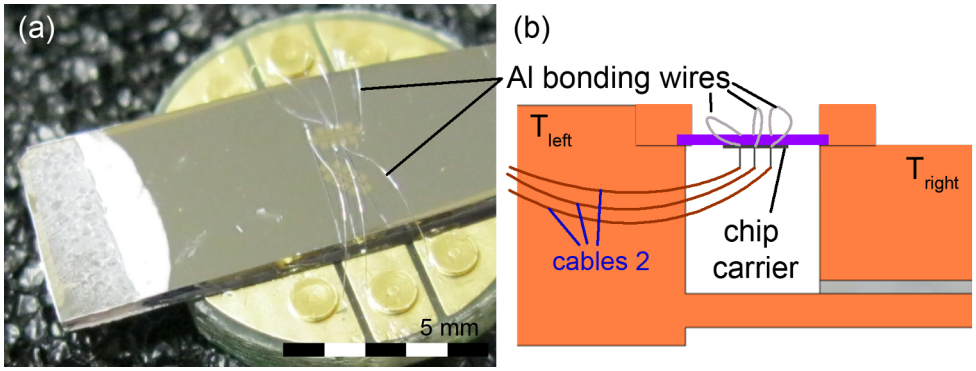

Figure 4.19.: (a) 1.5 cm long substrate pieces with the Hallbar structured multilayers were glued and bonded on chip carriers [112], (b) which were then clamped in the same sample holder as in the previous study (based on Ref. [111]).

This contacting method enabled the investigation of both effects at the same sample and, thus, should lead to more comparable results. Three measurement modes were used for investigations. Firstly, the AHE was measured for increasing T_{base}, increasing t_{Co}, with a direct current of $I = 500\,\mu A$ but with $\Delta T = 0\,K$ (mode 1). Secondly, the ANE was recorded for the same range of T_{base} and t_{Co} but with $\Delta T = 20\,K$ and $I = 0\,\mu A$ (mode 2). Comparing the effect magnitudes for different T_{base} and t_{Co} point to a sign change of the AHE (as also seen by Keskin *et al.* [94]) but none in the ANE for increasing T_{base}. However, due to the changing thermal conditions between the AHE and ANE measurements, a quantitative comparison of the results of measurement mode 1 and 2 are questionable. Thus, measurement mode 3 was used to measure the AHE and ANE under same thermal conditions. Here, $\Delta T = 20\,K$ and the direct current $I = 500\,\mu A$ were simultaneously applied along the x-axis while the transverse voltage V_y was measured. Due to the same geometry of the AHE and ANE, the resulting voltage V_y consists of the superimposed signal of the AHE and ANE. In a second step, the current direction was inverted, leading to an inverted AHE signal but because of the same direction of ΔT not changing the ANE contribution. These two signals could be used to split the thermally induced ANE and electrically induced AHE contributions. Whereas the magnitudes of the AHE of mode 1 and 3 showed very good agreement, the deviations of the ANE between mode 2 and 3 were larger and could only be compared qualitatively.

As shown in Sec. 3.3, the thermoelectric conductivities could be fitted by knowing the electric resistivities if the Mott relation is valid for the present multilayer systems. The quantitative analysis of the data of M. van Straaten's study in terms of the Mott relation turns out to be problematic since too many unknown parameters prevent the determination of the pure Seebeck coefficient of the multilayers. These issues were taken into account to further improve the experimental setup for a quantitative comparable study between the AHE and ANE.

Figure 4.20 (a) illustrates the thermal circuit which describes the sample mount of M. van Straaten's study implying all involved thermal resistances with their corresponding Seebeck coefficients. The Seebeck voltage is measured along two longitudinal contacts of the Hallbar, but

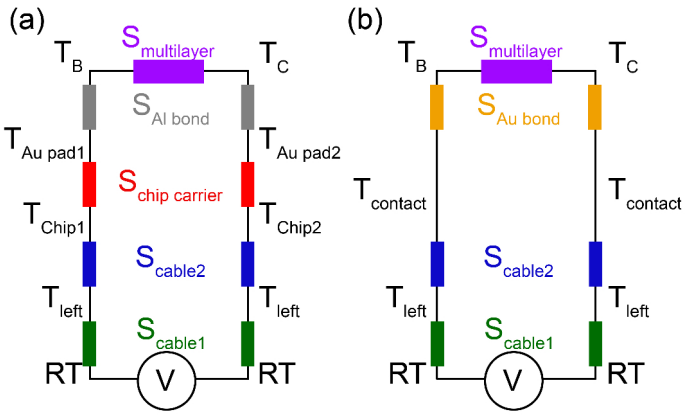

Figure 4.20.: (a) Thermal circuit of the experiment by M. van Straaten including all thermal resistances and Seebeck coefficients, (b) thermal circuit of updated setup reducing experimental uncertainties.

it is important to consider all involved materials being exposed to a ΔT. Following the scheme and the general formula $V_{\text{Seebeck}} = -S\,\Delta T$, the net measured voltage $\mathrm{V_{total}}$ can be written as

$$\begin{aligned} V_{\text{total}} = &- S_{\text{cable2}}(T_{\text{chip1}} - T_{\text{left}}) - S_{\text{carrier}}(T_{\text{Au pad 1}} - T_{\text{chip1}}) \\ &- S_{\text{bond}}(T_B - T_{\text{Aupad1}}) - S_{\text{multilayer}}(T_C - T_B) - S_{\text{bond}}(T_{\text{Aupad2}} - T_{\text{C}}) \\ &- S_{\text{carrier}}(T_{\text{chip 2}} - T_{\text{Aupad2}}) - S_{\text{cable2}}(T_{\text{left}} - T_{\text{chip2}}) \quad , \end{aligned} \tag{4.15}$$

demonstrating that the exact Seebeck coefficient of the multilayers can only be determined if the Seebeck coefficients $\mathrm{S_{cable2}}$, $\mathrm{S_{carrier}}$, $\mathrm{S_{bond}}$ as well as the temperatures $\mathrm{T_{chip1}}$, $\mathrm{T_{Aupad1}}$, $\mathrm{T_{Aupad2}}$ and $\mathrm{T_{chip2}}$ were known. The largest uncertainty in this equation is clearly given by the chip carrier, since neither its Seebeck coefficient nor its temperatures on the top Au bonding pads or on its bottom at the connections to cable 2 can be quantified. Also the usage of Al bonding wires which have a production charge dependent content of Si implies a large uncertainty in the Seebeck coefficient of the bonding wires.

To avoid these uncertainties and to be able to calculate the exact Seebeck coefficient of the multilayers the usage of a chip carrier is avoided for the following experiments. Also, the bonding wires are changed from Al wires to Au wires (Au HD2, Heraeus, 99.99% purity) for which the Seebeck coefficient is known from literature [101]. For reasons of mechanically stable connections of the Au bonding wires, the use of Au contact pads on the Hallbar structure is necessary, so that a second lithography step is conducted for patterning (see. Fig. 4.17 (b)).

Figure 4.21 illustrates the mount of the sample into the vacuum furnace without a chip carrier. Six bonding wires are bonded on the Au contact pads of the Hallbar and simply cut at the other end. The loose ends are glued with temperature stable silver paste to six electric contacts which close the electric circle to the cables 2 (Fig. 4.21 (a)). Note that all electric contacts are at the same temperature $\mathrm{T_{contact}}$ due to the same position on the left copper block (see Fig. 4.21 (b)). The changed configuration leads to an adjusted thermal circuit as depicted in Fig. 4.20 (b). As

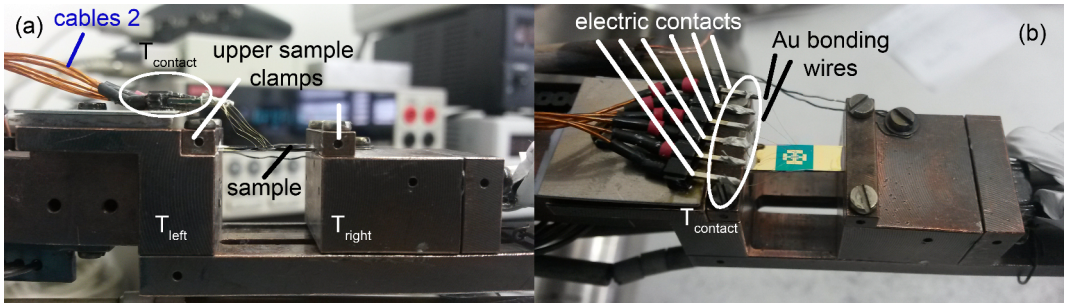

Figure 4.21.: (a) Sideview and (b) topview of the sample holder showing the Hallbar structured sample, both heatbaths, bonding wires and electric contacts.

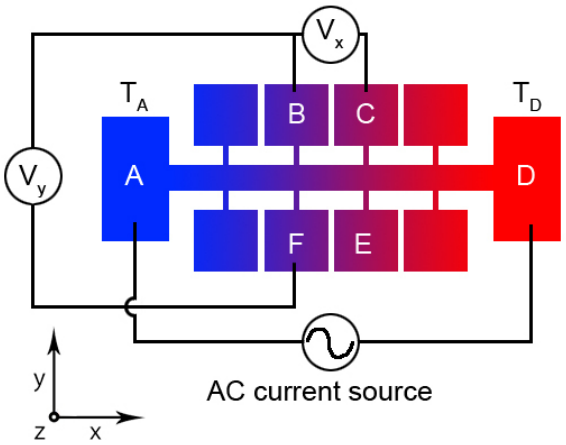

Figure 4.22.: The sample is exposed to $\nabla T \parallel \vec{x}$. The voltages V_x and V_y are measured, once, without applied current and, second, with an applied alternating current through the contact pads A and D.

before, the cables 1 lead from room temperature to T_{left}, but in contrast, the cables 2 underlay the same thermal difference $|T_{contact} - T_{left}|$ for both sides of the thermal circuit. Therefore, without the chip carrier, Eq. (4.15) simplifies to

$$\begin{aligned} V_{tot} &= -S_{bond}(T_B - T_{contact}) - S_{multilayer}(T_C - T_B) - S_{bond}(T_{contact} - T_C) \\ &= -S_{bond}(T_B - T_C) - S_{multilayer}(T_C - T_B) \quad . \end{aligned} \tag{4.16}$$

With an estimation for $T_C - T_B$ as shown in Sec. 4.2.3 and $S_{bond} = S_{Au}$ the Seebeck coefficient $S_{multilayer}$ can be concluded.

But not only the sample mount has been adjusted in comparison to the last studies, also the electric measurement modes are improved to ensure the most stable thermal conditions and clearest signals for both the AHE and ANE experiments. For reasons of better overview the electric contacting of the Hallbar is shown without the Au contact pads, see Fig. 4.22. The Hallbar is exposed to $\Delta T = 30$ K along the +x-axis, for $45°\,C \leq T_{base} \leq 245°\,C$ in steps of 20 K for all ANE and AHE measurements. At each T_{base}, two measurement modes are conducted,

each recording V_x (between contact pads B and C) and V_y (between contact pads B and F) in dependence of an applied magnetic field $+H \parallel +z$. To avoid parasitic Hall effect contributions in the Nernst measurements, only ΔT is applied as a current driving force in the first measurement mode. Here, V_x^{therm} will be induced by the magnetic field independent, ordinary Seebeck effect, which will be denoted as $V_x^{Seebeck}$ (measured by a Keithley 2000 multimeter in DCV mode) and V_y^{therm} by the superposition of the ONE and ANE (measured by a Keithley 2182A Nanovoltmeter). In the second measurement mode, while not changing the thermal conditions, the contact pads A and D are additionally connected to a home built current supply, which is controlled by an external function generator (SFG-1013, GW Instek). This delivers an alternating current of $500\,\mu$A amplitude with f = 117 Hz through the Hallbar, hence, working as a second current driving force in addition to ∇T. Now, the voltage V_x^{elec} is detected in ACV mode (by a Keithley 2000 multimeter) that cancels out the DC component driven by ∇T. Since the electric resistance in magnetic materials is influenced by its magnetization direction, this measurement resolves the AMR and is therefore denoted as V_x^{AMR}. Also, V_y is a superimposed signal of a transverse thermally and electrically driven component. To be sensitive only to the electric component, a Lock-In amplifier (SR850, Scientific instruments) measures the first harmonic signal of V_y in differential mode, since the Hall effect contribution directly scales with the modulation of the current. Thus, the measured voltage along the y-axis in the second measurement mode will be denoted as V_y^{elec}. Note that similar to V_y^{therm}, V_y^{elec} is a simultaneous measurement of the OHE and AHE. Using the Lock-In technique avoids parasitic contributions of heating currents or current offsets and allows the unambiguously separation of the ANE and AHE.

4.2.3. Calculating electric and thermal transport coefficients

In the following, one ends up with two voltage signals for each measurement mode. The signal processing and assumptions of experimental errors will be discussed in this section.

Figure 4.23 (a) shows an exemplary measurement of the longitudinal voltage in measurement mode 1, $V_x^{Seebeck}$. As expected, the Seebeck voltage does not depend on the magnetic field, thus, the mean value of all data points is taken as the representative voltage $\overline{V}_x^{Seebeck}$ for each measurement and the standard deviation $\sigma\left(\overline{V}_x^{Seebeck}\right)$ as its error value. Now, $\overline{V}_x^{Seebeck}$ equals V_{tot} of Eq. (4.16) and consists of the Au bond and multilayer's Seebeck contributions. Since $\Delta T = T_{right} - T_{left}$ is known for all experiments, $\nabla T = \frac{\Delta T}{D}$ can be calculated with the length D of the sample which was clamped between both heaters. The distance of the longitudinal contact pads l can in turn be used to calculate the temperature difference $\Delta T_{CB} = (T_C - T_B) = \nabla T\, l$ between the contact pads C and B. This leads to the expression

$$\begin{aligned} S_{multilayer} &= -\left(\frac{\overline{V}_x^{Seebeck} + S_{Au}\,(T_B - T_C)}{T_C - T_B}\right) = -\left(\frac{\overline{V}_x^{Seebeck} + S_{Au}\,(-\frac{\Delta T}{D}\,l)}{\frac{\Delta T}{D}\,l}\right) \\ &= -\frac{\overline{V}_x^{Seebeck}\,D}{\Delta T\,l} + S_{Au} = S_{xx} \quad . \end{aligned} \tag{4.17}$$

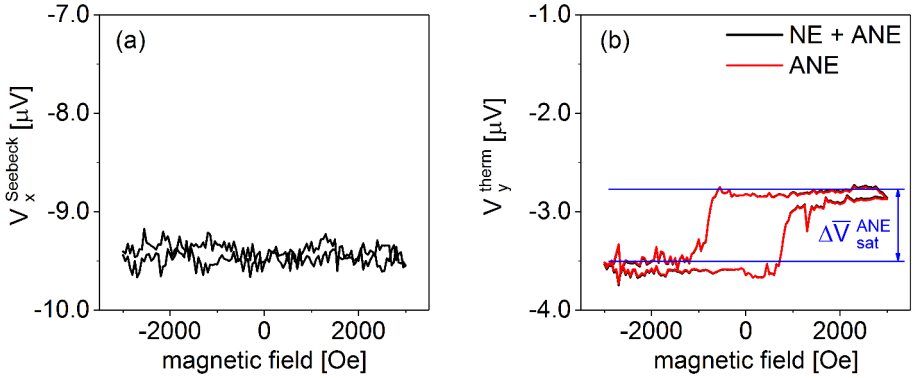

Figure 4.23.: Results of measurement mode 1: (a) Measuring $V_x^{Seebeck}$ depending on an external magnetic field lead to a constant voltage, (b) V_y^{therm} shows a clear hysteresis for $\Delta T = 30$ K.

Exemplary data of V_y for measurement mode 1 are shown in Fig. 4.23 (b). Note that the raw data principally show the superposition of the ONE and ANE (black curve) but can be separated with a linear correction of the saturation slope (red curve). In most measurements in this study, the ONE contributions are negligibly small. However, to extract the transverse thermopower coefficient S_{xy} the difference of the mean saturation voltages are taken and halved, $V^{ANE} = (\Delta\overline{V}_{sat}^{ANE})/2$, representing the effective ANE magnitude. Now, S_{xy} can be determined by the negative ratio of the voltage V^{ANE} induced by the temperature difference ΔT

$$S_{xy} = -\frac{V_y}{\Delta T} = -\frac{V^{ANE}}{\Delta T_{CB}} = -\frac{V^{ANE}\,D}{\Delta T\,l} \quad . \tag{4.18}$$

Figure 4.24 (a) illustrates an exemplary measurement of V_x^{AMR} during the measurement mode 2. For the determination of ρ_{xx} its mean value $\overline{V}_x^{AMR}$ is used since the relative change of resistivity due to the AMR is small,

$$\frac{V_{max}^{AMR} - V_{min}^{AMR}}{V_{min}^{AMR}} < 0.1\% \quad , \tag{4.19}$$

and the usage of $\overline{V}_x^{AMR}$ does not introduce a large error. The longitudinal resistivity ρ_{xx} is then calculated by

$$\rho_{xx} = \frac{\overline{V}_x^{AMR}}{I_x}\,\frac{w\,t_{tot}}{l} \quad . \tag{4.20}$$

The analysis of V_y^{elec} is conducted similar to V_y^{therm}, as described above. The effective AHE magnitude V^{AHE} leads to the anomalous Hall resistivity

$$\rho_{xy} = \frac{V^{AHE}}{I_x}\,t_{tot} \quad . \tag{4.21}$$

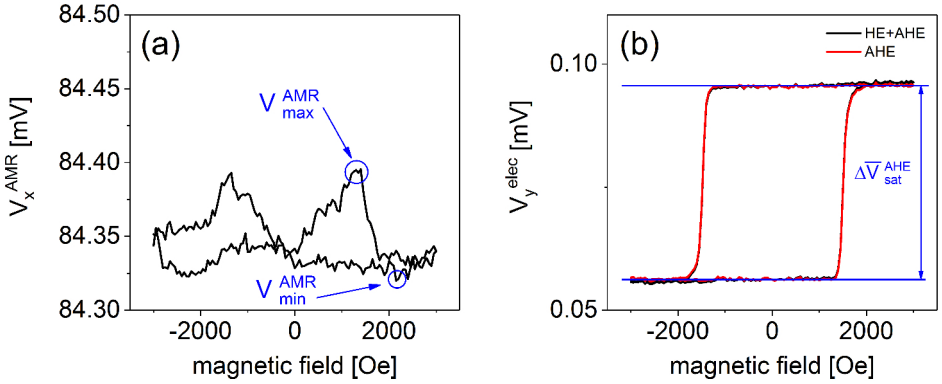

Figure 4.24.: Results of measurement mode 2: (a) Measuring V_x^{AMR} in dependence of the external field leads to two symmetrical peaks at about 1700 Oe. (b) Lock-In response while an alternating current is sent through the Hallbar. Again, the superimposed signal of the OHE and AHE can be separated by the subtraction of the linear slope of the saturation voltages.

The errors of all transport coefficients are calculated by linear error propagation following

$$\Delta f(x,y,z) = \left|\frac{\partial f(x,y,z)}{\partial x}\,\mathrm{d}x\right| + \left|\frac{\partial f(x,y,z)}{\partial y}\,\mathrm{d}y\right| + \left|\frac{\partial f(x,y,z)}{\partial z}\,\mathrm{d}z\right| \quad , \tag{4.22}$$

as derived in detail in the attachment. Measurement uncertainties of $\mathrm{d}D = 0.5\,\mathrm{mm}$, $\mathrm{d}\Delta T = 0.1\,\mathrm{K}$, $\mathrm{d}t_{\mathrm{tot}} = 2\,\mathrm{nm}$, $\mathrm{d}I_{\mathrm{x}} = 0.5\,\mu\mathrm{A}$, $\mathrm{d}l = \mathrm{d}w = +0\,\mathrm{mm}$ and $\mathrm{d}S_{\mathrm{Au}} = 0\,\frac{\mu\mathrm{V}}{\mathrm{K}}$ are assumed.

5. Results and Discussion

5.1. Rotation of a thermal gradient

In this section, the newly developed setup is used to conduct experiments with a rotatable thermal gradient. In contrast to other experiments, the sample is kept within the setup while rotating ∇T. Thus, neither the electrical contacts nor the thermal contacts to the heatsink or heatsource have to be changed for applying ∇T in different directions. After a proof of principle of the ∇T rotation by optical temperature detection, the ∇T rotation is used to investigate the anisotropy of magnetothermoelectric effects.

5.1.1. Optical experiments

The rotation of ∇T is proven for MgO, $MgAl_2O_4$ (MAO), Al_2O_3 (Sa) and Cu substrates to verify the rotation for materials in a broad range of thermal conductivities (15 $\frac{\mathrm{W}}{\mathrm{K\,m}}$ to 400$\frac{\mathrm{W}}{\mathrm{K\,m}}$). A temperature difference of $\Delta T = 20\,\mathrm{K}$ is applied at $T_{\mathrm{base}} = 35°\,\mathrm{C}$ at increasing $\varphi_{\mathrm{T}} = [0°, 360°]$ in steps of 15°. Figure 5.1 shows the IR records for the Cu substrate for applied $\varphi_{\mathrm{T}} = 45°, 105°, 240°, 360°$. The resulting directions of ∇T calculated within the ROI are indicated by the white arrows. They clearly show a successful rotation with calculated output angles of $\varphi_{\mathrm{T,\,out}} = 49°$, 112°, 246° and 352°. Thus, deviations between the input values and the optically calculated output angles of max. 8° can be observed. Similar to the Cu substrate, the rotation could be verified for the MgO, MAO and Sa substrates (see Figs. A.5, A.6, A.7 in attachment).

The recorded temperature distribution additionally allows the characterization of the temperature profile along the calculated output angle. The temperatures along the angle $\varphi_{\mathrm{T,\,out}}$ and within the ROI are exported and can be analyzed in more detail. This is done for all substrates at $\varphi_{\mathrm{T}} = 0°$ with a large ROI to also obtain information of the temperature of the sample holders. Figure 5.2 (a) illustrates the temperature profiles for the different substrates. The temperature profiles are linear for distances smaller than 4 mm from the center which proves a homogenous temperature distribution within all substrates. Only at the ends, where the sample holders are implied in the profile (|d|>4 mm), the temperature shows a nonlinear increase. In thermal equilibrium it is expected that the sample holders are at the same temperature as the sample in near proximity. This deviation can maybe explained by the transition of two different materials. Although the samples as well as the sample holders were coated by black Au to sustain equal

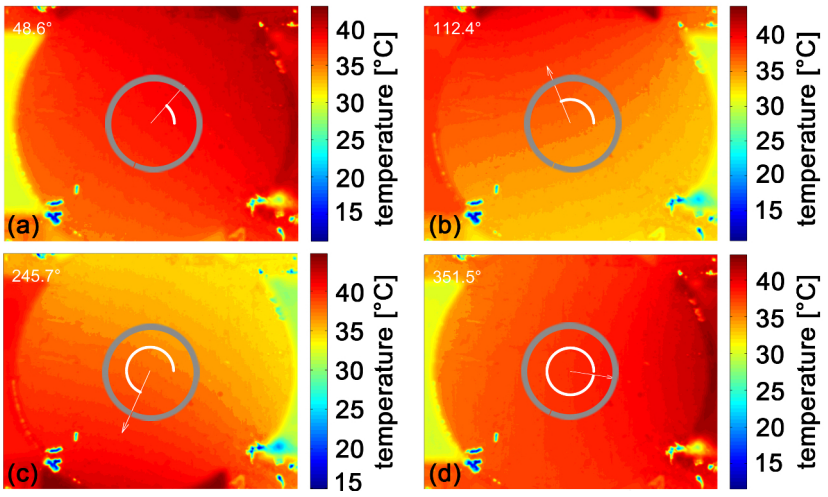

Figure 5.1.: The Cu substrate with applied ∇T at $\varphi_T = 45°$ (a), 105° (b), 240° (c) and 360° (d). The calculated output angles within the ROI prove the rotation of ∇T within ±8°.

emissivities, there might be a difference in the coating thickness resulting in a different amount of IR radiation despite the same temperature of sample and sample holder.

Since the new setup works under ambient conditions a qualitative comparison to vacuum conditions is made. For this purpose, the same samples are built into a vacuum furnace with a IR transmissive window for IR detection. Due to the dimensions of this setup, the IR detection only allows to record the sample and the heat bath, whereas the heat sink is situated out of the range of the IR camera. The temperature of the heat sink is therefore electrically detected by a thermocouple which is situated around 6 cm left from the sample's center. Although the distance between the thermocouple and sample could principally be subject to a thermal gradient, it consists of Cu with high thermal conductivity and, thus, is expected to equalize at the same temperature over the complete distance. Figure 5.2 (b) shows the vacuum temperature profiles for $\Delta T = 20\,\mathrm{K}$ and $T_{base} = 35\,\mathrm{K}$. Again, for small distances to the sample's center, the

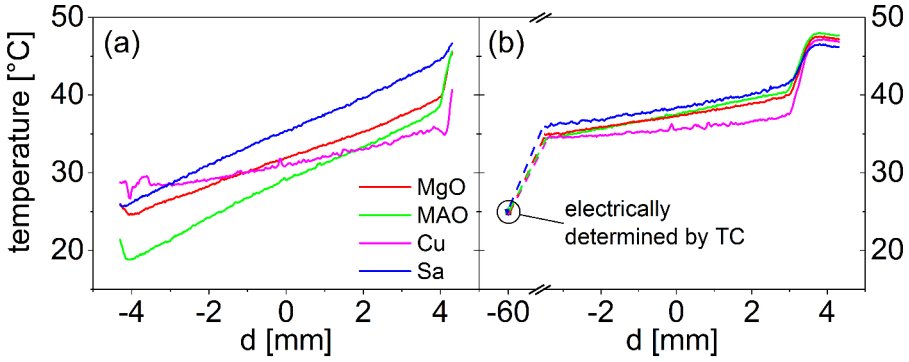

Figure 5.2.: Temperature profiles for different substrates under (a) ambient and (b) vacuum conditions. In both cases, a temperature difference of 20 K was applied at $T_{base} =$ 35° C.

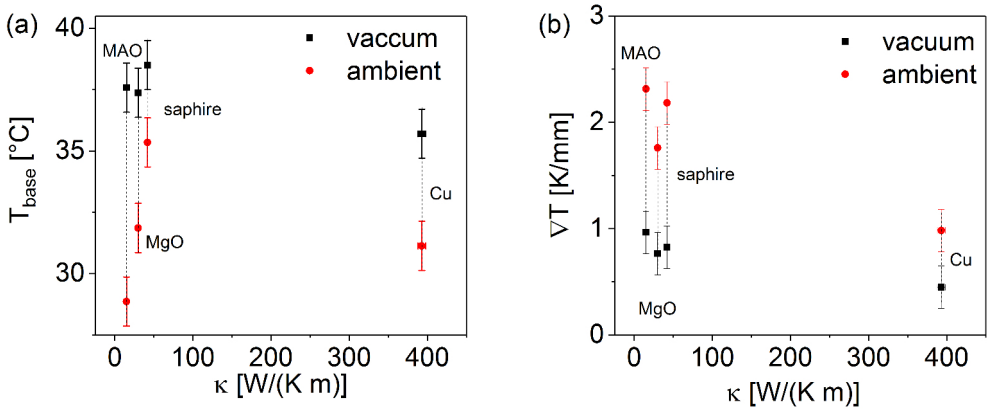

Figure 5.3.: A linear fit of the temperature profiles of Fig. 5.2 extracts T_{base} (a) and ∇T (b) for ambient and vacuum conditions.

temperature distribution is linear as expected for homogeneous samples. For d>3 mm, the heat bath is recorded which again shows a higher temperature than the sample. For this setup, it was not possible to coat the heat bath with the black Au which could be the reason for a higher temperature increase (≈ 8 K) in comparison to the setup in ambient conditions (≈ 5 K). However, the most noticeable difference to Fig. 5.2 (a) is the temperature difference between the heat sink and the sample. Because the heat sink's temperature is evaluated at a larger distance, it is connected by dashed lines to the sample's temperature. Here, the heat sink seems to be 10 K colder than the cold side of all samples. Since the thermocouple is connected via a solid Cu block to the sample and the complete Cu block is heated to 25°, a temperature drop of 10 K between the point of measurement and the sample does not seem reasonable. The temperature difference is rather attributed to the comparison of temperatures evaluated by two different methods. While the electric voltage generated by the Seebeck effect in the thermocouple is calibrated to the absolute temperature, the IR camera rather detects relative temperature changes within a sample with less absolute temperature values. Therefore, an absolute temperature comparison between different materials or different methods is not recommended, although the use of the black Au coating should minimize differences due to different sample properties.

Hence, for a further comparison of ambient and vacuum conditions we concentrate on the linear part of the temperature distribution within $|d| \leq 3$ mm. A linear fit of all temperature profiles gives the intercept and slope of the temperature distribution for each substrate. The intercept (x=0 mm) gives the temperature at the center of the sample, which should equal the applied base temperature of 35°C. Thus, the resulting T_{base} are plotted vs. the thermal conductivity κ in Fig. 5.3 (a). It can be seen that the profiles under ambient conditions principally show lower base temperatures than those under vacuum conditions. Thermal convection and conduction most likely additionally cool the samples, resulting in a net cooler temperature profile than in vacuum. It is expected, that for thermal equilibrium T_{base} should be independent of κ, leading to a constant T_{base} for all substrates. Under ambient conditions the calculated T_{base} are scattered within 7 K, but under vacuum conditions they are constant within 2 K. Only Cu is an exception

but with a deviation of 4 K it still lies within the measurement uncertainty. The slopes of the linear fits give the measured ∇T for all substrates. The comparison of ambient and vacuum conditions is shown in Fig. 5.3 (b). A general decrease of ∇T is obtained for increasing κ under ambient conditions while ∇T stays constant within the measurement uncertainties for vacuum conditions. Because for the IR measurements no thermal conductive paste is used, the microscopic roughness of the sample holder - sample interface highly influences the thermal resistance. Whereas in ambient conditions a thermal flux can also be transmitted via thermal conduction within microscopically embedded gas pockets, these gas pockets can not contribute to the thermal flux in vacuum conditions. This may result in higher thermal resistances between the sample and sample holder, leading to less efficient heating or cooling of the sample. This, in turn, would result in smaller thermal gradients, especially in materials with high thermal conductivities as it is the case for Cu.

Since the origin of the principally smaller ∇T in vaccum can not be identified for sure, a quantitative comparison between different materials or different surrounding conditions is hard to conclude. However, the optical data qualitatively show a successful rotation of ∇T for all substrates. This proof of principle allows to continue with a more quantitative study of the ∇T rotation.

5.1.2. Electrical experiments

After the optical determination of the rotation of ∇T, the rotation shall also be verified electrically. For this purpose, the longitudinal and transverse AMTP is investigated in a sputter deposited 18 nm thin $Ni_{80}Fe_{20}$ (Py) film ($5 \times 5\,mm^2$) on a MgO(001) substrate ($10 \times 10\,mm^2$). The smaller area of the Py film in comparison to the substrate allows its electrical decoupling to the sample holders when built into the setup as described earlier. Two gold wires were bonded in the center of the Py film, aligned to the y-axis and, thus, allow to measure V_y (see Fig. 4.2). All shown data of V_y are averaged over five single measurements at a base temperature of 308 K. The separation of the longitudinal and transverse AMTP is made possible by the use of two distinct measurement modes. A *sweep measurement* is conducted, when V_y is measured as a function of H, varied from -150 Oe up to +150 Oe (black branch of data) and back to -150 Oe (red branch of data). This mode depicts the magnetization dynamics of the AMTP or PNE under a fixed magnetic field angle φ. On the other hand, the *field rotation measurement* mode is used, when M is kept saturated along H ($H = 200\,Oe$, $\Delta\varphi = \pm 3°$) and follows the counterclockwise in-plane rotation of H. This mode rotates M and V_y reflects the φ dependencies of the AMTP or PNE, depending on φ_T, i.e. the applied direction of ∇T.

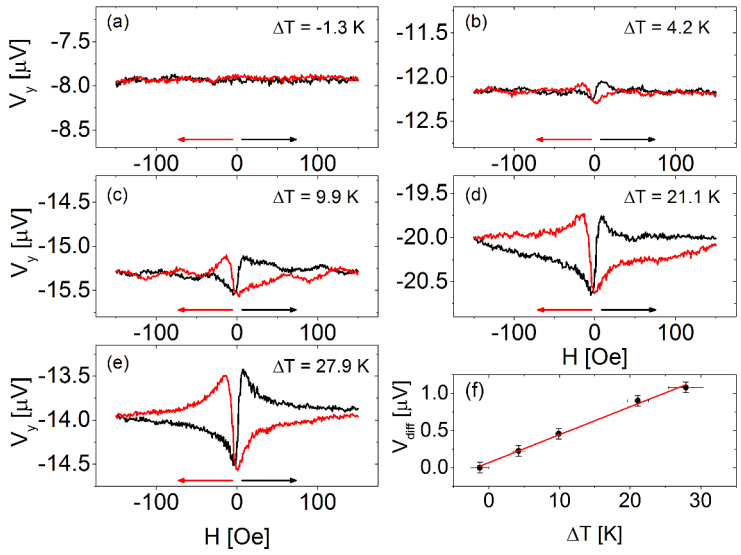

Figure 5.4.: (a)-(e) Sweep measurements of V_y for increasing ΔT and $\varphi = \varphi_T = 0°$. (f) The signal magnitude $V_{diff} = V_{max} - V_{min}$ is averaged for each branch and plotted vs. ΔT. The expected ΔT proportionality is verified.

∇T and φ dependence of the PNE

As shown in Sec. 4.1.5, within the given measurement geometry the electric field along the y-axis induced by the longitudinal AMTP is described by Eq. (4.12)

$$E_y = -(S_+ - S_- \cos 2\varphi)\,|\nabla T|\,\sin\varphi_T$$

and the contribution induced by the PNE by Eq. (4.13)

$$E_y = -S_-\,\sin 2\varphi\,|\nabla T|\,\cos\varphi_T \quad .$$

As a first step, sweep measurements for increasing ΔT are conducted for $\varphi = 0°$ and $\varphi_T = 0°$. Because ∇T is applied perpendicular to the voltage measurement, no AMTP contribution is present (Eq. (4.12)) and only the PNE is measured. Figure 5.4 shows V_y when ΔT is increased from $\approx 0\,K$ to $\approx 30\,K$. For the lowest ΔT, the sweep of H does not induce any change in V_y so that only a background signal within the noise level of $\approx 50\,nV$ can be detected (Fig. 5.4 (a)). Hence, the magnetization switching in the film due to the H reversal from -150 Oe to +150 Oe does not affect V_y. When ΔT is slightly increased to 4.2 K, V_y starts to develop peaks in the low magnetic field regime (Fig. 5.4 (b)). While increasing H from negative to positive values, V_y first stays constant before it forms a minimum for small negative fields. For small positive fields it abruptly changes to a maximum before it saturates again for high magnetic fields. Decreasing H from positive to negative fields leads to the same behavior, first showing a minimum for small positive fields followed by a maximum for small negative fields. Only then V_y decreases to the saturation value already obtained in the beginning of the raising branch. The shape of this signal

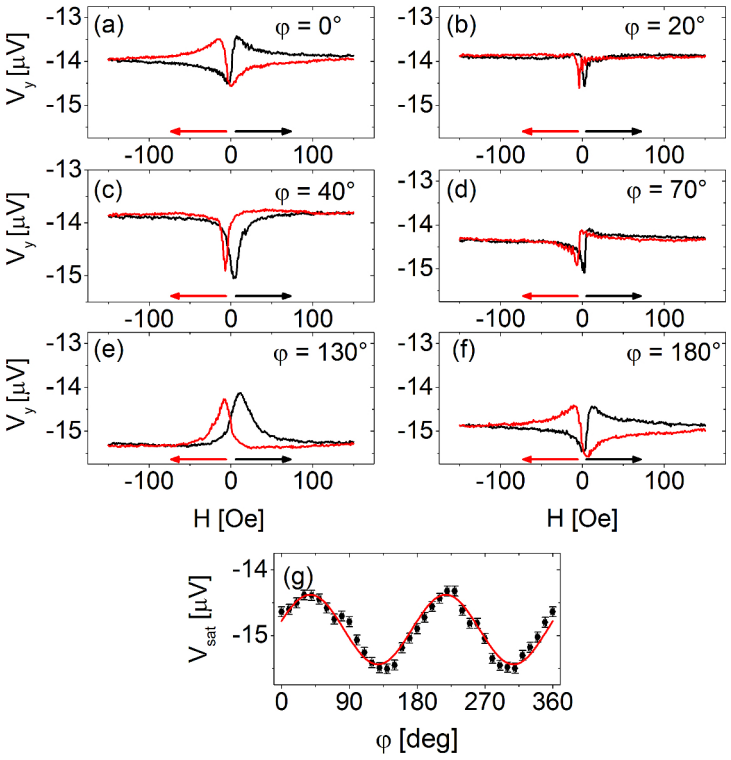

Figure 5.5.: (a)-(f) Magnetic sweep measurements are conducted for increasing field directions φ with an applied $\Delta T = 30\,\mathrm{K}$ at $\varphi_\mathrm{T} = 0°$. Only data for $0° \geq \varphi \geq 180°$ are shown, since these signals are repeated for higher angles due to the underlying $\sin 2\varphi$ symmetry. (g) The saturation values for $|H| \geq 140\,\mathrm{Oe}$ are averaged for each φ and plotted agains φ. The resulting data verify the $\sin 2\varphi$ dependence of the PNE, described by Eq. (4.13) (red fit).

is stressed, when ΔT is further increased up to $\approx 30\,\mathrm{K}$ and, thus, illustrates the influence of ΔT on $\mathrm{V_y}$. The voltage differences $\mathrm{V_{diff}}$ between the maximum and minimum of both branches are averaged for each ΔT and quantify the thermally induced magnitude increase. Figure 5.4 (f) shows that $\mathrm{V_{diff}}$ is proportional to ΔT following the $|\nabla T|$ dependence of the PNE described by Eq. (4.13). The study by Meier *et al.* also investigates the temperature dependence of the PNE on a Py thin film [68] which shows a similar behavior. Slight differences can be attributed to deviations of the magnetic anisotropy and small parasitic magnetic fields due to the interaction of both magnetic axes.

In the next step, sweep measurements are conducted for various magnetic field angles, $0° \geq \varphi \geq 360°$. Figure 5.5 shows exemplary chosen curves between 0° and 180°. Note that $\varphi_\mathrm{T} = 0°$ and $\Delta T = 30\,\mathrm{K}$ and, thus, Fig. 5.5 (a) shows the same dataset as Fig. 5.4 (e). Although for $|H| > 140\,\mathrm{Oe}$ all signals still show constant saturation values, the signal shape in the low magnetic field regime starts to qualitatively change for increasing field angles. For $\varphi = 20°$ (Fig. 5.5 (b)) both branches of the measurement show a minimum for small magnetic fields with small intensity. Hence, the magnetization switching process is independent of the field reversal

direction. When φ is increased to 40° (Fig. 5.5 (c)) the intensity of these minima reaches a maximum until for $\varphi = 70°$ they form a minimum and maximum with low intensity again (Fig. 5.5 (d)). Note that in contrast to $\varphi = 0°$ both branches show the minimum for negative and the maximum for positive magnetic fields and, like for $\varphi = 20°$, the magnetization reversal process is independent of the magnetic field switching direction. By further increasing φ to 130° each branch develops a maximum (Fig. 5.5 (e)) with comparable intensity. Here, both maxima are slightly shifted with respect to the origin, i.e. the black branch to positive and the red branch to negative fields. Reaching $\varphi = 180°$ (Fig. 5.5 (f)), V_y shows the same signal shape as for $\varphi = 0°$. For higher angles than $\varphi = 180°$ the curves from $0° \geq \varphi \geq 180°$ are repeated and are not shown for this reason.

Since the investigated film is a metal ferromagnet, an unintended oop thermal gradient in combination with the ip magnetization could give rise to a parasitic voltage contribution by the ANE. In a similar experiment Meier *et al.* systematically investigate the influence of an oop ∇T on the measured PNE signal by intentionally heating one contact needle [68]. Their experimental data of the same sweep measurements can be mathematically split into an antisymmetric and a symmetric part by taking the sum and the difference of the two branches. It shows that only the antisymmetric part is manipulated by the introduced oop ∇T and an antisymmetric contribution in the data of the sweep measurements is an indicator for underlying oop ∇T. Hence, the data shown in Fig. 5.5 (a)-(f) are analyzed in the same manner to evaluate any potential parasitic oop ∇T in the new setup. However, no systematic dependence of the asymmetric part on the field angle could be observed. Since this would have been the case for the ANE, any unintended oop contributions of the ∇T can be excluded for this setup. The small non-systematic asymmetric deviations in some of the shown data (e.g. Fig. 5.5 (c), (d)) can rather be attributed to a non-perfect antisymmetric magnetization reversal process for some magnetic field directions.

In general, when H is decreased to 0 Oe, M is not saturated and the total magnetization decays into statistically distributed magnetic domains depending on the underlying magnetic anisotropies. Depending on the orientations of those domains, the PNE induces an electric field in each domain following the angle dependence of Eq. (4.13). In contrast, when all magnetic domains are parallel aligned, also the resulting electric field induced by the PNE is aligned for each domain. Thus, one obtains a saturated voltage when M is saturated. Hence, the more the orientation of the magnetic domains deviate from the saturated state, the higher the resulting voltage deviates from the saturation voltage. This means, in turn, when for low magnetic fields only small or even no intensity change of the voltage can be measured, the magnetic domains do not change their initial orientation significantly, thus, are aligned to a magnetic easy axes (MEA). Therefore, the small intensities for both branches of the datasets for $\varphi = 20°, 70°$ indicate the presence of two MEA tilted by 50°.

This appearance can be explained by a non-parallel superposition of an uniaxial (UMA) and a fourfold in-plane cubic magnetic anisotropy (CMA). It has been shown that the presence of a UMA can be due to substrate shape [113], dangling bonds [114], surface steps [115] or oblique growth [116]. Furthermore, the UMA in Fe/MgO(001) systems was manipulated in terms of

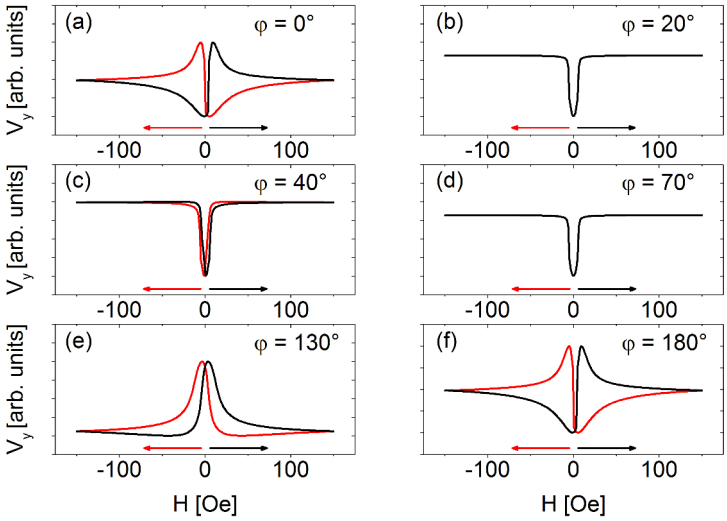

Figure 5.6.: The experimental data of Fig. 5.5 can be fitted by simulations based on the Stoner-Wohlfarth model. Besides of minimal deviations for the MEA ((b), (c)), all data can be qualitatively simulated.

orientation or strength by varying the deposition technique or deposition conditions [117, 118]. This has also been shown for Py films on different substrates [119, 120]. However, the presence of an UMA in our sample is very likely introduced via the deposition process. Because CMAs are expected to be present in cubic magnetic films due to the crystalline symmetry, the crystalline structure of the Py/MgO(001) sample is investigated via X-ray diffraction (XRD). As can be seen in the attachment, Fig. A.4 confirms a cubic structure by a fourfold diffraction pattern at a 2Θ angle of 44.332° for (111) Bragg reflections. Thus, a CMA can be expected and its superposition with the UMA can give rise to the MEAs at $\varphi = 20°$ and 70°. A more detailed insight in the underlying magnetization dynamics is given in the next section.

Figure 5.6 shows that the sweep measurements of Fig. 5.5 can be simulated via the Stoner-Wohlfarth model regarding the geometry of the electromagnets (see next section). While the simulations for both MEA (Fig. 5.6 (b), (d)) equals each other, the experimental data show a different signal shape and, thus, propose a varying magnetization reversal process for both MEA. Additionally, both branches of the simulated MEA are identical whereas those of the experimental data show a slight shift of around 20 Oe. This shift is also observable for the other angles but despite of this fact, the simulations fit the experimental data exceptionally well.

So far, only the shape of the field reversal curves of V_y are discussed. As it is explained in detail later, they can be used to conclude the magnetization reversal process. Now, the φ dependence of the saturation values V_{sat} shall be highlighted. When all V_y for $|H| \geq 140\,\mathrm{Oe}$ are averaged, subtracted by a linear temperature drift and plotted vs. the magnetic field angle, V_{sat} shows an oscillation around an offset value of -15 μV (Fig. 5.5 (g)). This offset value results from the ordinary Seebeck coefficient described by S_+ in Eq. (4.12). The data follow a $\sin 2\varphi$ dependence and, therefore, confirm the φ dependence for the PNE predicted by Eq. (4.13). The PNE

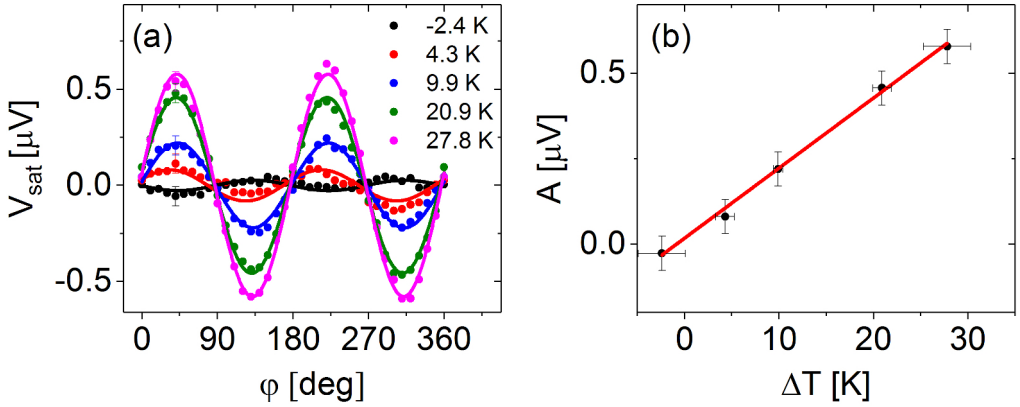

Figure 5.7.: Rotation measurements for increasing ΔT are conducted with $\varphi_T = 0°$. For reasons of better overview, the measurement uncertainties $\delta\varphi$ and δV_{sat} are only shown for $\varphi = 40°$. Each data set confirms the $\sin 2\varphi$ oscillation of Fig. 5.5 (g) and, thus, can be fitted with $V_{sat} = y_0 + A \sin 2(\varphi - \varphi_0)$. (b) The fit parameter A indicates the PNE magnitude and is proportional to ΔT. Thus, the experimental data follow the φ and ΔT dependence of Eq. (4.13).

amplitude is determined to $(0.5 \pm 0.05)\,\mu V$ which proves the setups resolution within the nanovolt regime. Small deviations between the fit and data can be found around $\varphi = 90°$, 270° but an analysis of $V_{sat} - V_{\sin 2\varphi}$ observes no systematical measurement artefacts. These data are basically obtained from a rotation measurement and confirm the presence of the PNE. To further prove the setups functionality, rotation measurements for five different ΔT are conducted.

For this purpose, five rotation measurements for each ΔT are averaged and depicted in Fig. 5.7 (a). Following Eq. (4.13), all data sets can be fitted with $V_{sat} = y_0 + A \sin 2(\varphi - \varphi_0)$ with a fixed phase shift φ_0 for all data sets. An increasing oscillation amplitude for increasing ΔT is clearly observed. The fit parameter A represents the strength of the PNE which is dependent on ΔT. Plotting A vs. ΔT (Fig. 5.7 (b)) illustrates the ΔT proportionality of the PNE magnitude and unambiguously proves the presence of the PNE. Thus, the data confirm the derived theory for the PNE.

Influence of ∇T rotation on AMTP and PNE measurements

In the next step, the key feature of the new setup is investigated. Therefore, $\Delta T = 30\,K$ is rotated within the sample plane from 0° to 360° in steps of $d\varphi_T = 15°$. For each φ_T a sweep measurement at $\varphi = 0°$ is recorded. Figure 5.8 (a)-(f) shows exemplary data, each with an inset which symbolizes the geometric orientation of ∇T (red to blue color gradient). As before, each sweep measurement shows a saturation voltage in the high magnetic field regime and the formation of extrema in the low magnetic field regime near the zero crossing point.

Since for (a) $\varphi_T = \varphi = 0°$, this measurement equals the data of Fig. 5.5 (a). Due to the perpendicular voltage measurement with respect to ∇T, V_y records a transverse signal. Any

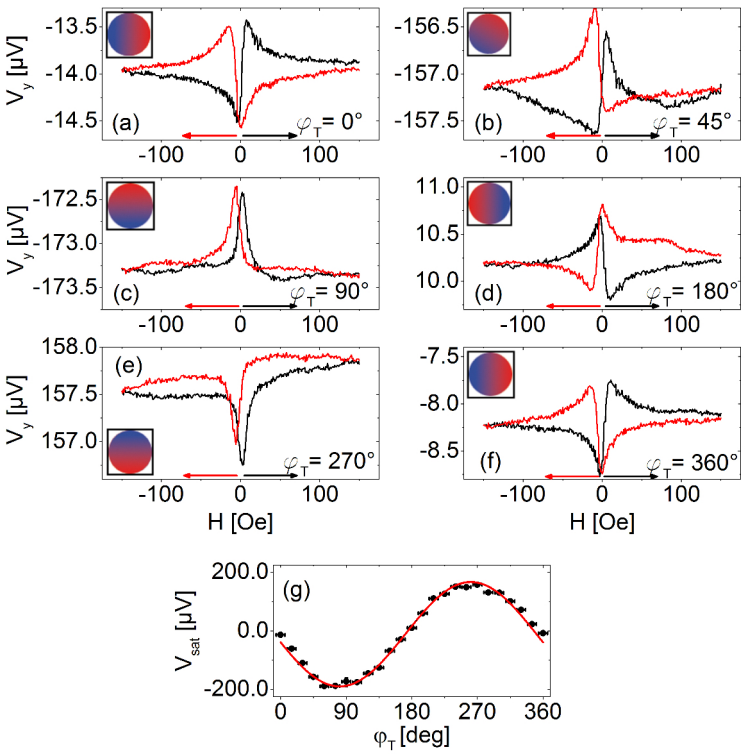

Figure 5.8.: (a)-(f) Magnetic sweep measurements at $\varphi = 0°$ for increasing φ_T. (g) The voltages V_{sat} are calculated as described for Fig. 5.5 (g) and plotted vs. φ_T.

contributions of the AMTP can be generally excluded since $E_{y,AMTP} \propto \sin 2\varphi_T$ (see Eq. (4.12) for $\varphi_T = 0°$). On the other hand, when M is saturated along $\varphi = 0°$ for high magnetic fields, the PNE contribution also vanishes due to $E_{y,PNE} \propto \sin 2\varphi \cos \varphi_T$ (see Eq. (4.13)). Only for low magnetic fields V_y resolves the PNE responses of differently aligned magnetic domains than for $\varphi = 0°$.

Figure 5.8 (c) depicts the situation for $\varphi_T = 90°$. In contrast to (a), ∇T is parallel to the voltage measurement and $E_{y,PNE} \propto \sin 2\varphi \cos \varphi_T$ results in a total exclusion of any PNE contribution to V_y. Thus, the signal originates purely from the AMTP, described by the proportionality $E_{y,AMTP} \propto \sin 2\varphi_T$ in Eq. (4.12). Here, both extrema of each branch in (a) have developed to one common maximum near 0 Oe. This transformation is already observable in (b) ($\varphi_T = 45°$), where both minima are clearly decreased in comparison to (a). Note that here V_y is a superimposed signal of the PNE and AMTP since the total thermal gradient is composed of an x- and y-thermal gradient. Thus, $\nabla_x T$ induces a contribution to E_y due to the PNE and $\nabla_y T$ an E_y contribution due to the AMTP. Increasing φ_T changes the relative orientation of M with respect to ∇T, leading to a subsequent shift from a PNE to an AMTP measurement and back.

Consequently, (d) shows a horizontally mirrored PNE signal for $\varphi_T = 180°$ in comparison to (a), whereas (e) with $\varphi_T = 270°$ is the mirrored counterpart to $\varphi_T = 90°$. Only after a complete rotation by 360° the signal of (a) is repeated, see (f). Note that also for rotating φ_T, each sweep measurement can be simulated with the same model as previously described for rotating φ.

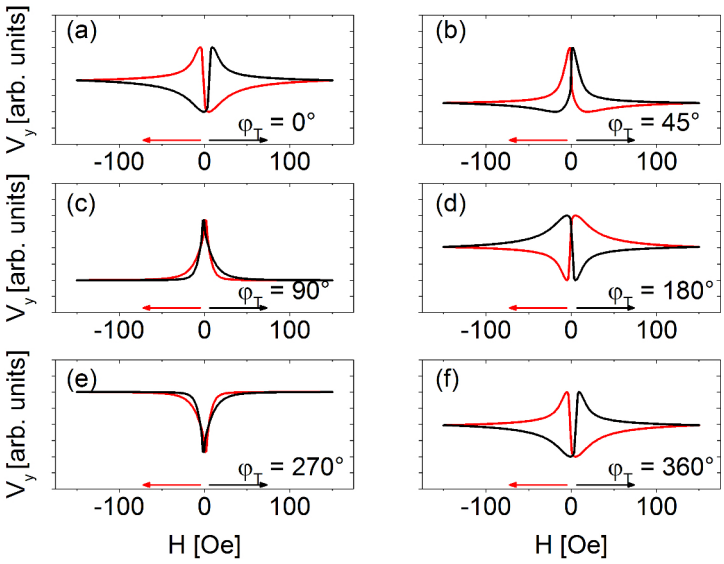

Figure 5.9.: Simulated sweep measurements of Fig. 5.8 by MuMax3.

Figure 5.9 shows the convincing agreement between the experimental data and the underlying model for all directions of the applied ∇T.

The superposition of the PNE and AMTP can be described by adding Eq. (4.13) and Eq. (4.12) to the total electric field along the y axis, leading to

$$E_\mathrm{y} = -S_+ \left|\nabla T\right| \sin\varphi_\mathrm{T} - S_- \left|\nabla T\right| \cos\varphi_\mathrm{T} \sin 2\varphi + S_- \left|\nabla T\right| \sin\varphi_\mathrm{T} \cos 2\varphi \quad . \tag{5.1}$$

Equation (5.1) describes the measured voltage, when the distance of the voltage probes d is taken into account

$$V_\mathrm{y} = y_0(\varphi_\mathrm{T}) + A(\varphi_\mathrm{T}) \sin 2\varphi + B(\varphi_\mathrm{T}) \cos 2\varphi \quad , \tag{5.2}$$

with

$$y_0(\varphi_\mathrm{T}) = -S_+ \left|\nabla T\right| d \sin\varphi_\mathrm{T} \quad , \tag{5.3}$$

$$A(\varphi_\mathrm{T}) = -S_- \left|\nabla T\right| d \cos\varphi_\mathrm{T} \quad , \tag{5.4}$$

$$B(\varphi_\mathrm{T}) = S_- \left|\nabla T\right| d \sin\varphi_\mathrm{T} \quad . \tag{5.5}$$

Here, $y_0(\varphi_\mathrm{T})$ describes the magnetic field independent ordinary Seebeck effect, whereas the parameters $A(\varphi_\mathrm{T})$ and $B(\varphi_\mathrm{T})$ represent the magnitudes of the PNE and AMTP, respectively. Figure 5.8 (g) depicts all saturation voltages of (a)-(f) implying that the magnetization is always saturated along $\varphi = 0°$. Hence, the PNE contribution in Eq. (5.2) cancels out, leaving only $y_0(\varphi_\mathrm{T})$ and $B(\varphi_\mathrm{T})$ (i.e. the Seebeck effect and the AMTP) contributing to V_y. Comparing Eqs. (5.4) and (5.5) reveal that the AMTP is expected to be of identical magnitude as the PNE which was earlier determined to $0.5\,\mu$V. Thus, the obtained sine oscillation of $(178 \pm 4)\,\mu$V is three

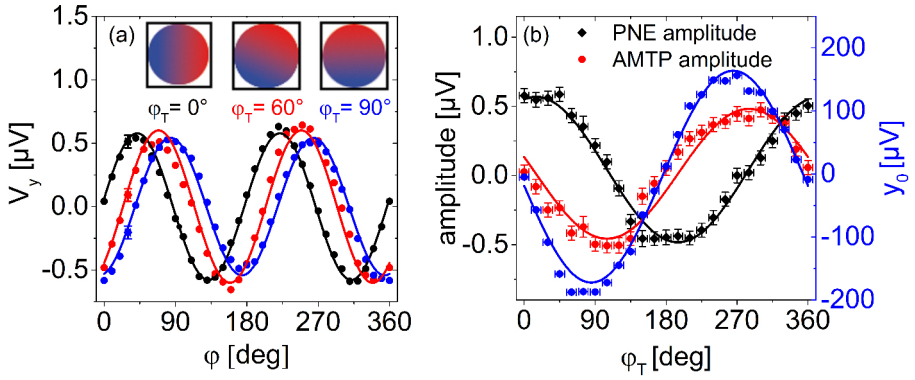

Figure 5.10.: The angle φ_T is increased from 0° to 360° after recording a rotation measurement at each φ_T. (a) The rotation of ∇T results in a phase shift of the sin(2φ) ($\varphi_T = 0°$) to a -cos(2φ) oscillation ($\varphi_T = 90°$) and a changing voltage offset consistent with Eq. (4.14). The measurement uncertainties are depicted only at $\varphi = 30°$ for reasons of better overview. All rotation measurements are fitted with Eq. (5.2) and the resulting fit parameters y_0 (blue), A (black) and B (red) are plotted against φ_T in (b). They follow the expected cos- (PNE), sin- (AMTP) and sin- (ordinary Seebeck effect) dependence on φ_T described by Eqs. (5.3)-(5.5).

orders of magnitude larger than the AMTP or PNE and, therefore, can be attributed only to the sin (φ_T) dependence of the ordinary Seebeck effect. The sine oscillation of the Seebeck effect can also be explained geometrically. Rotating ∇T within the sample plane leads to a sin(φ_T) projection of ∇T onto the y-axis. This projection results in the sine shaped Seebeck voltage V_y.

So far, only one parameter was constantly changed within a measurement series. Either the angle of H or the angle of ∇T. Now, a combination of both is used to separate and compare all three contributions to V_y. Firstly, rotation measurements are conducted for $0° > \varphi_T > 360°$, subtracted by the offset voltage y_0 for better overview and plotted in Fig. 5.10 (a). The sin (2φ) oscillation already observed in Fig. 5.5 (g) is repeated for $\varphi_T = 0°$ and represents a pure PNE measurement due to the transverse measurement of V_y relative to ∇T. The oscillation shifts for higher φ_T (exemplary represented by the red curve for $\varphi_T = 60°$) until it equals a $-\cos(2\varphi)$ oscillation for $\varphi_T = 90°$. In the latter case, due to the parallel measurement of V_y relative to ∇T, the AMTP is the origin of the observed signal. As previously described, all measurements for $\varphi_T \neq 0°, 90°, 180°, 360°$ consist of a superposition of all effects due to the subsequent change of the ∇T projection onto the x- and y- axis. The observed phase shift of the rotation measurements for increasing φ_T is consistent with Eq. (4.14) and stresses the subsequent shift of a PNE to an AMTP measurement. Secondly, the rotation measurements are fitted with Eq. (5.2), since this relation regards the separate contributions of the Seebeck effect, PNE and AMTP for each φ and φ_T. As can be seen in Fig. 5.10 (a), all rotation measurements can be fairly fitted by this formulation.

Now, the resulting fit parameters $y_0(\varphi_T)$, $A(\varphi_T)$ and $B(\varphi_T)$ are plotted vs. φ_T in Fig. 5.10 (b). The result clearly illustrates the φ_T dependencies of all parameters as predicted by Eqs. (5.3)-(5.5) and even reflects the opposite sign of A and B. Since this plot depicts the contribution of each effect to V_y for different φ_T, it also verifies the previously mentioned shift from a PNE to an AMTP measurement. At $\varphi_T = 0°$, $B(\varphi_T)$ and $y_0(\varphi_T)$ (AMTP and ordinary Seebeck effect) vanish while $A(\varphi_T)$ (PNE) is at its maximum. In contrast, at $\varphi_T = 90°$, $A(\varphi_T)$ vanishes while $B(\varphi_T)$ and $y_0(\varphi_T)$ are maximal.

Consequently, the fit parameters are fitted with the corresponding Eqs. (5.3)-(5.5), revealing a PNE amplitude of $(0.53 \pm 0.05)\,\mu$V and an AMTP amplitude of $(-0.47 \pm 0.05)\,\mu$V. As it was expected, both effect magnitudes are the same within the measurement uncertainty. Thus, they can be averaged to estimate the thermovoltage induced by S_-

$$S_- |\nabla T|\, d = -(0.50 \pm 0.05)\,\mu\text{V} \quad . \tag{5.6}$$

On the other hand, the fit of y_0 describes the S_+ induced Seebeck effect by

$$U_{\text{Seebeck}} = -S_+ |\nabla T|\, d = -(168 \pm 4)\,\mu\text{V} \quad . \tag{5.7}$$

At this point it is important to note, that the measured Seebeck contribution is again a superpositioned signal. Not only the measured Py film under investigation influences the resulting signal, but also the used Au bond wires to contact the thin film. Because of the absence of ferromagnetism, their influence can be neglected for the PNE and AMTP. But the magnetic field independent Seebeck effect of the wires influences the measured Seebeck voltage. Thus, the Seebeck coefficient S_+ has to be regarded as an effective Seebeck coefficient composed of the Seebeck coefficients of the film and wires. The conventional definition of the Seebeck voltage in combination with $S_{\text{Py}} = -4.5\,\frac{\mu\text{V}}{\text{K}}$ [100] and $S_{\text{Au}} = 1.8\,\frac{\mu\text{V}}{\text{K}}$ [101], allows to estimate the net applied temperature difference between the bond wires

$$\begin{aligned} U_{\text{Seebeck}} &= -S_{\text{eff}}\,\Delta T = -(S_{\text{Py}} - S_{\text{Au}})\,\Delta T = -(168 \pm 4)\,\mu\text{V} \\ \Delta T &= \frac{U_{\text{Seebeck}}}{-S_{\text{eff}}} = -(26.7 \pm 0.6)\,\text{K} \quad . \end{aligned} \tag{5.8}$$

This result agrees well with the applied temperature difference of 30 K between the sample holders and can further be used to calculate S_- by Eq. (5.6)

$$\begin{aligned} U_- &= -S_-\,\Delta T = (0.50 \pm 0.05)\,\mu\text{V} \\ S_- &= -\frac{U_-}{\Delta T} = (0.019 \pm 0.002)\,\frac{\mu\text{V}}{\text{K}} \quad . \end{aligned} \tag{5.9}$$

With the earlier introduced definitions

$$S_+ = \frac{S_{||} + S_-}{2} \quad \text{and} \quad S_- = \frac{S_{||} - S_\perp}{2}$$

the Seebeck coefficients parallel and perpendicular to the magnetization can be formulated

$$S_{||} = S_+ + S_- \quad \text{and} \quad S_\perp = S_+ - S_- \quad . \tag{5.10}$$

Now, the relative change of the anisotropic Seebeck coefficient, ΔS, can be expressed in terms of S_- and S_+

$$\Delta S = \frac{S_{||} - S_\perp}{S_{||}} = \frac{2\,S_-}{S_+ + S_-} \quad . \tag{5.11}$$

Finally, since ΔS should only be determined for the Py thin film, instead of the experimentally observed S_+, S_{Py} is used to derive

$$\Delta S = \frac{2\,S_-}{S_{\mathrm{Py}} + S_-} = -(0.84 \pm 0.08)\% \quad . \tag{5.12}$$

This result shows, that in the investigated thin film the magnetothermopower is 0.84% stronger perpendicular to its magnetization than parallel to it.

5.1.3. Simulation of electrical experiments

In kind cooperation with A. Shestakov from Regensburg University simulations have been conducted to fully understand the voltage traces shown in Figs. 5.5 and 5.8. Subsequent calculations based on the Stoner-Wohlfarth model including the superposition of a UMA and CMA as well as parasitic magnetic field contributions by the setups geometry lead to the simulated voltage traces shown in Figs. 5.6 and 5.9.

As mentioned earlier, Eqs. (3.36) and (3.38) imply that the vector of the magnetization $\vec{M}$ coincides with the vector of the external field $\vec{H}$, $\varphi_M = \varphi$. This assumption is only valid as long as $\vec{H}$ is at least one order of magnitude larger than any underlying magnetic anisotropy i, $|\vec{H}| \gg \frac{C_i\,K_i}{M_s}$ (C_i dimensionless constant, K_i anisotropy constant, M_s saturation magnetization), or any parasitic magnetic field contributions $\vec{H}_p$, $\left(|\vec{H}| \gg |\vec{H}_p|\right)$. However, this is only the case for fields larger than 100 Oe and a more specified model is needed in order to calculate φ_M for lower H and to simulate the complete voltage traces of the sweep measurements.

For this purpose, Eq. (4.14) is rearranged, describing only the magnetic field dependent change of V_{y}

$$V_{\mathrm{y}}(H) = S_-\,d\,|\nabla T|\sin\left(2\,\varphi_{\mathrm{M}}(H) - \varphi_{\mathrm{T}}\right) \quad . \tag{5.13}$$

Here, the contact distance d is included since $V_{\mathrm{y}} = -E_{\mathrm{y}}\,d$ and the summand S_+ is neglected because it only causes a voltage offset and is not dependent on H. The presence of two MEA at $\varphi = 20°, 70°$ was earlier explained by the superposition of an UMA and a CMA and are also taken into account for further calculations.

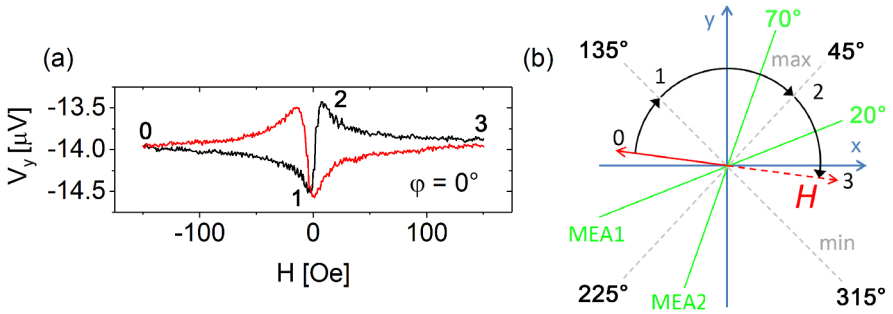

Figure 5.11.: (a) Each branch of the experimental sweep measurement passes through 4 specified positions, (b) M reversal explanation for the sweep measurent at $\varphi = \varphi_T = 0°$. The green lines indicate magnetic easy axes whereas the gray dashed lines indicate the directions for minimal and maximal voltage responses, following Eq. (5.13).

Figure 5.11 (a) shows the experimental sweep measurement at $\varphi = \varphi_T = 0°$. The black branch represents the sweep up curve and the red branch the sweep down measurement. At position 0, M is saturated at negative H, representing the start of the measurement where $\varphi_M = \varphi \approx 180°$. Next, the voltage passes its minimum for low negative H near 0 Oe at position 1, before it directly increases to its maximum at position 2 for low positive H. At 1 and 2 the magnetization vector tilts out of the direction φ since the magnetic field is too weak to keep M aligned. Only then it saturates again at position 3 for high positive fields, where the magnetization angle equals the field angle, $\varphi_M = \varphi = 0°$.

A first suggestion for the rotation of M is depicted in Fig. 5.11 (b). The green lines indicate the directions of both MEA along 20° and 70°. Additionally, according to Eq. (5.13), the maximum of the voltage occurs for $\varphi_M = 45°$, 225° and the minimum for $\varphi_M = 135°$, 315° and, thus, these axes are highlighted by the dashed gray lines. The rotation of φ_M is illustrated by the black arrows. At point 0, H is at high negative fields (solid red arrow) and keeps M aligned. When the absolute magnitude of H is reduced, M rotates off the direction of H towards the minimum at point 1, despite it is expected to first move to the closer MEA1. After switching the direction of H (along dashed red line), M first passes MEA2, reaches the maximum at point 2 and finally aligns with H at point 3 for high positive fields.

In the next step, the in-plane magnetic free energy density, U, is calculated. Following Gurevich *et al.* [121], it reads in the presence of a UMA and CMA for monodomain magnetization

$$U = -M_s\, H\, \cos\left(\varphi_M - \varphi\right) + K_U \sin^2(\varphi_M - \varphi_{UA}) + \frac{K_C}{4} \sin^2(2[\varphi_M - \varphi_{CA}]) \quad . \tag{5.14}$$

Here, the first, second and third terms are attributed to the Zeeman, the UMA and the CMA energies, respectively. K_U (K_C) expresses the strength and φ_{UA} (φ_{CA}) the angle of the UMA (CMA). As before, M_s is the saturation magnetization and φ_M the direction of the magnetization. In the given geometry, the demagnetization energy is excluded since the estimated demagnetization factors following Aharoni *et al.* [122] are in the order of 10^{-6} and lead to negligible effective in-plane demagnetizing fields of around 0.01 Oe. With literature values for Py ($K_C = 5 \cdot 10^4 \frac{\text{erg}}{\text{cm}^3}$

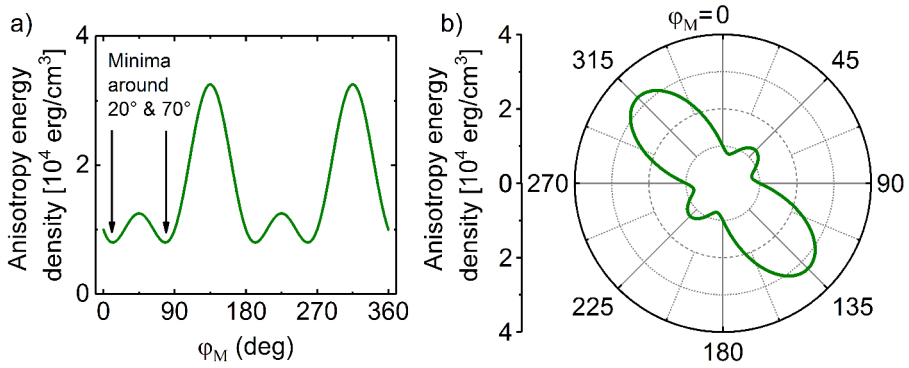

Figure 5.12.: (a) Magnetic free energy density U in dependence of the magnetization angle φ_M calculated by Eq. (5.14). The energy minima are aligned with the MEA at 20° and 70° and, thus, determine the appearance of MEA at the given angles. (b) The energy distribution plotted in polar coordinate system.

[123], $K_U = 2 \cdot 10^4 \frac{\text{erg}}{\text{cm}^3}$ [70, 124]) as well as $\varphi_{UA} = 45°$ and $\varphi_{CA} = 0°$ and without an external magnetic field, the angular distribution of U can be calculated. It is shown in Fig. 5.12 and clearly verifies the experimentally found energy minima at $\varphi = 20°, 70°$. With this model, however, only symmetric PNE/AMTP traces can be simulated and do not reasonably fit the experimental signal shown in Fig. 5.11 (a).

Therefore, in the next step, the simulations were improved by using a more sophisticated model. MuMax3 regards the magnetic hysteresis, uses magnetic multidomain states and includes UMA and CMA as well as finite temperature modeling [125]. Due to the cell number limitation of this model, the effective Py area has to be reduced to $1 \times 1\,\mu\text{m}^2$ which leads to an enhanced demagnetization energy contribution by 3 orders of magnitude. As a consequence, M_s is halved and the anisotropy constants are enlarged by an order of magnitude in comparison to the aforementioned simulations. In addition with the expansion of the field sweep range to $\pm 1000\,\text{Oe}$, this model only gives qualitative simulations. However, the result can be seen in Fig. 5.13. A clear asymmetric trace of V_y can be seen in (a) with a maximum for small negative fields and a minimum for small positive fields. The corresponding rotation of M is depicted in Fig. 5.13 (b). In contrast to Fig. 5.11, M tilts from the fully saturated negative direction at point 0 towards the MEA 1 at point 1 for low negative fields. By further increasing H, M switches its direction by 180° via multidomain state into point 2. Note for $H = 0\,\text{Oe}$ (point 1') M first passes through the maximum direction at 225° before the absolute value of M reduces to a minimum due to the multidomain state. Because the AMTP (PNE) is proportional to $|M|^2$, the voltage trace shows a minimum for low positive fields where $|M|$ is minimal. For higher H, M saturates and aligns with H at point 3. Although this model leads to asymmetric voltage traces which are also seen in other AMTP (PNE) experiments with CMA, low M_s and large magnetic anisotropy [126, 127], the results of this study can not reasonably be fitted.

The last deviations between the simulations and experimental results can be eliminated by introducing a parasitic magnetic field H_p which is induced by the geometry of the setup itself.

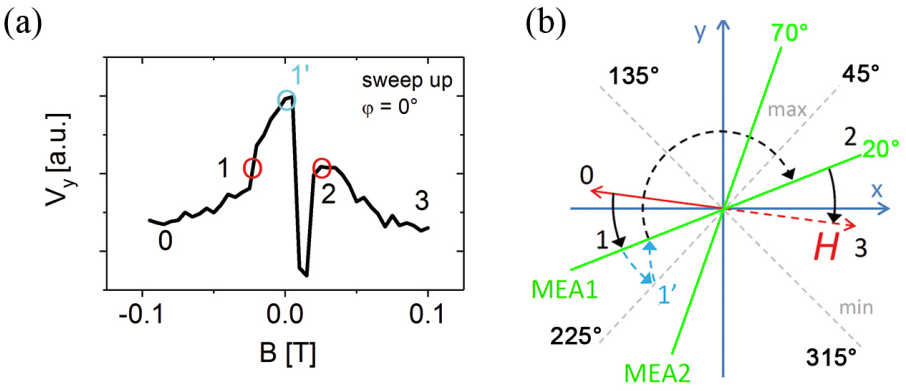

Figure 5.13.: (a) The normalized sweep up trace simulated by MuMax3 and (b) the corresponding rotation of M involving multidomain switching.

Since the magnetic hard axes of the CMA are aligned with the magnetic poles of the magnet, a link between both seems reasonable. For the case of a perfect geometry of the magnet, including the pole distances and homogeneity of the yoke, a pure CMA due to the samples symmetry proven by the XRD seems realistic. But for small perturbations within the geometry, the introduction of an additional UMA could be realized. For example, in case of a smaller distance between one magnet pair compared to the other, the magnetic flux could prefer one axis and thus introduce another UMA. Additionally, through the direct connection of both axis via the yoke, a leakage of magnetic flux from one pair to the other might appear. Therefore, the magnetic state of one axis is dependent on the other and, thus, introduces the parasitic field $H_\mathrm{p}(\varphi)$ which can be written as

$$|H_\mathrm{p}(\varphi)| = |H_{\mathrm{p,\,max}}|\,|\sin(\varphi - \varphi_{\mathrm{min1}})\sin(\varphi - \varphi_{\mathrm{min2}})| \quad . \tag{5.15}$$

The amplitude $H_{\mathrm{p,\,max}}$ is set to 7.5 Oe, $\varphi_{\mathrm{min1}} = 20°$ and $\varphi_{\mathrm{min2}} = 70°$, leading to Fig. 5.14 (a) which is very similar to the free energy density U, Fig. 5.12. It basically shows the anisotropy of the amplitude of the parasitic field.

Furthermore, it has to be taken into account, that the direction of $H_p(\varphi)$, φ_p, is dependent on H and φ,

$$\varphi_\mathrm{p}(H,\varphi) = \varphi \pm 180° \left(\frac{H_\mathrm{max} + H}{2\,H_\mathrm{max}}\right) \quad . \tag{5.16}$$

Here, $H_\mathrm{max} = 150$ Oe and the phase shift is attributed to the leakage process and the rotation of M. The sign is chosen the way, that M rotates into the closest minimum of the AMTP (PNE) signal, corresponding to Fig. 5.11 (b).

The combination of the aforementioned methods allows the complete reconstruction of the experimental voltage signals. Firstly, for fixed $H_{\mathrm{p,\,max}}$, φ_T, φ_{min1}, φ_{min2}, $|H_\mathrm{p}(\varphi)|$ is calculated (Eq. (5.15)) followed by the numerical solution of Eq. (5.16) which gives the orientation of $\vec{H}_\mathrm{p}$

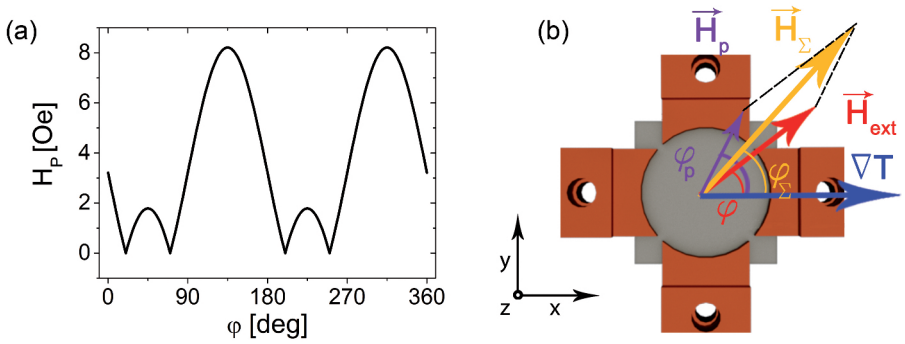

Figure 5.14.: (a) The parasitic field H_p introduced by a non-perfect geometry of the magnet, according to Eq. (5.15). (b) Via vectorsum the parasitic magnetic field $\vec{H}_\mathrm{p}$ adds up with the externally applied $\vec{H}$ to the effective field $\vec{H}_\Sigma$ which determines the Zeemann contribution to the magnetic free energy U.

for each value H of a sweep measurement. Secondly, the effective magnetic field $\vec{H}_\Sigma(H)$ along the orientation $\varphi_\Sigma(H)$ is introduced, where both parameters are determined by vector addition of $\vec{H}$ and $\vec{H}_\mathrm{p}$ (see Fig. 5.14 (b)). Now, the Zeemann energy contribution to U in Eq. (5.14) is corrected by $H_\Sigma(\vec{H})$ and $\varphi_\Sigma(\vec{H})$ resulting in

$$\begin{aligned} U = &- M_\mathrm{s}\, H_\Sigma(\vec{H})\, \cos\left(\varphi_\mathrm{M} - \varphi_\Sigma(\vec{H})\right) + K_\mathrm{U} \sin^2(\varphi_\mathrm{M} - \varphi_\mathrm{UA}) \\ &+ \frac{K_\mathrm{C}}{4} \sin^2(2[\varphi_\mathrm{M} - \varphi_\mathrm{CA}]) \quad . \end{aligned} \tag{5.17}$$

The equilibrium position φ_M of $\vec{M}$ for the complete field sweep can now be calculated by finding φ_M for which U is minimal. Thus,

$$\frac{\partial U}{\partial \varphi_\mathrm{M}} = 0 \tag{5.18}$$

numerically calculates the $\varphi_\mathrm{M}(H)$ dependence. By inserting $\varphi_\mathrm{M}(H)$ into Eq. (5.13) the normalized ($S_- \left|\nabla T\right| d = 1$) voltage curve $V_\mathrm{y}(\varphi_\Sigma(H))$ reconstructs the experimental data reasonably well. By repeating this procedure for each φ and φ_T the sweep measurements of Figs. 5.5 and 5.8 can be simulated, resulting in Figs. 5.6 and 5.9.

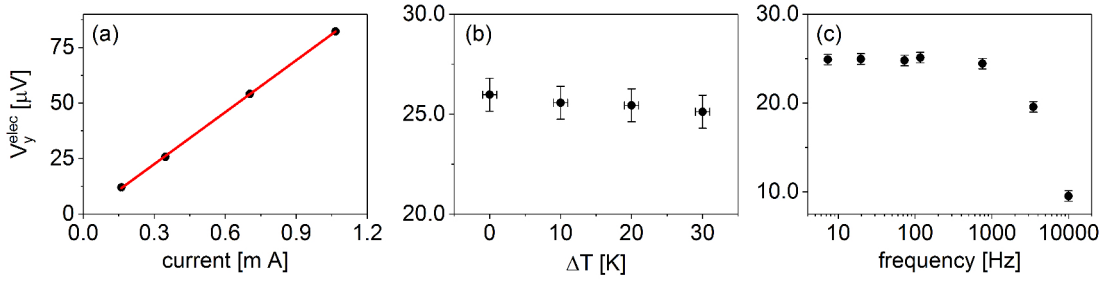

Figure 5.15.: The electrically induced AHE voltage is measured for varying (a) current (including a linear fit), (b) ΔT and (c) frequency to ensure a pure AHE signal which is not influenced by ∇T.

5.2. Magneto(thermo)electric investigation of Co/Pd multilayers

As mentioned earlier, two measurement modes are used to conclude and compare thermal and electrical transport coefficients. Firstly, only ∇T is the driving force for a longitudinal and transverse voltage and, thus, no superimposed signals due to different driving forces can occur in mode 1. But since in the measurement mode 2 additional to ∇T an alternating current is applied, the resulting voltages might be subject to superimposed origins. Therefore, the dependence of the transverse voltage on the driving current, the applied ∇T and the frequency of the current is recorded. Figure 5.15 shows the corresponding results. As can be seen in (a), the transverse voltage is proportional to the applied current, hence, the underlying ∇T does not give rise to an additional thermal contribution in measurement mode 2. This is also verified by (b), where ΔT is increased from zero to 30 K for alternating current of constant magnitude. Within the measurement uncertainty, the AHE voltage stays constant. Furthermore, the frequency of the alternating current is increased to exclude any frequency dependent artifacts on the AHE voltage. Figure 5.15 (c) shows that up to 1 kHz the AHE voltage stays constant before it drastically drops for higher frequencies. Because of these findings, a current of 0.5 mA is chosen for not altering the Hall bar due to too high current densities. A temperature difference of 30 K ensures a high ANE response and a frequency of 117 Hz guarantees to stay within the constant regime of the AHE response.

In the following, the temperature dependent signals of the multilayer with $t_{Co} = 0.3$ nm are representatively shown in detail. As before, the magnetic sweep direction from negative to positive fields is symbolized by the black branch of the results whereas the sweep direction from positive to negative values is represented by the red branch. Figure 5.16 shows V_{AHE} from (a) T_{base} = room temperature (RT) up to (e) T_{base} = 478 K. At each temperature, V_{AHE} shows a clear hysteresis with saturation values for $|H| > 2000$ Oe. With increasing temperature, the coercive fields continuously decrease indicating that the magnetization switches earlier for higher temperatures. Furthermore, the magnitude of V_{AHE}, $V_{mag} = (V_{+sat} - V_{-sat})/2$, increases linearly until it seems to saturate for temperatures around 500 K, see Fig. 5.16 (f). The high squareness of all curves verify the PMA also for high temperatures, showing that the Curie temperature is not reached until 500 K.

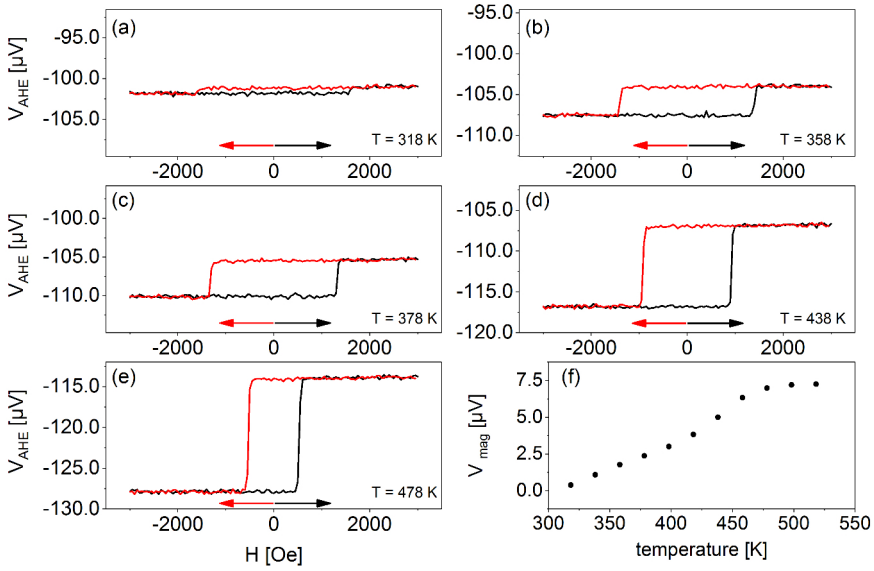

Figure 5.16.: (a)-(e) The AHE voltage of the multilayer with $t_{Co} = 0.3\,nm$ for increasing temperature shows a hysteresis with increasing magnitude and decreasing coercive fields. (f) The AHE magnitude first linearly increases with temperature before it seems to saturate for temperatures higher than 500 K.

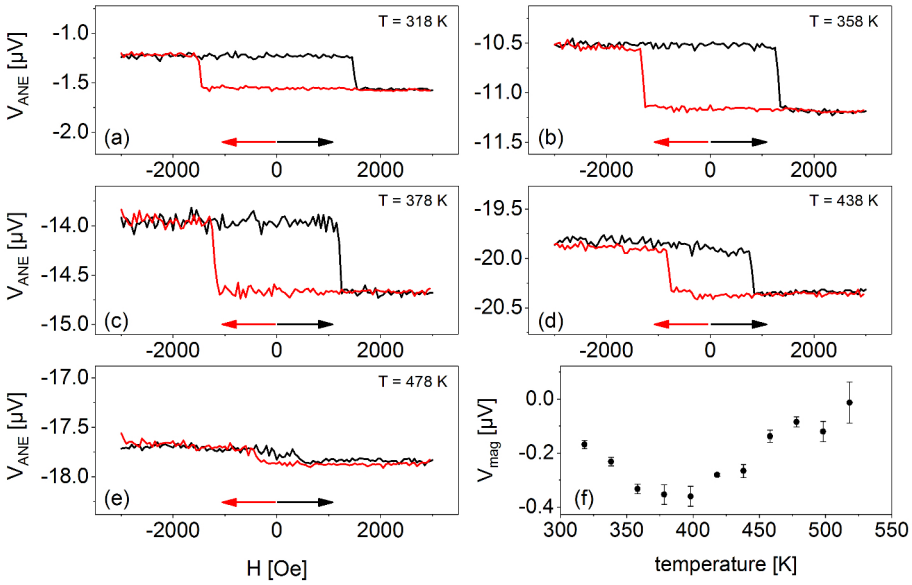

Figure 5.17.: (a)-(e) The ANE voltage of the multilayer with $t_{Co} = 0.3\,nm$ for increasing temperature shows a hysteresis with inverted polarity compared to the AHE and decreasing coercive fields. (f) The ANE magnitude first drops to a negative maximum at 400 K before it seems to linearly decrease to zero for high temperatures.

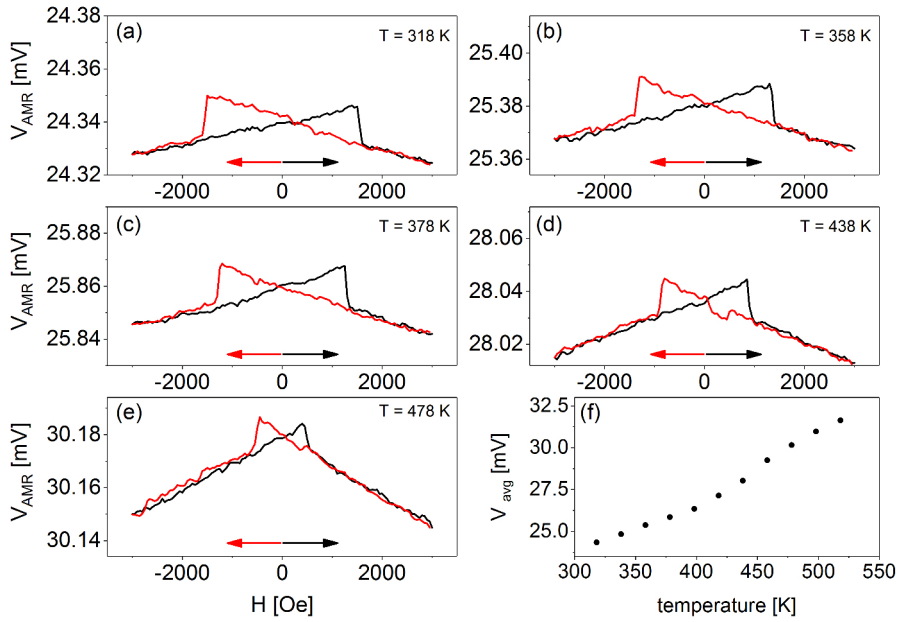

Figure 5.18.: (a)-(e) The AMR voltage of the multilayer with $t_{Co} = 0.3\,nm$ for increasing temperature shows a linear increase to a maximum voltage at H_c before it abruptly drops to a linear decreasing background voltage. (f) The average AMR voltage increases constantly with temperature.

Figure 5.17 (a)-(e) depicts V_{ANE} in the same temperature regime. Again, hysteresis curves can be recorded for $T_{base} < 500\,K$. In comparison to the AHE signal, the ANE has an inverted polarity and is about one order of magnitude smaller. Nevertheless, the squareness of the hysteresis again shows that the perpendicular magnetization reversal takes place over a narrow range of H, still indicating a fast switching and, thus, a PMA. As before, the coercive fields decrease with increasing temperature. But in contrast to the AHE, V_{mag} does not follow a linear temperature dependence, see Fig. 5.17 (f). Instead, it reaches a negative maximum around 400 K before decreasing nearly linearly to zero for high temperatures. However, no sign change can be observed within $320\,K \geq T_{base} \geq 520\,K$ for $t_{Co} = 0.3\,nm$.

So far, only the transverse voltage signals of measurement mode 1 (V_{ANE}) and measurement mode 2 (V_{AHE}) are described. For a quantitative comparison, also the longitudinal voltages of mode 1 ($V_{Seebeck}$) and mode 2 (V_{AMR}) have to be evaluated. Fig. 5.18 illustrates the temperature dependent AMR voltage simultaneously recorded with the AHE voltage. Starting from negative H, the voltage first increases linearly with increasing H until it reaches its maximum for positive H. It abruptly drops at the same coercive field as recorded for the AHE and ANE signal and then decreases linearly with further increasing H. When the field sweep goes back to zero, the voltage again increases linearly with the same slope as it has dropped before the magnetic sweep direction change. A maximum voltage is reached, before it drops down to the voltage of the increasing field branch at the negative coercive field. Further increasing the negative field linearly decreases the voltage. This behavior is seen for all temperatures, but the significant fields of

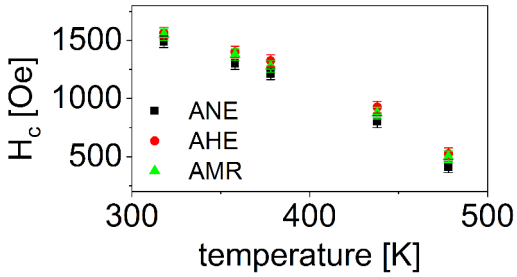

Figure 5.19.: The coercive fields of the AHE, ANE and AMR show the same temperature dependent decrease.

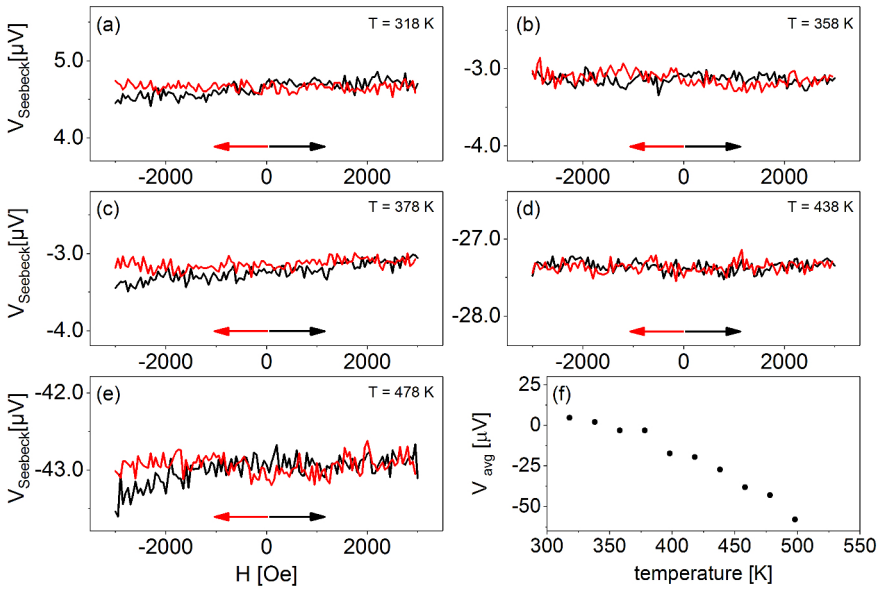

Figure 5.20.: (a)-(e) The longitudinal Seebeck voltage is independent of H and shows a constant voltage at each temperature. (f) The absolute average value constantly increase with temperature.

the voltage drops decrease with increasing temperature. Similar shapes of the AMR signal of Co(0.2 nm)/Pd(2 nm) multilayers have been earlier reported at 4 K [17]. The average signal of V_{AMR} is shown in Fig. 5.18 (f) and follows a linear temperature dependence.

When all coercive fields of the AHE, ANE and AMR measurements are compared, it shows that within the error uncertainties all measurements follow the same temperature dependent decrease of H_c (Fig. 5.19). This clearly proves that all of these effects follow the same magnetization dynamics, although their magnitudes have different dependencies on the temperature.

Figure 5.20 shows the longitudinal Seebeck voltages recorded together with the ANE. As expected, the Seebeck voltages do not show any dependencies on H and, thus, a constant voltage within the noise level is found for each temperature (see Fig. 5.20 (a)-(e)). The mean value of each signal is plotted vs. temperature in (f) and its absolute value continuously increase with increasing temperature.

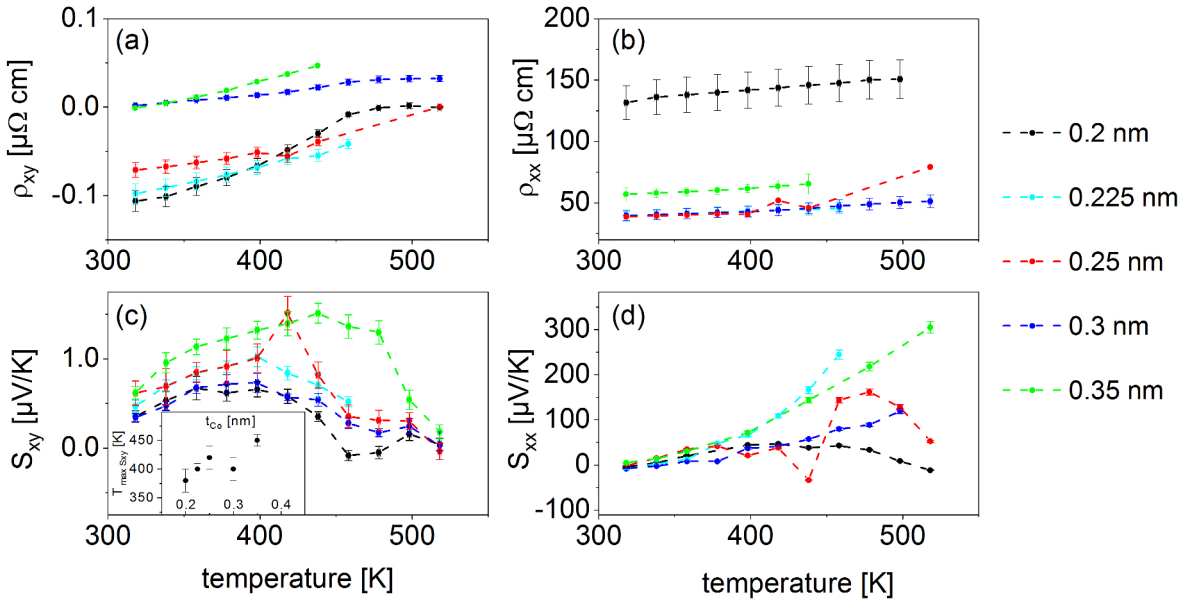

Figure 5.21.: The temperature dependent transport coefficients (a) ρ_{xy}, (b) ρ_{xx}, (c) S_{xy} and (d) S_{xx} of the Co/Pd multilayers for increasing Co thickness.

In the next step, the temperature dependent voltage signals of Figs. 5.16 (f), 5.17 (f), 5.18 (f) and 5.20 (f) are used to calculate the temperature dependent transport coefficients following Eqs. (4.17), (4.18), (4.20) and (4.21). This procedure is repeated for the multilayers with t_{Co}= 0.2 nm, 0.225 nm, 0.25 nm, 0.3 nm and 0.35 nm leading to the normalized transport coefficients depicted in Fig. 5.21. The dashed lines connecting the data points only act as guides to the eye. The anomalous Hall resistivity ρ_{xy} continuously increases with temperature for all t_{Co} and a sign change is observed between 0.25 nm and 0.3 nm at 320 K (see Fig. 5.21 (a)). A previous AHE study on the same multilayer systems found the sign change in ρ_{xy} also for $t_{Co} = 0.3$ nm but at 140 K [94]. This might be due to different production charges where different sputter targets result in differing sputter rates and could lead to an offset in the net multilayer or individual layer thickness. In the previous study, ρ_{xy}(320 K) ranges from -0.1 $\mu\Omega$ cm to +0.1 $\mu\Omega$ cm at and ρ_{xy}(320 K) of this study range from -0.1 $\mu\Omega$ cm to 0.0 $\mu\Omega$ cm. Hence, they lay in the same order of magnitude. Nevertheless it has to be mentioned that the data in (a) do not show a clear thickness dependent variation in ρ_{xy} as it is the case in the other study at low temperatures. It is reasonable that the thinnest sample shows the smallest AHE respond at 320 K. It contains the lowest ferromagnetic content resulting in the lowest magnetization which, in turn, highly influences the AHE. But the subsequent increase of t_{Co} does not yield a consistent increase of ρ_{xy}. For example, ρ_{xy}(320 K) equals for $t_{Co} = 0.3$ nm and 0.35 nm. Furthermore, the data set of $t_{Co} = 0.2$ nm shows a steeper increase with temperature than the thicker multilayers, leading to a crossing point at around 420 K. The measurements in the high temperature regime $T_{base} > 450$ K often lead to unstable AHE signals which is why the data sets for $t_{Co} = (0.225, 0.35)$ nm end at around 445 K and only the samples with $t_{Co} = (0.2, 0.25, 0.3)$ nm could be successfully measured up to 525 K.

However, comparing ρ_{xy}(T) with ρ_{xx}(T) shows a general increase by two orders of magnitude (Fig. 5.21 (b)). Beside the sample with $t_{Co} = 0.2\,nm$ the resistivities of all multilayers lay in the intermediate metallic regime within $40\,\mu\Omega\,cm$ to $60\,\mu\Omega\,cm$ [128]. ρ_{xx}(T) increases monotonically for all multilayers but due to the same reasons as for ρ_{xy}, the data sets for t_{Co} = (0.225, 0.35) nm are incomplete for high temperatures. The longitudinal resistivity being two orders of magnitude larger than the AHE resistivity has been earlier reported for low temperatures in (Co/Pd) multilayers [18, 94] as well as for face-centered-cubic (fcc) Co films [129] and, thus, the shown data seem to be generally reasonable. Because $\rho_{xx}(320\,K)$ of the same samples have also been evaluated between $45\,\mu\Omega\,cm$ to $55\,\mu\Omega\,cm$ in the study of Keskin *et al.* [94], the thicker multilayers lay within the same regime. But again two anomalies have to be mentioned. First, the multilayer with $t_{Co} = 0.2\,nm$ has a nearly three times higher resistivity than the multilayer with $t_{Co} = 0.3\,nm$. Although it is expected for thinner multilayers to have higher resistivities [130] because of a higher influence of interface scatter events, the increase of the resistivity into the dirty conduction regime ($\rho_{xx} > 100\,\mu\Omega\,cm$ [128]) rather seems to be a measurement artifact. And second, the thickest sample does not show the lowest resistivity although expected. Hence, a thickness dependent interpretation of the longitudinal resistivities can hardly be done.

The ANE measurements result in highly differing temperature dependencies of S_{xy} compared to the electrical transport coefficients, see Fig. 5.21 (c). With increasing temperature, S_{xy} first increases to a maximum value before it decreases to zero for higher temperatures. By increasing t_{Co} the width of the maximum becomes broader while the maximum obviously shifts to higher temperatures. The inset of Fig. 5.21 (c) shows the temperature of the maximum S_{xy}, $T_{max\ Sxy}$, depending on t_{Co}. With exception of $t_{Co} = 0.3\,nm$, $T_{max\ Sxy}$ monotonically increases for higher Co thicknesses. Although no sign change is observed in the range of $320\,K < T_{base} < 525\,K$, the trend of S_{xy} for T<370 K suggests a sign change for all t_{Co} within a temperature range between 250 K and 300 K. A sign change from positive to negative S_{xy} has been reported for Fe_3O_4 single crystals at 123 K [22]. Here, the temperature corresponds to the Verwey transition temperature, where a phase transition in magnetite changes its crystal lattice and, therefore, also its physical properties, e.g. its magnetization, specific heat or resistivity [131]. But also in ferromagnetic semiconductors a sign change in the transverse Seebeck coefficient is observed. Figure 5.22 shows (a) S_{yx}(T) and (b) S_{xx}(T) for different Mn amounts x in the $Ga_{1-x}Mn_xAs$ alloy [21]. In all samples, S_{yx}(T) increases for low temperatures developing a high peak of around $8\,\mu V/K$ and decreasing to $0\,\mu V/K$ for higher temperatures. Whereas the drop to $0\,\mu V/K$ is attributed to the excess of the Curie temperature, the origin of the sign change was not a subject of their investigation. Interestingly, a remarkable similarity to the measured data shown in Fig. 5.21 (c) is obtained. Both experiments show a broadening and a shift to higher temperatures of the peak for either an increased Co thickness within the multilayer or an increased amount of Mn in the semiconductor alloys. Only the positions of the peaks are found at nearly 300 K higher temperatures for the multilayers compared to the alloys. However, this similarity further points to a potential sign change of S_{xy} at temperatures slightly below room temperature.

The temperature dependent longitudinal Seebeck coefficients of the multilayers, S_{xx}(T), can be found in Fig. 5.21 (d). For all multilayers S_{xx} starts between -10 $\mu V/K$ and 5 $\mu V/K$ at 320 K and

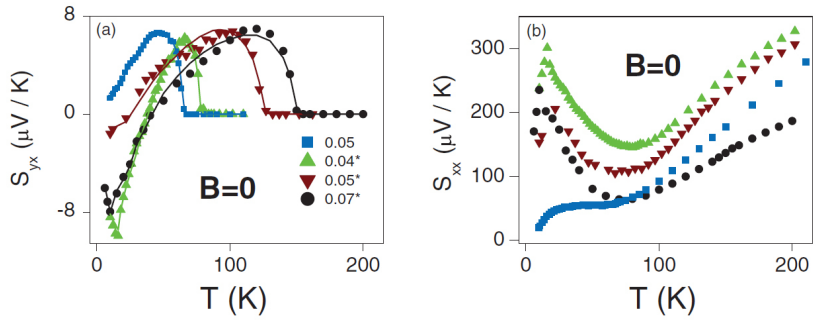

Figure 5.22.: The transverse (a) and longitudinal (b) Seebeck coefficients for $Ga_{1-x}Mn_xAs$ alloys, taken from Ref. [21].

increases with temperature. Whereas the multilayer with $t_{Co} = 0.2\,nm$ shows a broad maximum at around 420 K, the multilayer with $t_{Co} = 0.25\,nm$ rather develops a narrow maximum at 475 K. In contrast, all other samples only show a positive slope with maximum S_{xx} in the range of 100 μV/K to 300 μV/K. Again, these values can be compared to those of the study conducted on ferromagnetic semiconductors, Fig. 5.22 (b). These data also show the development of extrema (at around 25 K and 90 K) and vary within 200 μV/K in a range of 200 K. But with variation in x, the temperature dependence changes more continuously than that of the multilayers. Although both experiments show a principally different behavior of $S_{xx}(T)$, the order of magnitude of the multilayers Seebeck coefficients can be assumed as reasonable.

Pu *et al.* and Ramos *et al.* were able to fit the obtained $S_{xy}(T)$ data by the other transport coefficients $\rho_{xx}(T)$, $\rho_{xy}(T)$ and $S_{xx}(T)$ [21, 22]. Here, we follow their approach and discuss the validity of the Mott relation for the Co/Pd multilayer system. For a detailed discussion we concentrate on the multilayer with $t_{Co} = 0.3\,nm$, since it does not show any discontinuities or break downs of any transport coefficient for high temperatures. As described in Sec. 3.1.3, the transverse resistivity is conventionally plotted against the longitudinal resistivity and fitted by the power law ($\rho_{xy} = \lambda\,\rho_{xx}^{n}$) to obtain information about the underlying scatter mechanisms. Hence, ρ_{xy} is plotted vs. ρ_{xx} in Fig. 5.23. Classically, the power law is fitted to experimental data without any offsets, as shown in (a) for the power factors n = 2, 1, 0.5. Obviously, the pure power law is not suitable to consistently fit the experimental data. They rather suggest a residual ρ_{xy} for low ρ_{xx} or, equivalently, low temperatures. Much experimental effort has been conducted to conclude a unified AHE scaling law since it showed that it depends on the choice of materials, temperature range or varied between thin films or bulk materials. By using thin Fe films of different thickness, Tian *et al.* could individually tune the intrinsic and extrinsic contributions to the total scatter events and developed a model which also involves such a residual resistivity [132].

Based on the conventional separation of a linear extrinsic and a quadratic intrinsic scattering term

$$\rho_{xy} = a\,\rho_{xx} + b\,\rho_{xx}^{2} \quad , \tag{5.19}$$

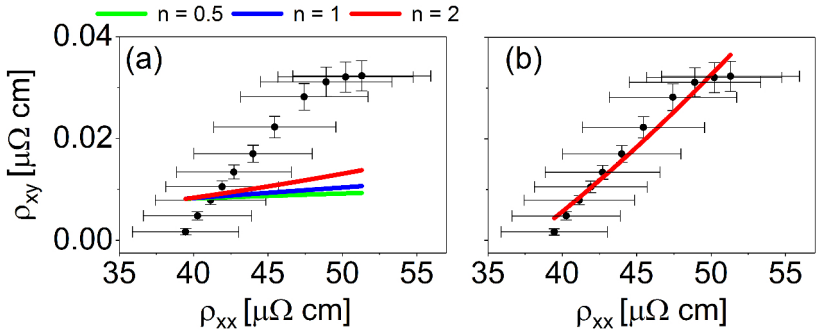

Figure 5.23.: The transverse resistivity plotted vs. the longitudinal resistivity for a Co/Pd multilayer with $t_{Co} = 0.3\,nm$. The data are fitted with (a) the classical scaling law $\rho_{xy} = \lambda\,\rho_{xx}^{n}$ for different n or (b) with the adjusted scaling law $\rho_{xy} = A + b\,\rho_{xx}^{2}$.

they pointed out that the linear term can have two origins with different magnitudes, a' and a'',

$$\rho_{xy} = a'\,\rho_{xx0} + a''\,\rho_{xxT} + b\,\rho_{xx}^{2} \quad , \tag{5.20}$$

with a residual resistivity, ρ_{xx0}, and a phonon-induced resistivity, ρ_{xxT}. Due to their low temperature experiment, they could determine ρ_{xx0}, ρ_{xxT} and ρ_{xx} and extract the fit parameters a', a'' and b. Interestingly, the phonon-induced scattering was negligible ($a'' \approx 0$) for all thicknesses so that further analysis allowed them to determine $a' = \alpha + \beta\,\rho_{xx0}$, with the magnitudes of skew and side-jump scattering, α and β. This lead to the scaling law

$$\begin{aligned} \rho_{xy} &= (\alpha\,\rho_{xx0} + \beta\,\rho_{xx0}^{2}) + b\,\rho_{xx}^{2} \\ &= A + b\,\rho_{xx}^{2} \end{aligned} \tag{5.21}$$

which, especially for films thinner than 6 nm, described their data significantly better than the classical scaling law. Thus, the first term represents the extrinsic (impurities scattering) and the second the intrinsic (electron-phonon scattering) contribution. Similar experiments are also done in t< 22 nm amorphous $Co_{40}Fe_{40}B_{20}$ films which further supports the adjusted scaling law [128]. The present study on Co/Pd multilayers is only conducted at high temperatures, thus, a determination of ρ_{xx0} and ρ_{xxT} is not possible. Hence, we can not investigate the parameters a', a'' and b at this point and, therefore, can not prove the non-existence of the linear term in Eq. (5.20). For a final conclusion whether a linear contribution to ρ_{xy} has to be taken into account the data set needs to be extended to low temperature data. However, since the adjusted scaling law was also verified by other works, we fitted our data by using Eq. (5.21), see Fig. 5.23 (b). It can be seen that the description of the experimental data is highly improved, compared to the classical scaling law. Although the shown data seem to correspond with Eq. (5.21), the physical interpretation of the obtained fit parameters has to be handled with care. Due to the investigation of multilayer systems, not only intrinsic and extrinsic scatter mechanisms influence both resistivities and have to be discussed independently. Each contribution furthermore consists of bulk, interface and surface contributions which, in turn, may also have different temperature

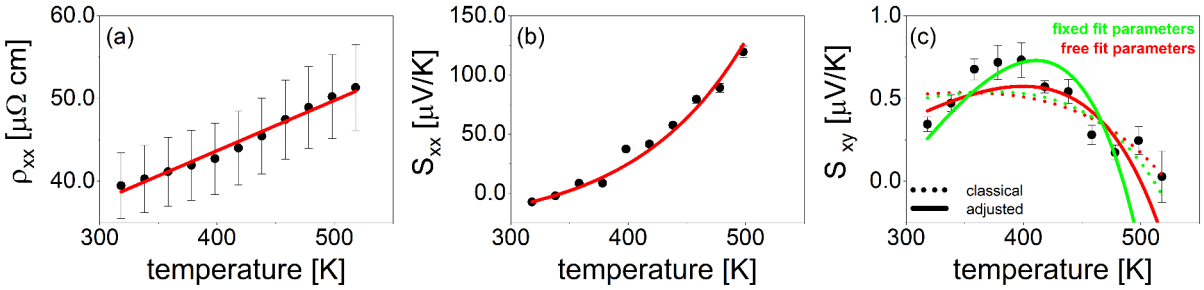

Figure 5.24.: Exemplary fitting of the transport coefficients of the Co/Pd multilayer with $t_{Co} = 0.3\,\mathrm{nm}$. (a) The longitudinal resistivity is fitted linearly, $\rho_{xx} = m\,T + \rho_{xx0}$, and (b) the longitudinal Seebeck coefficient exponentially, $S_{xx} = S_{xx0} + \exp\frac{T+T0}{c}$. (c) The anomalous Nernst coefficient is fitted by Eqs. (4.18) (dotted lines) and (5.27) (solid lines) for free fit parameters (red) or partially fixed fit paramets (green).

dependencies and impede a clear separation between intrinsic and extrinsic contributions. For this reason, Keskin *et al.* did not choose the scaling law to determine the underlying origin of the AHE, but alternatively used first principle calculations. By excluding thermal excitations at their low temperature experimental data [94], they independently calculated the intrinsic and side-jump contributions while assuming the skew-scattering to be suppressed. They conclude that the side-jump and intrinsic contribution are equal in sign and of comparable magnitude. By increasing the Co amount in their calculations, both scatter mechanisms converge to Co bulk values, pointing to competitive bulk and interfacial contributions to the total sign of the AHE resistivity. Hence, the determination of the physical origin of the AHE in multilayer systems at high temperature is non trivial and can not be finally identified within the conducted experiments.

However, for continuing the discussion of the anomalous Nernst coefficient S_{xy}, the determination of the off-diagonal thermoelectric conductivity tensor element, α_{xy}, is necessary. Following Pu and Ramos *et al.* [21, 22], α_{xy} is expressed in terms of ρ_{xx} and S_{xx} by utilizing the classical power law, $\rho_{xy} = \lambda\,\rho_{xx}^{n}$, and the Mott relation $S = \frac{\pi^2\,k_B^2}{3\,e}\,T\,\frac{\partial(\ln\sigma)}{\partial\epsilon}|_{\epsilon_F}$. With $\chi = \frac{\pi^2\,k_B^2}{3e}$ it writes (see attachments for details)

$$\alpha_{xy} = \rho_{xx}^{(n-2)}\left(\chi\,T\,\lambda' - \lambda(n-2)\,S_{xx}\right) \quad . \tag{5.22}$$

Here, λ and n are the fit parameters introduced by the power law and λ' the energy derivative of λ while ρ_{xx} and S_{xx} are measured as a function of temperature. $\alpha_{xy}\Big(\rho_{xx}(T),\,S_{xx}(T),T\Big)$ is then introduced into the expression of the off-diagonal Seebeck coefficient, leading to

$$S_{xy}\Big(\rho_{xx}(T),\,S_{xx}(T),\,T\Big) = \rho_{xx}(T)^{(n-1)}\left[\chi\,T\,\lambda' - (n-1)\,\lambda\,S_{xx}(T)\right] \quad . \tag{5.23}$$

Keeping n, λ and λ' as free fit parameters, this expression reconstructs the measured anomalous Nernst response in a temperature range of 10 K to 200 K, see Fig. 5.22 (a). In our experiment, the longitudinal resistivity and Seebeck coefficient of the $t_{Co} = 0.3\,\mathrm{nm}$ Co/Pd multilayer are

described by

$$\rho_{xx}(T) = 1.94 \cdot 10^{-7}\,\Omega\,\mathrm{m} + 6.1 \cdot 10^{-10}\,\frac{\Omega\,\mathrm{m}}{\mathrm{K}}\,T \tag{5.24}$$

and

$$S_{xx}(T) = -2.8 \cdot 10^{-5}\,\frac{\mathrm{V}}{\mathrm{K}} + 1.03\ 10^{-9}\frac{\mathrm{V}}{\mathrm{K}}\,\exp\left(\frac{T + 584.5\,\mathrm{K}}{90.9\,\mathrm{K}}\right) \quad , \tag{5.25}$$

see Fig. 5.24 (a) and (b). Consequently, Eqs. (5.24) and (5.25) are introduced into Eq. (5.23) to fit $\mathrm{S_{xy}(t_{Co} = 0.3\,nm)}$. The dotted lines in Fig. 5.24 (c) represent the fitting results gained by Eq. (5.23). The green dotted line results when n is fixed to 2 and the other parameters are left variable. It describes the temperature dependence at T>420 K relatively well but saturates for lower temperatures without developing the maximum around 400 K. For this reason, similar to Pu and Ramos, n is also freely fitted along with the other fit parameters, resulting in the red dotted fit. Whereas the slope for high temperatures decreases and, thus, agrees better with the data points, the function still misses a maximum and saturates around 0.5 $\frac{\mu\mathrm{V}}{K}$ for low temperatures.

This insufficient agreement is attributed to the usage of the classical scaling law during the derivation of Eq. (5.23). As described earlier, the electric transport coefficients of this study are rather related by the adjusted scaling law, Eq. (5.21). Thus, the changed scaling law has to be considered when deriving a proper formulation of S_{xy}. By using the same approach with the Mott relation but substituting the classic by the adjusted scaling law, α_{xy} reads (see attachment)

$$\alpha_{xy} = \chi\,T\,\rho_{xx}^{-2}\,\left(b'\,\rho_{xx}^{2} + A' + \frac{2\,A}{\chi}\,\frac{S_{xx}}{T}\right) \quad . \tag{5.26}$$

With Eq. (5.26) the expression of the anomalous Nernst coefficient transforms into

$$S_{xy}\Big(\rho_{xx}(T),\,S_{xx},\,(T)\,T\Big) = \rho_{xx}^{-1}(T)\,\left[\rho_{xx}^{2}(T)\,(\chi\,T\,b' - S_{xx}(T)\,b) + A\,S_{xx}(T) + A'\,\chi\,T\right] \quad . \tag{5.27}$$

Here, A and b are the fit parameters of the adjusted scaling law and A' and b' their corresponding energy derivatives. Now, Eq. (5.27) is used to fit the ANE coefficients of the $t_{Co} = 0.3$ nm Co/Pd multilayer, see the solid lines in Fig. 5.24 (c). By keeping all fit parameters free for fitting, the red solid line shows an enhanced agreement with the data points and also the development of a maximum around 400 K. By manually increasing A, A' and b, only leaving b' as a free fit parameter, the fitting curve can be manipulated to better fit the peak of the data points (Fig. 5.24 (c), solid green line). However, simultaneously the negative slope at high temperatures increases, leading to higher deviations between the experiment and theory for T>450 K. Thus, the best fit of the total data range is given by Eq. (5.27) while keeping all fit parameters free.

Hence, the longitudinal resistivities and Seebeck coefficients of the other multilayers (Fig. 5.21 (b), (d)) are similarly fitted and the validity of Eq. (5.27) is tested for $\mathrm{t_{Co}} = (0.2,\,0.225,\,0.25,\,0.35)$ nm. Figure 5.25 (a) depicts the resulting fits of all investigated multilayers. It can be seen that Eq. (5.27) generally describes the data well and mirrows the development of a maximum for

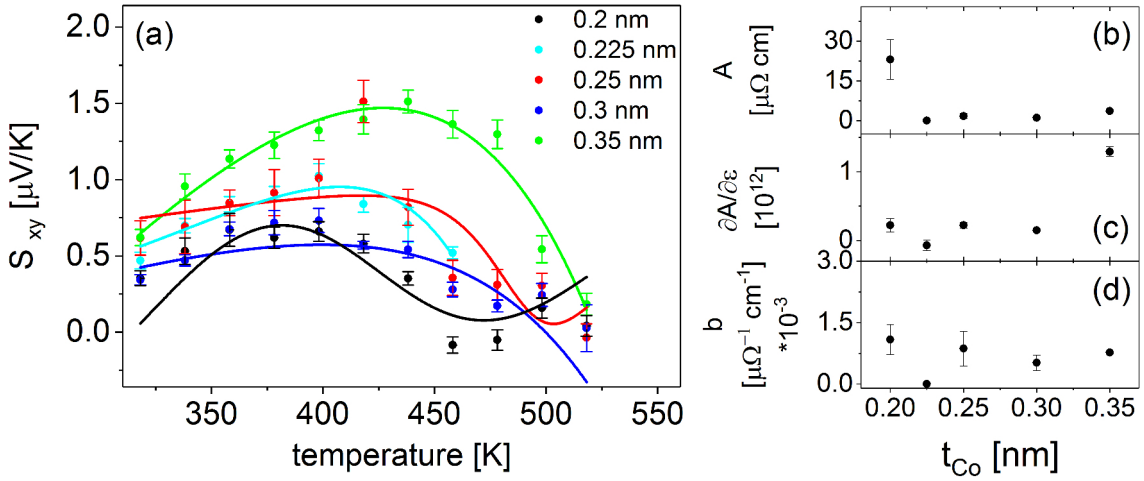

Figure 5.25.: (a) The ANE coefficients of all multilayers are fitted by Eq. (5.27). The resulting fit parameters A, A' and b are plotted thickness dependently in (b), (c) and (d).

all samples. The resulting fit parameters A, A' and b are thickness dependently plotted in Fig. 5.25 (b), (c) and (d). Obviously, the parameters do not show a continuous dependence on t_{Co} but, in general, stay within the same order of magnitude for all samples. $b'(t_{Co})$ is not shown since it is 1 for all samples and, by multiplying with χ which is in the order of 10^{-27}, has a negligible small influence on the fit of S_{xy}. In case of $t_{Co} = (0.225, 0.35)$ nm all data points are exceptionally well described by the fit, whereas the $t_{Co} = 0.3$ nm sample shows minimal deviations as described earlier. The fits of the samples with $t_{Co} = (0.2, 0.25)$ nm seem to develop a minimum of S_{xy} between 470 K and 500 K. This feature is probably attributed to the different behavior of their longitudinal Seebeck coefficients at high temperatures. As can be seen in Fig. 5.24 (d), these samples are the only ones which show a decrease of S_{xx} at high temperatures and, thus, their fits of S_{xy} are most likely determined by this high temperature behavior of S_{xx}. The real ANE experiment, however, is expected to converge to zero for temperatures above the Curie temperature. This behavior can not be predicted by the explained model since the implemented functions $S_{xx}(T)$ and $\rho_{xx}(T)$ do not reflect the temperature dependent decrease of the magnetization. This would only be regarded by a proper connection of the AHE (ρ_{xy}) to the AMR measurements (ρ_{xx}) via a solid theory of the scaling law for a broad temperature range.

The shown experiments were repeated for multiple heating cycles in order to verify the reproducibility of the results. It shows that the magnitude of S_{xy} degrades with increasing number of measurement cycles, especially in case of the thinner samples. In contrast, the electric transport coefficients show a very robust behavior over the measurement cycles. Although all samples are post annealed at higher temperature after preparation than any temperatures used during the experiment, the ANE coefficient is decreased. Since the post annealing process is conducted for 1 hour at 350° C, the samples might be temperature stable at short time scales. But since one measurement cycle lasts over 18h, the multilayers are exposed to temperatures above 100° C for several hours. This circumstance might lead to atomic diffusion which damps the ANE response, especially for the thinnest multilayers with $t_{Co} < 0.2$ nm. It was tried to track down any atomic

changes during the experiment with TEM investigations of thin lamellas cut by focused ion beam. But due to the sub monolayer thickness of the Co layers a successful investigation could not be achieved. This is another reason for recommending future experiments on thin multilayers to be conducted at lower temperatures.

6. Summary

This thesis discusses magnetoresistive, thermoelectric and magnetothermoelectric effects in magnetic thin films and multilayers. The first part of this thesis presents a new instrument for the rotation of thermal gradients in solid thin films. The presented tool opens a new degree of freedom for magnetothermoelectric investigations and, thus, allows detailed anisotropy studies for various sample systems. The novel setup realizes the ip rotation of a thermal gradient ∇T by the vectorial decomposition into two perpendicular thermal gradients of variable strength. This enables the application of ∇T at varied ip angles relative to the crystal structure without the need of reassembling the sample or the electric contacts. As a result, the simultaneous measurement of the AMTP and PNE has been made possible. The successful rotation of ∇T is first proven and analyzed by an IR camera, followed by the quantitative analysis of magnetothermopower effects in a Py thin film on MgO(001). Firstly, this is done by measuring the dependencies of the AMTP and PNE on the strength of an external magnetic field for different orientations φ for a fixed ∇T. Secondly, a saturation magnetic field is rotated ip the sample for increasing angle φ_{T} of ∇T. The initially recorded $\sin(2\varphi)$ oscillation of the voltage measured at $\varphi_{\mathrm{T}} = 0°$ subsequently shifts to a $\cos(2\varphi)$ oscillation at $\varphi_{\mathrm{T}} = 90°$. This phase shift unambiguously proves the rotation of ∇T and allows the quantitative separation of the AMTP, PNE and ordinary Seebeck effect. As a result, the relative change of the anisotropic Seebeck coefficient, ΔS, of Py can be estimated to $-(0.84 \pm 0.08)\%$.

In spin caloritronics, this experiment could help to investigate, e.g., the anisotropy of the spin Nernst magnetothermopower or the development of devices featuring specific crystal structures to enhance the thermoelectric energy conversion. Another promising usage of the setup could help with the identification of linear and quadratic contributions of the magnetization to magnetothermoelectric effects via the eight-directional method.

The second part of this work deals with the investigation of the AHE and ANE. Due to the relevance of the ANE in spin caloritronics, a detailed knowledge of its temperature dependence is helpful to exploit the ANE's full potential for thermoelectric devices or parasitic free measurements of the LSSE in metals. Because different studies show a relation between the ANE and the AHE, the ANE is investigated in thin $[\mathrm{Co_x/Pd_{1.5\,nm}}]_9$ multilayers which are known for a sign change of the AHE. This led to the development of an experiment which measures the magnetothermoelectric and magnetoelectric transport properties under same experimental conditions. Longitudinal and transverse voltage measurements are conducted for a temperature range from RT to 550 K with an applied temperature difference of 30 K. After the separation of the thermal and electric signals, the longitudinal and transverse electric and thermal transport coefficients can be extracted.

Thus, four transport coefficients, measured under identical experimental conditions, are analyzed depending on temperature and multilayer thickness. Whereas the earlier reported sign change of the AHE coefficient of $[Co_x/Pd_{1.5\,nm}]_9$ multilayers is observed, a sign change of the ANE coefficient stays undetected in the investigated temperature range. Instead, all data indicate a sign change of the ANE at lower temperatures between 100 K and 300 K. Furthermore, the transport coefficients are discussed in terms of Mott's law. This relation between the Seebeck coefficient and the energy derivative of the conductivity is reported to be valid in various sample systems. This could lead to the description of the ANE coefficient by the longitudinal resistivity, the AHE resistivity and the Seebeck coefficient. It shows that the already reported form of the relation is not capable of describing the experimental results but with slight changes within the mathematical derivation the agreement between experiment and theory can be significantly enhanced. To unambiguously identify a sign change of the ANE we suggest to focus future work onto the temperature range below RT. The combined measurement of all transport coefficients at low temperatures could further clarify the physical validity of the suggested theoretical model. Interestingly, a maximum of the ANE coefficient could be identified for each multilayer which could be of relevance for devices where the constructive superposition of the ANE with other, e.g. spin caloritronic, effects is desired to further enhance the heat-to-electricity efficiency.

A. Attachment

Magnetic field calibration

To calibrate the measured magnetic fields at the pole caps to the magnetic field at the sample's position a third Hall sensor has been positioned in the center, aligned with either magnetic axis 1 or 2. For different d_{core} the magnetic field was sweeped and recorded for both positions, the pole cap and the center, respectively. Fig. A.1 (a) and (b) show that the magnetic field at the sample's position is linearly decreased compared to that at the pole caps. For this reason, the slope of a linear fit gives the attenuation ratio for each magnetic axis and each d_{core}, shown in Fig. A.1 (c). Fitting these ratios with a second grade polynomial allow to interpolate the attenuation ratios for $d_{core} = [8\,\text{mm}, 11\,\text{mm}]$ and, thus, to conclude the magnetic field at the samples position by measuring it at the pole caps.

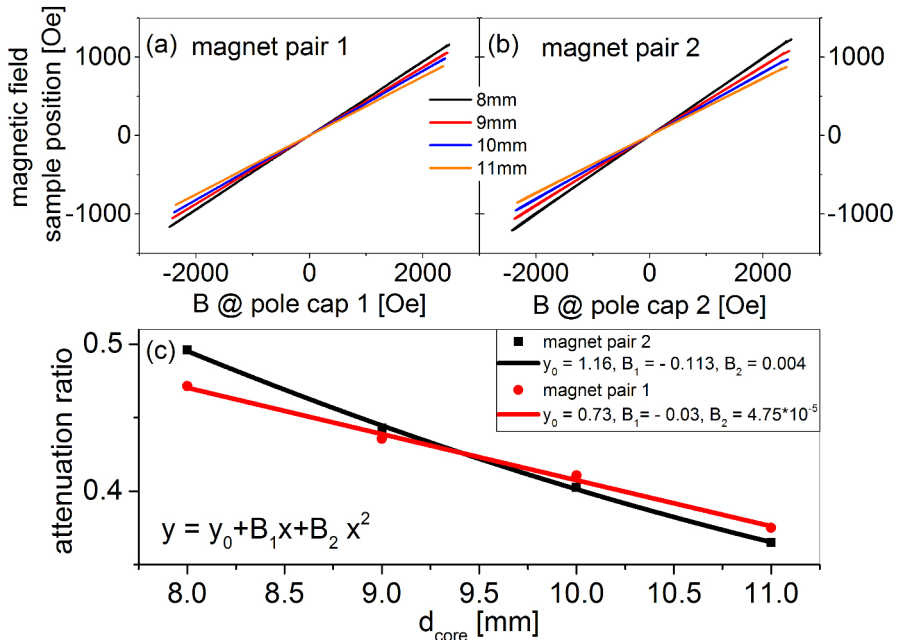

Figure A.1.: (a), (b) The magnetic field at the samples position is linearly decreased compared to the magnetic field at the pole caps of each magnetic axis. The linear slope for each d_{core} can be fitted (c) and used to achieve the attenuation ratios for $8\,\text{mm} \leq d_{core} \leq 11\,\text{mm}$.

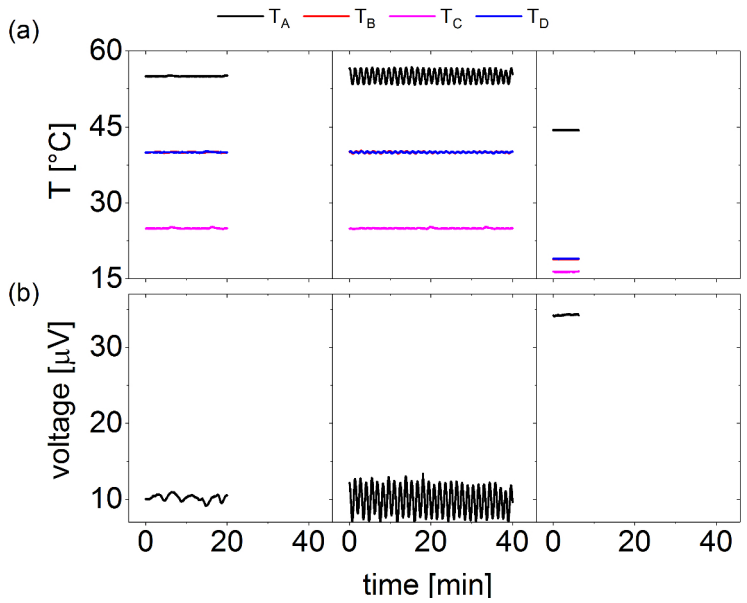

Figure A.2.: (a) Temperature distribution of all heaters and (b) background offset voltage for different PID settings. Slowest PID regulation (left), fastest PID regulation (middle); PID regulation turned off and manually controlled output current for Peltier elements (right).

PID characterization

After a systematical change of the PID parameters, two opposite states of the thermal system are chosen to stress the correlation between thermal and voltage oscillations. Figure A.2 shows three different settings of the PID controllers: The left side represents the system's behavior when the parameters are set to the slowest possible reaction time to suppress the oscillations as best as possible. Although ΔT has aligned at 0.3 K for all heaters, the resulting offset voltage still continuously changes within 1 μV. In contrast to that, the middle part shows the fastest system response. A clear increase in both, the thermal and voltage oscillations, can be observed in that case. Only if the PID controllers are turned off and the current of the Peltier elements is manually fixed, the temperatures stay constant within 0.1 K, resulting in a voltage background noise of 0.1 μV (see Fig. A.2, right).

The reason why not even the slowest settings can compensate the thermal oscillations lies within the working principle of a PID controller. In general, a PID controller has to determine a time dependent process parameter y(t) to smoothly approach a setpoint r(t) (Fig. A.3 (a)). For example, it might be used to open a valve for reaching a specific pressure in a gas chamber or, as in this setup, to adjust temperatures. This is done by an output voltage of the PID controller, u(t). This response u(t) can be calculated by

$$u(t) = K_p\, e(t) + K_i \int_0^t e(\tau)\, d\tau + K_d \frac{de(t)}{dt} \tag{A.1}$$

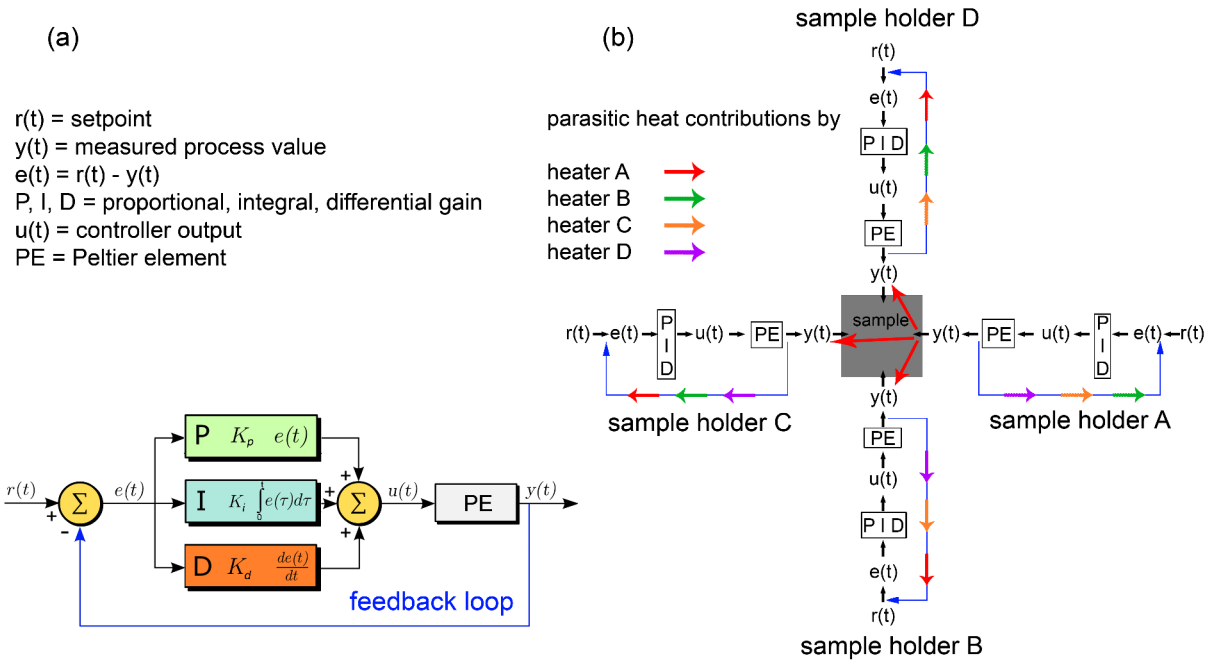

Figure A.3.: (a) A scheme of a PID circuit (based on Refs. [133, 134]). A process variable y(t) shall reach a setpoint r(t). Therefore it is adjusted by the PID response u(t) which is calculated using the error e(t)=r(t)-y(t). (b) The setup can be described by a thermally coupled system of four PID feedback loops. All feedback loops underlay parasitic heat contributions of the other heaters, hence, making it difficult to totally stabilize ∇T.

and is based on a feedback loop. By measuring y(t) and comparing it to the setpoint r(t) the time dependent error e(t)=r(t)-y(t), which is tried to be minimized over time, can be calculated. Equation A.1 shows the proportional (P), integral (I) and derivative (D) terms which account for the magnitude, the preceding values and the rate of change of the error, respectively [133, 134]. By the right choice of P, I and D, arbitrary process parameters such as temperatures or gas pressures can smoothly saturate at the setpoints without overshooting or oscillating.

However, independent of the choice of the parameters, any change of $y(t)_i$ will only be attributed to a change of $u(t)_i$ from the same feedback loop. This is the case if an isolated, thermally decoupled system is regarded. In contrast, the described setup represents a thermally coupled system, see Fig. A.3 (b). Individually described, each sample holder with its Peltier element (indicated by the index i) represents a closed PID feedback loop (blue arrows), in which $y(t)_i$ is adjusted only by its own variation of $u(t)_i$. But since all sample holders are in thermal contact with the sample, for example a change of $y(t)_A$ will also effect $y(t)_{B,C,D}$ (indicated by large red arrows). For this reason, all $y(t)_i$ will have parasitic contributions of the other heaters (indicated by red, orange, green and violet small arrows). Therefore, the parasitic external contributions to $y(t)_i$ will also influence the feedback loops and corrections of $e(t)_i$. Now, each PID controller tries to compensate its deviation $e(t)_i$ but since it has contributions of extrinsic origin (which by themselves are actively driven), can not minimize it to zero. This destabilizes the total thermal

system. This issue might be solved by using a multi-channel PID controller which is capable of controlling four output channels. These kinds of controllers might regard the influence of one output channel to the others and, thus, could decrease the oscillating offset voltages.

Measurement uncertainties of transport coefficients

Based on Eqs. (4.17), (4.18), (4.21) and (4.20) the corresponding measurement uncertainties are estimated to

$$\mathrm{d}S_{\mathrm{xx}} = \left|-\frac{D}{\Delta T\, l}\cdot\sigma\left(\overline{V}_{\mathrm{x}}^{\mathrm{Seebeck}}\right)\right| + \left|-\frac{\overline{V}_{\mathrm{x}}^{\mathrm{Seebeck}}}{\Delta T\, l}\cdot\mathrm{d}D\right| + \left|\frac{\overline{V}_{\mathrm{x}}^{\mathrm{Seebeck}}\, D}{\Delta T^2\, l}\cdot\mathrm{d}\Delta T\right| \quad , \tag{A.2}$$

$$\mathrm{d}S_{\mathrm{xy}} = \left|-\frac{D}{\Delta T\, l}\,\mathrm{d}V^{\mathrm{ANE}}\right| + \left|-\frac{V^{\mathrm{ANE}}}{\Delta T\, l}\,\mathrm{d}D\right| + \left|\frac{V^{\mathrm{ANE}}\, D}{\Delta T^2\, l}\,\mathrm{d}\Delta T\right| \quad , \tag{A.3}$$

$$\mathrm{d}\rho_{\mathrm{xx}} = \left|\frac{w\, t_{\mathrm{tot}}}{I_{\mathrm{x}}\, l}\,\sigma(\overline{V}_{\mathrm{x}}^{\mathrm{AMR}})\right| + \left|-\frac{\overline{V}_{\mathrm{x}}^{\mathrm{AMR}}}{I_{\mathrm{x}}^2}\,\frac{w\, t_{\mathrm{tot}}}{l}\,\mathrm{d}I_{\mathrm{x}}\right| + \left|\frac{\overline{V}_{x}^{\mathrm{AMR}}}{I_{\mathrm{x}}}\,\frac{w}{l}\,\mathrm{d}t_{\mathrm{tot}}\right| \quad , \tag{A.4}$$

and

$$\mathrm{d}\rho_{\mathrm{xy}} = \left|\frac{t_{\mathrm{tot}}}{I_{\mathrm{x}}}\,dV_{\mathrm{y}}^{\mathrm{AHE}}\right| + \left|-\frac{V_{\mathrm{y}}^{\mathrm{AHE}}}{I_{\mathrm{x}}^2}\,t_{\mathrm{tot}}\,dI_{\mathrm{x}}\right| + \left|\frac{V_{\mathrm{y}}^{\mathrm{AHE}}}{I_{\mathrm{x}}}\,dt_{\mathrm{tot}}\right| \quad . \tag{A.5}$$

Cross linking of off-diagonal transport coefficients

As described in Sec. 3.1.2, the thermoelectric tensor is connected to the conductivity tensor. Considering a transverse thermoelectric measurement only including AHE and ANE contributions, Eq. (3.17) can be written only for the considered off-diagonal components

$$\alpha_{\mathrm{xy}} = \left(\frac{\pi^2\, k_{\mathrm{B}}^2}{3\, e}\right) T\, \frac{d}{d\epsilon}[\sigma_{\mathrm{xy}}(\epsilon)]_{\mu} \quad . \tag{A.6}$$

The off-diagonal elements of the conductivity tensor can be expressed by elements of the resistivity tensor $\sigma_{\mathrm{xy}} = \frac{\rho_{\mathrm{xy}}}{\rho_{\mathrm{xx}}^2+\rho_{\mathrm{xy}}^2}$. When the off-diagonal response is assumed to be smaller than the diagonal response $\rho_{\mathrm{xy}} \ll \rho_{\mathrm{xx}}$, as it is the case in the given experiment (see Fig. 5.24 (a), (b)), it simplifies to

$$\sigma_{\mathrm{xy}} \approx \frac{\rho_{\mathrm{xy}}}{\rho_{\mathrm{xx}}^2} \quad . \tag{A.7}$$

With Eq. (A.7) and $\sigma_{\mathrm{xx}} = 1/\rho_{\mathrm{xx}}$, the power law of the AHE (Eq. (3.35)) can be converted into an expression for the conductivity tensor elements

$$\begin{aligned} \rho_{\mathrm{xy}} &= \lambda\, \rho_{\mathrm{xx}}^{\mathrm{n}} = \sigma_{\mathrm{xy}}\, \rho_{\mathrm{xx}}^2 \\ \Leftrightarrow \sigma_{\mathrm{xy}} &= \lambda\, \rho_{\mathrm{xx}}^{n-2} \\ &= \lambda\, \sigma_{\mathrm{xx}}^{2-n} \quad , \end{aligned} \tag{A.8}$$

which is used to calculate the energy derivative of Eq. (A.6)

$$\frac{\partial}{\partial\epsilon}[\sigma_{\mathrm{xy}}(\epsilon)]_\mu = \left(\frac{\partial\lambda}{\partial\epsilon}\right)_\mu \sigma_{\mathrm{xx}}^{(2-n)} + \lambda(2-n)\sigma_{\mathrm{xx}}^{(1-n)}\left(\frac{\partial\sigma_{\mathrm{xx}}}{\partial\epsilon}\right)_\mu \quad . \tag{A.9}$$

With $\lambda' = \partial\lambda/\partial\epsilon_{|\mu}$ and inserting the energy derivative into Eq. (A.6) one obtains

$$\alpha_{\mathrm{xy}} = \frac{\pi^2\, k_{\mathrm{B}}^2}{3e}\, T\, \sigma_{\mathrm{xx}}^{(2-n)}\left(\lambda' + \lambda(2-n)\frac{\left(\frac{\partial\sigma_{\mathrm{xx}}}{\partial\epsilon}\right)_\mu}{\sigma_{\mathrm{xx}}}\right) \quad , \tag{A.10}$$

which transforms with the Mott relation (Eq. (3.18)) into

$$\alpha_{\mathrm{xy}} = \frac{\pi^2\, k_{\mathrm{B}}^2}{3e}\, T\, \sigma_{\mathrm{xx}}^{(2-n)}\left(\lambda' + \lambda(2-n)\,\frac{3\,e}{\pi^2\, k_{\mathrm{B}}^2}\, S_{\mathrm{xx}}\right) \quad . \tag{A.11}$$

The transverse thermoelectric matrix element can therefore be described by the resistivity $\rho = \rho_{\mathrm{xx}}$, the Seebeck coefficient $S = S_{\mathrm{xx}}$ and the three fit parameters n, λ and λ' resulting from the power law of the AHE

$$\alpha_{\mathrm{xy}} = \rho^{(n-2)}\left(\frac{\pi^2\, k_{\mathrm{B}}^2}{3e}\, T\, \lambda' - \lambda(n-2)\, S\right) \quad . \tag{A.12}$$

The electric field along y induced by a temperature gradient along the x-direction is described by the off-diagonal Seebeck coefficient S_{xy}. Following Ref. [22], this electric field has two origins. Firstly, the off-diagonal thermoelectric tensor element is responsible for a direct conversion of a longitudinal heat current into a transverse charge current. Secondly, the charge current along x, induced by the ordinary Seebeck effect (described by S_{xx}) is deflected by the Hall effect into the y-direction. This conversion efficiency is described by the Hall angle $\Theta_{\mathrm{H}} = \frac{\sigma_{\mathrm{xy}}}{\sigma_{\mathrm{xx}}}$. Thus, the total off-diagonal Seebeck coefficient adjusts to

$$\frac{E_{\mathrm{y}}}{\nabla_{\mathrm{x}} T} = S_{\mathrm{xy}} = \rho\alpha_{\mathrm{xy}} - S\frac{\sigma_{\mathrm{xy}}}{\sigma_{\mathrm{xx}}} \quad . \tag{A.13}$$

Inserting Eq. A.12 into Eq. (A.13) and utilizing Eq. (A.8) leads to

$$\begin{aligned} S_{\mathrm{xy}} &= \rho^{(n-1)}\left[\chi\, T\, \lambda' - (n-2)\lambda S\right] - S\,\frac{\sigma_{\mathrm{xy}}}{\sigma} \\ &= \rho^{(n-1)}\left[\chi\, T\, \lambda' - (n-2)\lambda S\right] - S\,\rho_{\mathrm{xx}}\,\lambda\,\sigma^{2-n} \\ &= \rho^{(n-1)}\left[\chi\, T\, \lambda' - (n-2)\lambda S\right] - S\,\rho_{\mathrm{xx}}\,\lambda\,\rho^{n-2} \\ &= \rho^{(n-1)}\left[\chi\, T\, \lambda' - (n-2)\lambda S\right] - S\,\lambda\,\rho^{n-1} \\ &= \rho^{(n-1)}\left[\chi\, T\, \lambda' - (n-1)\lambda S\right] \quad . \end{aligned} \tag{A.14}$$

Note this derivation is based on the assumption, that ρ_{xy} is correlated to ρ_{xx} via the classical power law. Since the here shown samples seem to follow another correlation, the derivation of $\mathrm{S_{xy}}$ has to be adjusted. Eq. (A.6) and Eq. (A.7) are still valid, but with the adjusted power law,

Eq. (A.8) changes to

$$\begin{aligned} \rho_{\mathrm{xy}} &= A + b\,\rho_{xx}^2 = \sigma_{\mathrm{xy}}\,\rho_{\mathrm{xx}}^2 \\ \Leftrightarrow \sigma_{\mathrm{xy}} &= A\,\rho_{\mathrm{xx}}^{-2} + b \\ &= b + A\,\sigma_{\mathrm{xx}}^2 \quad . \end{aligned} \tag{A.15}$$

Thus, the energy derivative of σ_{xy} writes

$$\frac{\partial}{\partial\epsilon}\left[\sigma_{\mathrm{xy}}(\epsilon)\right]_\mu = \left(\frac{\partial b}{\partial\epsilon}\right)_\mu + \left(\frac{\partial A}{\partial\epsilon}\right)_\mu \sigma_{\mathrm{xx}}^2 + A\,(2\,\sigma_{\mathrm{xx}})\,\left(\frac{\partial\sigma_{\mathrm{xx}}}{\partial\epsilon}\right)_\mu \quad . \tag{A.16}$$

Hence, the off-diagonal thermoelectric tensor is

$$\begin{aligned} \alpha_{\mathrm{xy}} &= \chi\,T\left(b' + A'\,\sigma_{\mathrm{xx}}^2 + 2\,A\,\sigma_{\mathrm{xx}}\,\frac{\partial\sigma_{\mathrm{xx}}}{\partial\epsilon}\right) \\ &= \chi\,T\,\sigma_{\mathrm{xx}}^2\left(\frac{b'}{\sigma_{\mathrm{xx}}^2} + A' + 2\,A\,\frac{\frac{\partial\sigma_{\mathrm{xx}}}{\partial\epsilon}}{\sigma_{\mathrm{xx}}}\right) \\ &= \chi\,T\,\sigma_{\mathrm{xx}}^2\left(\frac{b'}{\sigma_{\mathrm{xx}}^2} + A' + 2\,A\,\frac{S_{\mathrm{xx}}}{\chi\,T}\right) \\ &= \chi\,T\,\rho_{\mathrm{xx}}^{-2}\left(b'\,\rho_{\mathrm{xx}}^2 + A' + \frac{2\,A}{\chi}\,\frac{S_{\mathrm{xx}}}{T}\right) \quad , \end{aligned} \tag{A.17}$$

with A' and b' being the energy derivatives of the fit parameters A and b. Introducing Eq. (A.15) and (A.17) into Eq. (A.13) gives

$$\begin{aligned} S_{\mathrm{xy}} &= \chi\,T\,\rho_{\mathrm{xx}}^{-1}\left(b'\,\rho_{\mathrm{xx}}^2 + A' + \frac{2\,A}{\chi}\,\frac{S_{\mathrm{xx}}}{T}\right) - S_{\mathrm{xx}}\,\rho_{\mathrm{xx}}\,\left(b + A\,\sigma_{\mathrm{xx}}^2\right) \\ &= \rho_{\mathrm{xx}}^{-1}\left(\chi\,T b'\rho_{\mathrm{xx}}^2 + A'\,\chi\,T + 2\,A\,S_{\mathrm{xx}} - S_{\mathrm{xx}}\,\rho_{\mathrm{xx}}^2\,b - S_{\mathrm{xx}}\,A\right) \\ &= \rho_{\mathrm{xx}}^{-1}\left[\rho_{\mathrm{xx}}^2\,\left(\chi\,T\,b' - S_{\mathrm{xx}}\,b\right) + A\,S_{\mathrm{xx}} + A'\,\chi\,T\right] \quad . \end{aligned} \tag{A.18}$$

XRD measurement

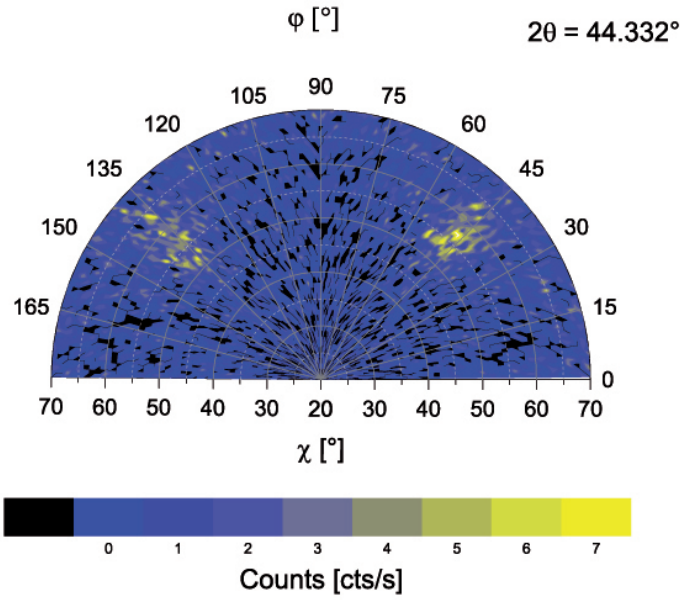

Figure A.4.: XRD measurements via the Euler cradle confirm the four-fold diffraction pattern of a cubic crystal structure of the investigated Py film.

Optical detection of ∇T rotation

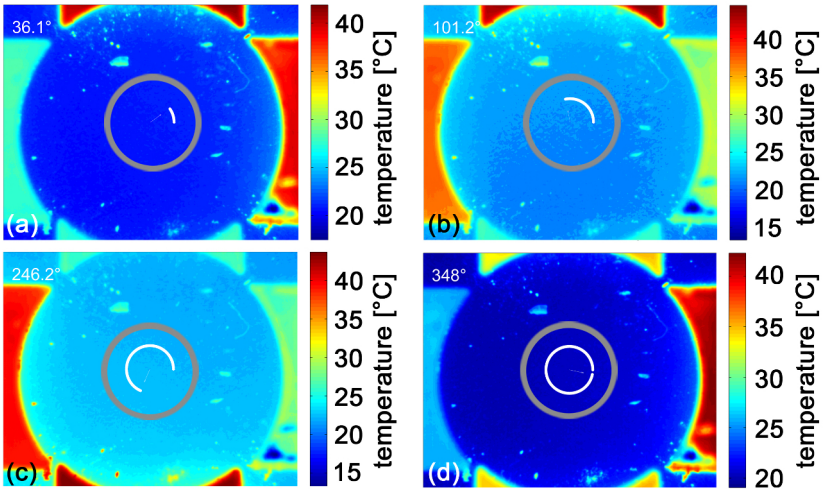

Figure A.5.: The MgO substrate with applied ∇T at $\varphi_T = 45°$ (a), 105° (b), 240° (c) and 360° (d). The calculated output angles within the ROI prove the rotation of ∇T within ±12°.

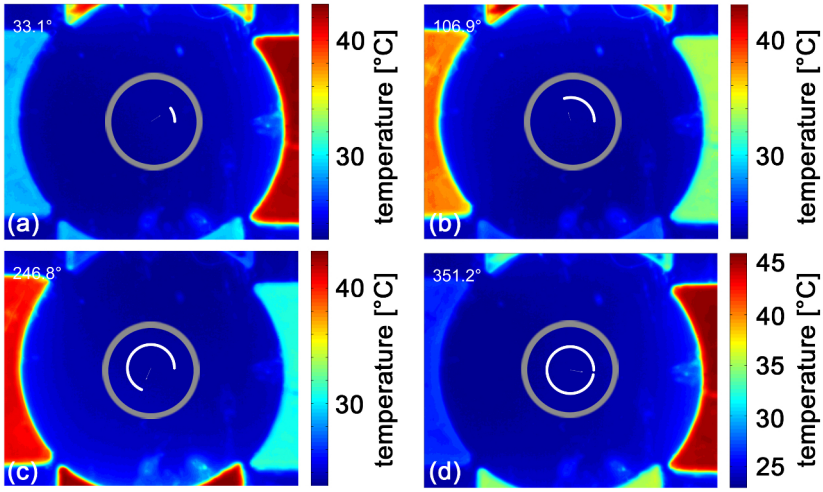

Figure A.6.: The MAO substrate with applied ∇T at $\varphi_T = 45°$ (a), 105° (b), 240° (c) and 360° (d). The calculated output angles within the ROI prove the rotation of ∇T within ±12°.

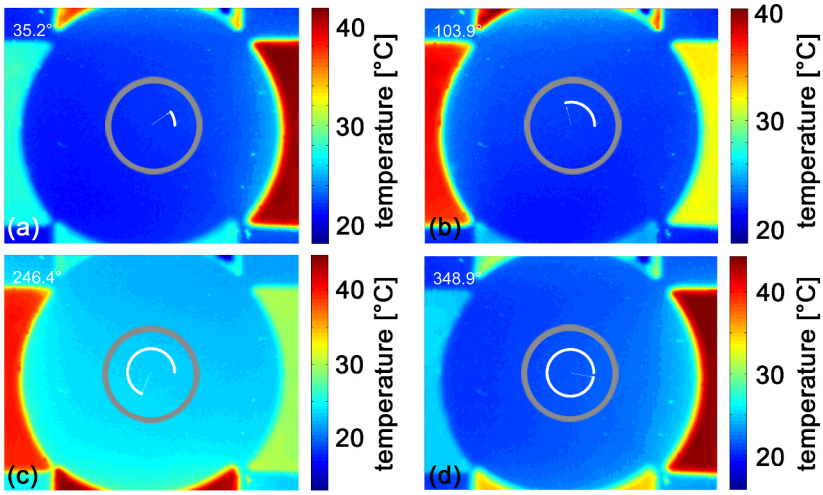

Figure A.7.: The Sa substrate with applied ∇T at $\varphi_T = 45°$ (a), 105° (b), 240° (c) and 360° (d). The calculated output angles within the ROI prove the rotation of ∇T within ±11°.

B. List of Figures

C. Bibliography

[1] H. Rong, H. Zhang, S. Xiao, C. Li, and C. Hu. Optimizing energy consumption for data centers. *Renewable and Sustainable Energy Reviews*, 58:674–691, 2016.

[2] M. N. Baibich, J. M. Broto, A. Fert, F. Nguyen Van Dau, F. Petroff, P. Etienne, G. Creuzet, A. Friederich, and J. Chazela. Giant Magnetoresistance of (001)Fe/(001)Cr Magnetic Superlattices. *Phys. Rev. Lett.*, 61(21):2472, 1988.

[3] G. Binasch, P. Grünberg, F. Saurenbach, and W. Zinn. Enhanced magnetoresistance in layered magnetic structures with antiferromagnetic interlayer exchange. *Phys. Rev. B*, 39 (7):4828–4830, 1989.

[4] A. Hoffmann and S. D. Bader. Opportunities at the Frontiers of Spintronics. *Phys. Rev. Applied*, 4(4):47001, 2015.

[5] V. V. Kruglyak, S. O. Demokritov, and D. Grundler. Magnonics. *J. Phys. D: Appl. Phys.*, 43(26):264001, 2010.

[6] A. V. Chumak, V. I. Vasyuchka, A. A. Serga, and B. Hillebrands. Magnon spintronics. *Nat. Phys.*, 11(6):453–461, 2015.

[7] S. B. Riffat and X. Ma. Thermoelectrics: A review of present and potential applications. *Applied Thermal Engineering*, 23(8):913–935, 2003.

[8] X. F. Zheng, C. X. Liu, Y. Y. Yan, and Q. Wang. A review of thermoelectrics research - Recent developments and potentials for sustainable and renewable energy applications. *Renewable and Sustainable Energy Reviews*, 32(1):486–503, 2014.

[9] G. Bauer, E. Saitoh, and B. J. van Wees. Spin caloritronics. *Nat. Mat.*, 11(5):391–399, 2012.

[10] K.-I. Uchida, H. Adachi, T. Ota, H. Nakayama, S. Maekawa, and E. Saitoh. Observation of longitudinal spin-Seebeck effect in magnetic insulators. *Appl. Phys. Lett.*, 97(17):172505, 2010.

[11] S. R. Boona, R. C. Myers, and J. P. Heremans. Spin caloritronics. *Energy Environ. Sci.*, 7 (3):885, 2014.

[12] K.-I. Uchida, H. Adachi, T. Kikkawa, A. Kirihara, M. Ishida, S. Yorozu, S. Maekawa, and E. Saitoh. Thermoelectric Generation Based on Spin Seebeck Effects. *Proc. IEEE*, 104 (10):1946–1973, 2016.

[13] S. Iwasaki. Perpendicular magnetic recording: Evolution and future. *IEEE Trans. Magn.*, 20(5):657–662, 1984.

[14] D. Litvinov, T. A. Roscamp, T. Klemmer, M.-L. Wu, J. K. Howard, and S. Khizroev. Co/Pd multilayer based recording layers for perpendicular media. *Mat. Res. Soc. Symp. Proc.*, 674:3.9.1–3.9.6, 2001.

[15] S. Kim, S. R. Lee, and J. D. Chung. Magnetic properties of Pd/Co multilayer films studied by Hall effect. *J. Appl. Phys.*, 73(10):6344–6346, 1993.

[16] S. U. Jen, B. L. Chao, and C. C. Liu. Hall effect of polycrystalline Co–Pd alloys. *J. Appl. Phys.*, 76(10):5782–5785, 1994.

[17] Y. Aoki, K. Honda, H. Sato, Y. Kobayashi, S. Hashimoto, T. Yokoyama, and T. Hanyu. The extraordinary Hall effect of Pd/Co multilayers. *J. Magn. Magn. Mater.*, 162(1):1–6, 1996.

[18] D. Rosenblatt, M. Karpovski, and A. Gerber. Reversal of the extraordinary Hall effect polarity in thin Co/Pd multilayers. *Appl. Phys. Lett.*, 96(2):022512, 2010.

[19] K.-D. Lee, D.-J. Kim, H. Yeon Lee, S.-H. Kim, J.-H. Lee, K.-M. Lee, J.-R. Jeong, K.-S. Lee, H.-S. Song, J.-W. Sohn, S.-C.l Shin, and B.-G. Park. Thermoelectric Signal Enhancement by Reconciling the Spin Seebeck and Anomalous Nernst Effects in Ferromagnet/Non-magnet Multilayers. *Sci. Rep.*, 5:10249, 2015.

[20] S. A. Wolf, D. D. Awschalom, R. A. Buhrman, J. M. Daughton, S. von Molnar, M. L. Roukes, A. Y. Chtchelkanova, and D. M. Treger. Spintronics: A spin-based electronics vision for the future. *Science*, 294:1488, 2001.

[21] Y. Pu, D. Chiba, F. Matsukura, H. Ohno, and J. Shi. Mott relation for anomalous Hall and Nernst effects in $Ga_{1-x}Mn_xAs$ ferromagnetic semiconductors. *Phys. Rev. Lett.*, 101(11): 117208, 2008.

[22] R. Ramos, M. H. Aguirre, A. Anadón, J. Blasco, I. Lucas, K. Uchida, P. A. Algarabel, L. Morellón, E. Saitoh, and M. R. Ibarra. Anomalous Nernst effect of Fe_3O_4 single crystal. *Phys. Rev. B*, 90(5), 2014.

[23] K. Behnia. *Fundamentals of Thermoelectricity*. University Press, Oxford, 1 edition, 2015.

[24] nanoHUB U. Nanoelectronics: Basic concepts, 2015.

[25] nanoHUB U. Fundamentals of Nanoelectronics: The new Perspective: Conductance formula, 2015.

[26] T. J. Seebeck, editor. *Magnetische Polarisation der Metalle und Erze durch Temperature Differenz*. 1821.

[27] T. J. Seebeck. Ueber die magnetische Polarisation der Metalle und Erze durch Temperatur Differenz. *Ann. Phys.*, 1826, 1826.

[28] C. Jeong, R. Kim, M. Luisier, S. Datta, and M. S. Lundstrom. On Landauer versus Boltzmann and full band versus effective mass evaluation of thermoelectric transport coefficients. *J. Appl. Phys.*, 107:023707, 2010.

[29] G. D. Mahan and J. O. Sofo. The best thermoelectric. *Proc. Natl. Acad. Sci. USA*, 93: 7436–7439, 1996.

[30] T. J. Scheidemantel, C. Ambrosch-Draxl, T. Thonhauser, J. V. Badding, and J. O. Sofo. Transport coefficients from first-principles calculations. *Phys. Rev. B*, 68(12):331, 2003.

[31] nanoHUB U. Thermoelectricity: Bottom-up Approach: Seebeck Coefficient, 2014.

[32] J. Nickel. Magnetoresistance Overview.

[33] S. Tumanski. Modern magnetic field sensors - a review. *Przeglad Elektrotechniczny*, 89: 1–12, 2013.

[34] D. Thompson, L. Romankiw, and A. Mayadas. Thin film magnetoresistors in memory, storage, and related applications. *IEEE Trans. Magn.*, 11(4):1039–1050, 1975.

[35] W. Thomson. On the electro-dynamic qualities of metals: effects of magnetization on the electric conductivity of nickel and of iron. *Proc. Royal Soc. London*, 8:546, 1856.

[36] T. McGuire and R. Potter. Anisotropic magnetoresistance in ferromagnetic 3d alloys. *IEEE Transactions on Magnetics*, 11(4):1018–1038, 1975.

[37] E. H. Hall. On a New Action of the Magnet on Electric Currents. *Am. J. Math.*, 2(3): 287–292, 1879.

[38] E. H. Hall. XXXVIII. On the new action of magnetism on a permanent electric current. *Philos. Mag.*, 10(63):301–328, 1880.

[39] G. S. Leadstone. The discovery of the Hall effect. *Physics Education*, 14(6):374–379, 1979.

[40] E. H. Hall. On the "Rotational Coefficient" in nickel and cobalt. *Philos. Mag.*, 12(74): 157–172, 1881.

[41] E. M. Pugh. Hall Effect and the Magnetic Properties of Some Ferromagnetic Materials. *Phys. Rev.*, 36:1503–1511, 1930.

[42] N. Nagaosa, J. Sinova, S. Onoda, A. H. MacDonald, and N. P. Ong. Anomalous Hall effect. *Rev. Mod. Phys.*, 82(2):1539–1592, 2010.

[43] A. Hoffmann. Spin Hall Effects in Metals. *IEEE Trans. Magn.*, 49(10):5172–5193, 2013.

[44] R. Karplus and J. M. Luttinger. Hall Effect in Ferromagnetics. *Phys. Rev. Applied*, 95(5): 1154–1161, 1954.

[45] M. Gradhand, D. V. Fedorov, F. Pientka, P. Zahn, I. Mertig, and B. L. Györffy. First-principle calculations of the Berry curvature of Bloch states for charge and spin transport of electrons. *J. Phys.: Condens. Matter*, 24(21):213202, 2012.

[46] L. Berger. Side-Jump Mechanism for the Hall Effect of Ferromagnets. *Phys. Rev. B*, 2(11): 4559–4566, 1970.

[47] J. Smit. The spontanous Hall effect in Ferromagnetics I. *Physica (Amsterdam)*, 21:877–887, 1955.

[48] J. Smit. The spontaneous Hall effect in ferromagnetics II. *Physica*, 24:39–51, 1958.

[49] C. Kooi. Hall Effect in Ferromagnetics. *Phys. Rev.*, 95:843, 1954.

[50] V. D. Ky. The planar Nernst effect in permalloy films. *phys. stat. sol.*, 17:207, 1966.

[51] A. von Ettingshausen and W. Nernst. Ueber das Auftreten electromotorischer Kräfte in Metallplatten, welche von einem Wärmestrome durchflossen werden und sich im magnetischen Felde befinden. *Ann. Phys. Chem.*, 265:343, 1886.

[52] S.-Q. Shen. Spintronics and Spin current. *AAPPS Bulletin*, 18(5):29, 2008.

[53] I. Zutic, J. Fabian, and S. Das Sarma. Spintronics: Fundamentals and applications. *Rev. Mod. Phys.*, 76(76):323–410, 2004.

[54] Y. Kajiwara, K. Harii, S. Takahashi, J. Ohe, K. Uchida, M. Mizuguchi, H. Umezawa, H. Kawai, K. Ando, K. Takanashi, S. Maekawa, and E. Saitoh. Transmission of electrical signals by spin-wave interconversion in a magnetic insulator. *Nature*, 464(7286):262–266, 2010.

[55] D. Awschalom and N. Samarth. Spintronics without magnetism. *Physics*, 2(50):467, 2009.

[56] J. Hirsch. Spin Hall Effect. *Phys. Rev. Lett.*, 83(9):1834–1837, 1999.

[57] Y. K. Kato, R. C. Myers, A. C. Gossard, and D. D. Awschalom. Observation of the spin Hall effect in semiconductors. *Science*, 306(5703):1910–1913, 2004.

[58] J. Wunderlich, B. Kaestner, J. Sinova, and T. Jungwirth. Experimental observation of the spin-Hall effect in a two-dimensional spin-orbit coupled semiconductor system. *Phys. Rev. Lett.*, 94(4):047204, 2005.

[59] E. Saitoh, M. Ueda, H. Miyajima, and G. Tatara. Conversion of spin current into charge current at room temperature: Inverse spin-Hall effect. *Appl. Phys. Lett.*, 88(18):182509, 2006.

[60] T. Jungwirth, J. Wunderlich, and K. Olejník. Spin Hall effect devices. *Nat. Mater.*, 11(5): 382–390, 2012.

[61] T. Kuschel and G. Reiss. Spin orbitronics: Charges ride the spin wave. *Nat. Nanotech.*, 2014.

[62] M. Althammer, S. Meyer, H. Nakayama, M. Schreier, S. Altmannshofer, M. Weiler, H. Huebl, S. Geprägs, M. Opel, R. Gross, D. Meier, C. Klewe, T. Kuschel, J.-M. Schmalhorst, G. Reiss, L. Shen, A. Gupta, Y.-T. Chen, G. Bauer, E. Saitoh, and Goennenwein, S. T. B. Quantitative study of the spin Hall magnetoresistance in ferromagnetic insulator/normal metal hybrids. *Phys. Rev. B*, 87(224401):1–15, 2013.

[63] Goennenwein, S. T. B. and G. Bauer. Spin caloritronics: electron spins blow hot and cold. *Nature nanotechnology*, 7(3):145–147, 2012.

[64] M. Johnson and Silsbee R. H. Thermodynamic analysis of interfacial transport and of the thermomagnetoelectric system. *Phys. Rev. B*, 35(10):4959–4972, 1987.

[65] G. Bauer, Allan H. MacDonald, and Sadamichi Maekawa. Spin Caloritronics. *Solid State Communications*, 150(11-12):459–460, 2010.

[66] K. Uchida, S. Takahashi, K. Harii, J. Ieda, W. Koshibae, K. Ando, S. Maekawa, and E. Saitoh. Observation of the spin Seebeck effect. *Nature*, 455(7214):778–781, 2008.

[67] M. Schmid, S. Srichandan, D. Meier, T. Kuschel, J.-M. Schmalhorst, M. Vogel, G. Reiss, C. Strunk, and C. H. Back. Transverse Spin Seebeck Effect versus Anomalous and Planar Nernst Effects in Permalloy Thin Films. *Phys. Rev. Lett.*, 111(18):7201, 2013.

[68] D. Meier, Reinhardt, D., Schmid, M., C. H. Back, J.-M. Schmalhorst, T. Kuschel, and G. Reiss. Influence of heat flow directions on Nernst effects in Py/Pt bilayers. *Phys. Rev. B*, 88:184425, 2013.

[69] D. Meier, D. Reinhardt, M. van Straaten, C. Klewe, M. Althammer, M. Schreier, Goennenwein, S. T. B., A. Gupta, M. Schmid, C. H. Back, J.-M. Schmalhorst, T. Kuschel, and G. Reiss. Longitudinal spin Seebeck effect contribution in transverse spin Seebeck effect experiments in Pt/YIG and Pt/NFO. *Nat. Comm.*, 6:8211, 2015.

[70] A. S. Shestakov, M. Schmid, D. Meier, T. Kuschel, and C. H. Back. Dependence of transverse magnetothermoelectric effects on inhomogeneous magnetic fields. *Phys. Rev. B*, 92(22), 2015.

[71] N. F. Mott. The Electrical Conductivity of Transition Metals. *Proc. Royal Soc. A London*, 153(880):699–717, 1936.

[72] I. I. Mazin. How to Define and Calculate the Degree of Spin Polarization in Ferromagnets. *Phys. Rev. Lett.*, 83(7):1427–1430, 1999.

[73] D. J. Sanders and D. Walton. Effect of magnon-phonon thermal relaxation on heat transport by magnons. *Phys. Rev. B*, 15(3):1489–1494, 1977.

[74] C. M. Jaworski, J. Yang, S. Mack, D. D. Awschalom, R. C. Myers, and J. P. Heremans. Spin-seebeck effect: a phonon driven spin distribution. *PRL*, 106(18):186601, 2011.

[75] A. Kirihara, K.-I. Uchida, Y. Kajiwara, M. Ishida, Y. Nakamura, T. Manako, E. Saitoh, and S. Yorozu. Spin-current-driven thermoelectric coating. *Nat. Mater.*, 11(8):686–689, 2012.

[76] Z. Qiu, K. Ando, K. Uchida, Y. Kajiwara, R. Takahashi, H. Nakayama, T. An, Y. Fujikawa, and E. Saitoh. Spin mixing conductance at a well-controlled platinum/yttrium iron garnet interface. *Appl. Phys. Lett.*, 103(9):092404, 2013.

[77] M. B. Jungfleisch, V. Lauer, R. Neb, A. V. Chumak, and B. Hillebrands. Improvement of the yttrium iron garnet/platinum interface for spin pumping-based applications. *Appl. Phys. Lett.*, 103(2):022411, 2013.

[78] Y. Saiga, K. Mizunuma, Y. Kono, J. C. Ryu, H. Ono, M. Kohda, and E. Okuno. Platinum thickness dependence and annealing effect of the spin-Seebeck voltage in platinum/yttrium iron garnet structures. *Appl. Phys. Express*, 7(9):093001, 2014.

[79] D. Kikuchi, M. Ishida, K. Uchida, Z. Qiu, T. Murakami, and E. Saitoh. Enhancement of spin-Seebeck effect by inserting ultra-thin $Fe_{70}Cu_{30}$ interlayer. *Appl. Phys. Lett.*, 106(8): 082401, 2015.

[80] M. Morota, Y. Niimi, K. Ohnishi, D. H. Wei, T. Tanaka, H. Kontani, T. Kimura, and Y. Otani. Indication of intrinsic spin Hall effect in 4d and 5d transition metals. *Phys. Rev. B*, 83(17):174405, 2011.

[81] H. L. Wang, C. H. Du, Y. Pu, R. Adur, P. C. Hammel, and F. Y. Yang. Scaling of spin Hall angle in 3d, 4d, and 5d metals from $Y_3Fe_5O_{12}$/metal spin pumping. *Phys. Rev. Lett.*, 112(19):197201, 2014.

[82] B. F. Miao, S. Y. Huang, D. Qu, and C. L. Chien. Inverse spin Hall effect in a ferromagnetic metal. *Phys. Rev. Lett.*, 111(6):066602, 2013.

[83] P. Laczkowski, J.-C. Rojas-Sánchez, W. Savero-Torres, H. Jaffrès, N. Reyren, C. Deranlot, L. Notin, C. Beigné, A. Marty, J.-P. Attané, L. Vila, J.-M. George, and A. Fert. Experimental evidences of a large extrinsic spin Hall effect in AuW alloy. *Appl. Phys. Lett.*, 104 (14):142403, 2014.

[84] C. M. Jaworski, J. Yang, S. Mack, D. D. Awschalom, J. P. Heremans, and R. C. Myers. Observation of the spin-Seebeck effect in a ferromagnetic semiconductor. *Nat. Mater.*, 9 (11):898–903, 2010.

[85] L. Chen, F. Matsukura, H. Ohno, and Lin Chen. Direct-current voltages in (Ga,Mn)As structures induced by ferromagnetic resonance. *Nat. Comm.*, 4:2055, 2013.

[86] J.-C. Lee, L.-W. Huang, D.-S. Hung, T.-H. Chiang, J. C. A. Huang, J.-Z. Liang, and S.-F. Lee. Inverse spin Hall effect induced by spin pumping into semiconducting ZnO. *Appl. Phys. Lett.*, 104(5):052401, 2014.

[87] K. Ando, S. Watanabe, S. Mooser, E. Saitoh, and H. Sirringhaus. Solution-processed organic spin-charge converter. *Nat. Mater.*, 12(7):622–627, 2013.

[88] Z. Qiu, M. Uruichi, D. Hou, K. Uchida, H. M. Yamamoto, and E. Saitoh. Spin-current injection and detection in k-(BEDT-TTF)$_2$Cu[N(CN)$_2$]Br. *AIP Advances*, 5(5):057167, 2015.

[89] P. Bougiatioti, C. Klewe, D. Meier, O. Manos, O. Kuschel, J. Wollschläger, L. Bouchenoire, S. D. Brown, J.-M. Schmalhorst, G. Reiss, and T. Kuschel. Quantitative Disentanglement of the Spin Seebeck, Proximity-Induced, and Ferromagnetic-Induced Anomalous Nernst Effect in Normal-Metal-Ferromagnet Bilayers. *Phys. Rev. Lett.*, 119(22):227205, 2017.

[90] D. Meier, T. Kuschel, L. Shen, A. Gupta, T. Kikkawa, K. Uchida, E. Saitoh, J.-M. Schmalhorst, and G. Reiss. Thermally driven spin and charge currents in thin $NiFe_2O_4$/Pt films. *Phys. Rev. B*, 87(5):054421, 2013.

[91] Y. Shiomi, Y. Handa, T. Kikkawa, and E. Saitoh. Transverse thermoelectric effect in $La_{0.67}$ $Sr_{0.33}$ MnO_3/$SrRuO_3$ superlattices. *Appl. Phys. Lett.*, 106(23):232403, 2015.

[92] R. Ramos, T. Kikkawa, M. H. Aguirre, I. Lucas, A. Anadón, T. Oyake, K. Uchida, H. Adachi, J. Shiomi, P. A. Algarabel, L. Morellón, S. Maekawa, E. Saitoh, and M. R. Ibarra. Unconventional scaling and significant enhancement of the spin Seebeck effect in multilayers. *Phys. Rev. B*, 92(22):220407, 2015.

[93] R. Ramos, T. Kikkawa, A. Anadón, I. Lucas, K. Uchida, P. A. Algarabel, L. Morellón, M. H. Aguirre, E. Saitoh, and M. R. Ibarra. Temperature dependence of the spin Seebeck effect in $[Fe_3O_4/Pt]_n$ multilayers. *AIP Advances*, 7(5):055915, 2017.

[94] V. Keskin, B. Aktaş, J. Schmalhorst, G. Reiss, H. Zhang, J. Weischenberg, and Y. Mokrousov. Temperature and Co thickness dependent sign change of the anomalous Hall effect in Co/Pd multilayers: An experimental and theoretical study. *Appl. Phys. Lett.*, 102(2):022416, 2013.

[95] S. Meyer, Y-T Chen, S. Wimmer, M. Althammer, T. Wimmer, R. Schlitz, S. Geprägs, H. Huebl, D. Ködderitzsch, H. Ebert, G. Bauer, R. Gross, and Goennenwein, S. T. B. Observation of the spin Nernst effect. *Nat. Mater.*, 16:977–981, 2017.

[96] J. Flipse, F. K. Dejene, D. Wagenaar, G. Bauer, J. Ben Youssef, and B. J. van Wees. Observation of the Spin Peltier Effect for Magnetic Insulators. *Phys. Rev. Lett.*, 113(2), 2014.

[97] L. Onsager. Reciprocal Relations in Irreversible Processes. I. *Phys. Rev.*, 38(12):405–426, 1931.

[98] C. Fang, C. H. Wan, Z. H. Yuan, L. Huang, X. Zhang, H. Wu, Q. T. Zhang, and X. F. Han. Scaling relation between anomalous Nernst and Hall effect in $[Pt/Co]_n$ multilayers. *Phys. Rev. B*, 93(5):054420, 2016.

[99] M. Bovender. *Konstruktion und Test eines Aufbaus für spinkalorische Messungen mit vektoriellem Temperaturgradienten*. Bachelor thesis, University Bielefeld, Bielefeld, 2015.

[100] F. K. Dejene, J. Flipse, and B. J. van Wees. Spin-dependent Seebeck coefficients of $Ni_{80}Fe_{20}$ and Co in nanopillar spin valves. *Phys. Rev. B*, 86(2), 2012.

[101] R. S. Crisp and J. Rungis. Thermoelectric power and thermal conductivity in the silver-gold alloy system from 3-300K. *Philosophical Magazine*, 22(176):217–236, 1970.

[102] C. Meola and G. M. Carlomagno. Recent advances in the use of infrared thermography. *Meas. Sci. Technol.*, 15(9):R27–R58, 2004.

[103] W. Wien. Ueber die Energievertheilung im Emissionsspectrum eines schwarzen Körpers. *Ann. Phys.*, 8:662–669, 1896.

[104] W. Lang, K. Kuhl, and H. Sandmaier. Absorbing layers for thermal infrared detectors. *Sensors and Acuators A*, 34:243–248, 1992.

[105] D. G. Stinson and S.-C. Shin. Magnetization and anisotropy of Co/Pd multilayer thin films. *Journal of Applied Physics*, 67(9):4459–4461, 1990.

[106] den Broeder, F. J. A., W. Hoving, and P. J. H. Bloemen. Magnetic anisotropy of multilayers. *Journal of Magnetism and Magnetic Materials*, 93:562–570, 1991.

[107] J. I. Hong, S. Sankar, A. E. Berkowitz, and W. F. Egelhoff. On the perpendicular anisotropy of Co/Pd multilayers. *J. Magn. Magn. Mater.*, 285(3):359–366, 2005.

[108] H.-S. Lee, S.-B. Choe, S.-C. Shin, and C. G. Kim. Characterization of magnetic properties in Co/Pd multilayers by Hall effect measurement. *J. Magn. Magn. Mater.*, 239(1-3): 343–345, 2002.

[109] Z. Kugler. *Perpendicular anisotropy in magnetic tunnel junctions*. Dissertation, Bielefeld University, Bielefeld, 2012.

[110] M. Meinert. *The Heusler alloy CoMnSb in magnetic tunnel junctions and high temperature TMR measurements*. Diploma thesis, University Bielefeld, Bielefeld, 2008.

[111] T. Matalla-Wagner. *Anomaler Nernst Effekt in magnetischen Multischichtsystemen und Legierungen*. Bachelor thesis, University Bielefeld, Bielefeld, 2013.

[112] M. van Straaten. *Untersuchungen des Anomalen Hall und Nernst Effekts in Co/Pd Multischichtsystemen*. Master thesis, University Bielefeld, Bielefeld, 2015.

[113] T. Kuschel, T. Becker, D. Bruns, M. Suendorf, F. Bertram, P. Fumagalli, and J. Wollschläger. Uniaxial magnetic anisotropy for thin Co films on glass studied by magnetooptic Kerr effect. *J. Appl. Phys.*, 109(9):093907, 2011.

[114] C. Daboo, R.-J. Hicken, E. Gu, M. Gester, S. J. Gray, D. E. P. Eley, E. Ahmad, J. A. C. Bland, and Ploessl, R. and Chapman, J. N. Anisotropy and orientational dependence of magnetization reversal processes in epitaxial ferromagnetic thin films. *Phys. Rev. B*, 51 (22):15964, 1995.

[115] J. Chen and J. L. Erskine. Surface-step-induced magnetic anisotropy in thin epitaxial Fe films on W(001). *Phys. Rev. Lett.*, 68(8):1212–1215, 1992.

[116] Y. Park, E. E. Fullerton, and S. D. Bader. Growth-induced uniaxial in-plane magnetic anisotropy for ultrathin Fe deposited on MgO(001) by oblique-incidence molecular beam epitaxy. *Appl. Phys. Lett.*, 66(16):2140, 1995.

[117] Q.-F. Zhan, S. Vandezande, and C. van Haesendonck. Manipulation of in-plane uniaxial anisotropy in FeMgO(001) films by ion sputtering. *Appl. Phys. Lett.*, 91:122510, 2007.

[118] Q.-F. Zhan, S. Vandezande, K. Temst, and C. van Haesendonck. Magnetic anisotropies of epitaxial Fe/MgO(001) films with varying thickness and grown under different conditions. *New J. Phys.*, 11(6):063003, 2009.

[119] A. Kaibi, A. Guittoum, R. M. Öksüzoglu, A. M. Yagci, M. Boudissa, and M. Kechouane. Structure, microstructure and magnetic properties of $Ni_{75}Fe_{25}$ films elaborated by evaporation from nanostructured powder. *App. Sur. Sci.*, 350:50, 2015.

[120] X. Li, X. Sun, J. Wang, and Q. Liu. Magnetic properties of permalloy films with different thicknesses deposited onto obliquely sputtered Cu underlayers. *J. Magn. Magn. Mater.*, 377:142–146, 2015.

[121] A. G. Gurevich and G. A. Melkov. *Magnetization oscillations and waves*. CRC Press, 1996.

[122] A. Aharoni. Demagnetizing factors for rectangular ferromagnetic prisms. *J. Appl. Phys.*, 83(6):3432–3434, 1998.

[123] L. F. Yin, D. H. Wei, N. Lei, L. H. Zhou, C. S. Tian, G. S. Dong, X. F. Jin, L. P. Guo, Q. J. Jia, and R. Q. Wu. Magnetocrystalline anisotropy in permalloy revisited. *Phys. Rev. Lett.*, 97(6):067203, 2006.

[124] Z. Frait, V. Kambersky, and Ondris, M., Malek, Z. On the effective magnetization and uniaxial anisotropy of thin permalloy films. *Czeck. J. Phys.*, 13(8):330, 1963.

[125] A. Vansteenkiste, J. Leliaert, M. Dvornik, M. Helsen, F. Garcia-Sanchez, and B. van Waeyenberge. The design and verification of MuMax3. *AIP Advances*, 4(10):107133, 2014.

[126] Y. Pu, E. Johnston-Halperin, D. D. Awschalom, and J. Shi. Anisotropic thermopower and planar Nernst effect in $Ga_{1-x}Mn_xAs$ ferromagnetic semiconductors. *Phys. Rev. Lett.*, 97(3): 036601, 2006.

[127] I. V. Soldatov, N. Panarina, C. Hess, L. Schultz, and R. Schäfer. Thermoelectric effects and magnetic anisotropy of $Ga_{1-x}Mn_xAs$ thin films. *Phys. Rev. B*, 90(10):104423, 2014.

[128] G. Su, Y. Li, D. Hou, X. Jin, H. Liu, and S. Wang. Anomalous Hall effect in amorphous $Co_{40}Fe_{40}B_{20}$. *Phys. Rev. B*, 90(21), 2014.

[129] Dazhi Hou, Yufan Li, Dahai Wei, Dai Tian, Lin Wu, and Xiaofeng Jin. The anomalous Hall effect in epitaxial face-centered-cubic cobalt films. *J. Phys.: Condens. Matter*, 24(48): 482001, 2012.

[130] G. Reiss, K. Kapfberger, G. Meier, J. Vancea, and H. Hoffmann. Resistivity and the Hall effect in polycrystalline Ni-Cu and Ta-Cu multi-layered thin films. *J. Phys.: Condens. Matter*, 1:1275–1283, 1989.

[131] F. Walz. The Verwey transition - a topical review. *J. Phys.: Condens. Matter*, 14: R285–R340, 2002.

[132] Yuan Tian, Li Ye, and Xiaofeng Jin. Proper scaling of the anomalous Hall effect. *Phys. Rev. Lett.*, 103(8):087206, 2009.

[133] L. Samet, N. Masmoudi, M. W. Kharrat, and L. Kamoun. A digital PID controller for real time and multi loop control: a comparative study. *IEEE International Conference on Electronics, Circuits and Systems*, page 291, 1998.

[134] H. Unbehauen and M. Araki, editors. *Control systems, robotics, and automation - System Analysis and Control: Classical Approaches: PID Control*, volume 2. 2009.

D. Scientific contributions

Publications

1. U. Martens, T. Huebner, H. Ulrichs, **O. Reimer**, T. Kuschel, R. R. Tamming, C.-L. Chang, R. I. Tobey, A. Thomas, M. Münzenberg, J. Walowski, *Anomalous Nernst effect on the nanometer scale: Exploring three-dimensional temperature gradients in magnetic tunnel junctions*, arxiv: 1801.04186

2. R. Klett, J. Schönle, A. Becker, D. Dyck, K. Borisov, K. Rott, D. Ramermann, B. Büker, J. Haskenhoff, J. Krieft, T. Hübner, **O. Reimer**, C. Shekhar, J.-M. Schmalhorst, A. Hütten, C. Felser, W. Wernsdorfer, G. Reiss, *Proximity induced superconductivity and quantum interference in topological crystalline insulator SnTe thin film devices*, Nano Lett. accepted (2018), DOI: 10.1021/acs.nanolett.7b04870

3. T. W. Chamberlain, J. Biskupek, S. Skowron, A. V. Markevich, S. Kurasch, **O. Reimer**, K. F. Walker, G. A. Rance, X. Feng, K. Müllen, A. Turchanin, M. A. Lebedeva, A. G. Majouga, V. G. Nenajdenko, U. Kaiser, E. Besley and A. N. Khlobystov, *Stop-frame filming and discovery of reactions at the single-molecule level by transmission electron microscopy*, ACS Nano **11** (3) (2017)

4. **O. Reimer**, D. Meier, M. Bovender, L. Helmich, J.-O. Dreessen, J. Krieft, A. Shestakov, C. H. Back, J.-M. Schmalhorst, G. Reiss and T. Kuschel, *Quantitative separation of the anisotropic magnetothermopower and planar Nernst effect by the rotation of an in-plane thermal gradient*, Sci. Rep. **7** (2017)

5. A. Markewitch, S. Kurasch, O. Lehtinen, **O. Reimer**, X. Feng, K. Müllen, A. Turchanin, A. N. Khlobystov, U. Kaiser and E. Besley, *Electron beam controlled covalent attachement of small organic molecules to graphene*, Nanoscale **8** (5) (2016)

6. P. Angelova, H. Vieker, N.E. Weber, D. Matei, **O. Reimer**, I. Meier, S. Kurasch, J. Biskupek, D. Lorbach, K. Wunderlich, L. Chen, A. Terfort, M. Klapper, K. Müllen, U. Kaiser, A. Gölzhäuser and A. Turchanin, *A universal scheme to convert aromatic molecular monolayers into functional carbon nanomembranes*, ACS Nano **7** (8)(2013)

Conferences

1. Poster at the **Spin caloritronics VIII**, Regensburg, Germany (June 2017)
2. Talk and poster at the **81st Deutsche Physikalische Gesellschaft (DPG) spring meeting**, Dresden, Germany (March 2017)
3. Poster at the **Spinmechanics 4**, Lake Louise, Canada (Feb. 2017)
4. Poster at the **International Conference on Microwave Magnetics (ICMM)**, Tuscaloosa, USA (June 2016)
5. Talk at the **80th Deutsche Physikalische Gesellschaft (DPG) spring meeting**, Regensburg, Germany (March 2016)
6. Poster at the **Coloquium of the SPP 1538 (SpinCat)**, Bad Honnef, Germany (March 2016)
7. Poster at the **Spinmechanics 3**, Munich, Germany (June, 2015)
8. Talk at the **SpinCat PhD workshop**, Garching, Germany (June 2015)
9. Poster at the **79th Deutsche Physikalische Gesellschaft (DPG) spring meeting**, Berlin, Germany (March 2015)
10. Poster at the **Coloquium of the SPP 1538 (SpinCat)**, Bad Honnef, Germany (Feb. 2015)
11. Poster at the **SpinCat PhD workshop**, Bielefeld, Germany (Oct. 2014)
12. Poster at the **Spin caloritronics VI**, Irsee, Germany (July 2014)

E. Danksagung

Zum Schluss möchte ich mich bei allen Personen bedanken, die auf unterschiedlichste Art dazu beigetragen haben, dass diese Arbeit erfolgreich zustande gekommen ist. An erster Stelle danke ich meinem Doktorvater Prof. Dr. Günter Reiss, der mir in seiner Arbeitsgruppe die Möglichkeit zur Arbeit an modernsten Instrumenten sowie den Raum zum kreativen Forschen gegeben hat. Der Besuch von nationalen und internationalen Fachkonferenzen hat mich persönlich und fachlich weiterentwickelt und wird mir immer in Erinnerung bleiben. Dr. Timo Kuschel hat mich als mein direkter Betreuer und Ansprechpartner durch die Promotion begleitet und war stets für fachliche Diskussionen, Fragen und Hilfestellungen zur Stelle. Danke für das offene Ohr und die motivierenden Worte, besonders in den schweren Zeiten. Vielen Dank auch an Prof. Dr. Thomas Huser, der als Zweitgutachter meine Dissertation bewertet hat und die Erstellung des Gutachtens auch in Zeiten terminlicher Auslastung unterbringen konnte. Ebenfalls möchte ich mich bei Prof. Dr. Arun Gupta, MINT Center of University of Alabama, für einen zweimonatigen Forschungsaufenthalt im Rahmen eines Summer School Internships bedanken, welcher mir die Mitarbeit in einem amerikanischen Forschungsinstitut ermöglichte.

Eine erfolgreiche Laborarbeit steht und fällt mit dem geschmeidigen Ineinandergreifen aller benötigten wissenschaftlicher Aufbauten. Karsten Rotts unglaublicher Erfahrungsschatz hat dazu beigetragen, dass jeder einzelne Baustein funktioniert und stand mit Rat und Tat auch bei Neuentwicklungen zur Seite. Danke für diese Unterstützung! Im Hintergrund war Aggi Windmann dafür verantwortlich, dass alle bürokratischen Angelegenheiten geregelt wurden und Materialbestellungen die Laborarbeit nicht unnötig verzögert haben. Danke für diesen Beitrag.

Viele weitere Kollegen und Kolleginnen haben durch wissenschaftliche Diskussionen, konstruktive Kaffeepausen, aktive Einarbeit in das Themengebiet oder Kooperation zu diesem Schriftstück beigetragen. Dafür bedanken möchte ich mich bei: Dr. Jan-Michael Schmalhorst, Prof. Dr. Hütten, Dr. Daniel Meier, Lars Hellmich, Jan Krieft, Panagiota Bougiatioti, Orestis Manos, Alessia Niesen, Andreas Becker, Niklas Dohmeier, Dr. Martin Gottschalk, Marianne Bartke, Luca Marnitz, Jan Oliver Dreessen und Anatoly Shestakov.

Besonders hervorheben möchte ich noch meine Freunde, die mich teilweise seit dem ersten Semester des Physikstudiums begleiten und mit denen ich gemeinsam durch dick und dünn gegangen bin. Torsten Hübner (a.k.a. Dr. Torte), Robin Klett (a.k.a. RPK), Jan Haskenhoff (a.k.a. Husky), Matthias Simonis (a.k.a. Dr. Bone), Thomas Lilienkamp (a.k.a. Dr. Thomi), Michael Stührenberg und Hanno Meyer zu Theenhausen: Danke für die gemeinsame Zeit, den Frohsinn und die Urlaube. Auf viele weitere Jahre der Freundschaft!

Die letzten Zeilen widme ich den Personen in meinem Leben, die mir das Fundament für meinen Lebensweg bereitet haben, mir den nötigen Rückhalt in allen Situationen gaben und es mir dadurch ermöglicht haben, dorthin zu kommen, wo ich jetzt bin. Mit tiefster Dankbarkeit erkenne ich, was Familie bedeutet.

In ewiger Verbundenheit zu meinen Großeltern, meinen Eltern und meiner Schwester.

Danke